Development and application of perfusion MRI methods

Innovating the measurement of cerebrovascular physiology

By

Esther A. H. Warnert, MSc

A Thesis submitted to the School of Graduate Studies

in Partial Fulfilment of the Requirements for the Degree

Doctor of Philosophy

Cardiff University

“If the brain were so simple we could understand it,

we would be so simple that we couldn’t”

Emerson M. Pugh

Doctor of Philosophy (2014) Cardiff University

(Psychology) Cardiff, Wales

TITLE: Development and application of perfusion MRI methods – Innovating the measurement of cerebrovascular physiology

AUTHOR: Esther A.H. Warnert, MSc

SUPERVISORS: Prof. Richard G. Wise, Prof. Judith E. Hall

NUMBER OF PAGES: 24 (Roman),156 (Arabic)

Declaration form

The following declaration is required when submitting your PhD thesis under the University's regulations.

Declaration

This work has not previously been accepted in substance for any degree and is not concurrently submitted in candidature for any degree.

. . . .	. . . .
Candidate	Date

Statement 1

This thesis is being submitted in partial fulfilment of the requirements for the degree of PhD.

. . . .	. . . .
Candidate	Date

Statement 2

This thesis is the result of my own independent work/investigation, except where otherwise stated. Other sources are acknowledged by explicit references.

. . . .	. . . .
Candidate	Date

Statement 3

I hereby give consent for my thesis, if accepted, to be available for photocopying and for inter-library loan, and for the title and summary to be made available to outside organisations.

. . . .

Candidate Date

Statement 4: Previously approved bar on access

I hereby give consent for my thesis, if accepted, to be available for photocopying and for inter-library loans after expiry of a bar on access previously approved by the Graduate Development Committee.

. . . .

Candidate Date

Acknowledgements

I would like to take this opportunity to thank everyone who has supported me throughout my PhD. Firstly I would like thank Professor Richard Wise, for being the best supervisor a PhD student can have. I am very grateful for all the time, help, and guidance you have given me. Your support has been invaluable throughout my PhD and I cannot imagine where I would be without it. Thanks also go to my supervisor Professor Judith Hall, for being an inspiration and for giving valuable input whenever needed. Special thanks go to Dr. Kevin Murphy for all the time and help you have given me, even if I was not yours to supervise, and to Dr. Ashley Harris for your help and patience when I turned up at your desk yet again with one of my ‘first year’s’ questions. Thanks also go to everyone in CUBRIC, in particular the past and present occupants of the analysis room, who made CUBRIC the best place to work.

I would also like to thank the people who I have collaborated with throughout my PhD. Firstly, I would like to thank Dr. Emma Hart not only for all your time and help, especially in my final year, but also for the fun times we had during our meetings and experiments. Secondly, I would like to thank Andrew Lansdown for the pleasant collaboration during many hours of scanning (and learning a thing or two about sharks!).

Finally, I would like to thank my friends and family for all their support throughout the years, from surprise international birthday visits to promising to only prank my room after I submit my thesis. I hope you accept my humble apologies for my writing-up-thesis induced anti-social behaviour. And mum, especially for you: eind goed, al goed!

Summary

A healthy cerebrovasculature is important in maintaining constant delivery of blood carrying oxygen and nutrients required for normal cerebral function. There is a considerable body of research into the regulation of the cerebrovasculature and cerebral blood flow, which has improved diagnosis, treatment and prevention of cerebrovascular pathology. However, a severe confound in research concerning the cerebrovasculature is the limited amount of in vivo human data available that assesses function and physiology of key cerebral structures: the brainstem and the cerebral arteries themselves. The work presented in this thesis aims to provide non-invasive imaging tools that can be used to further the understanding of cerebrovascular function and physiology. Herein, innovations of arterial spin labelling, an established magnetic resonance imaging technique to measure perfusion, are presented that address the challenges of measuring brainstem cerebrovascular physiology and facilitate a novel measurement of cerebral arterial compliance, a marker of cerebrovascular health.

Regulation of the cerebrovasculature by the sympathetic nervous system is used throughout this thesis as an example process that can be investigated with arterial spin labelling based imaging methods, because the brainstem is an important sympathetic control centre and changes in sympathetic outflow directly affect the cerebral arteries. Firstly, arterial spin labelling is adapted to measure cerebral blood flow in the brainstem. The arterial spin labelling method tailored for the brainstem is then applied in the investigation of cerebral blood flow in the presence of poly-cystic ovary syndrome, a pathology recently associated with elevated sympathetic outflow. Secondly, an arterial spin labelling based approach to measure cerebral arterial compliance is introduced. Lastly, this thesis shows that a combination of the optimised brainstem perfusion imaging method and the novel arterial compliance measurement is able to investigate clinically relevant processes, including cerebral autoregulation and Cushing’s mechanism.

List of abbreviations

aBV	Arterial blood volume
AC	Arterial compliance
ACA	Anterior cerebral artery
ACC	Anterior cingulate cortex
AFNI	Analysis of functional neuroimages
ANS	Autonomic nervous system
ASL	Arterial spin labelling
BA	Basilar artery
BMI	Body-mass index
BOLD	Blood oxygen-level dependent
BP	Blood pressure
BS	Brainstem
bSSFP	Balanced steady state free precession
CASL	Continuous arterial spin labelling
CBF	Cerebral blood flow
CSF	Cerebral Spinal Fluid
CNS	Central nervous system
CVLM	Caudal ventrolateral medulla
CVR	Cerebral vascular reactivity
DLF	Dorsal longitudinal fasciculus
EPI	Echo planar imaging
EPISTAR	Echo-planar imaging and signal targeting with alternating radio frequency
FAIR	Flow-sensitive alternating inversion recovery
FID	Free induction decay
FSL	FMRIB’s software library
FSPGR	Fast spoiled gradient echo
GM	Grey matter
HC	Hypercapnia
ICA	Internal carotid artery
IFC	Isometric forearm contraction
MAP	Mean arterial pressure

MB	Midbrain
MCA	Middle cerebral artery (RMCA & LMCA indicate right or left MCA)
MD	Medulla
ME-ANOVA	Mixed-effect analysis of variance
MNI	Montreal neurological institute
MRI	Magnetic resonance imaging
MSNA	Muscle sympathetic nerve activity
MT	Magnetisation transfer
MTI PASL	Multi inversion time pulsed arterial spin labelling
NC	normocapnia
NTS	Nucleus of the solitarty tract
P	Pons
PASL	Pulsed arterial spin labelling
PCA	Posterior cerebral artery (RPCA & LPCA indicate right or left PCA)
pCASL	Pseudo continuous arterial spin labelling
PCC	Posterior cingulate cortex
PCOS	Poly-cystic ovary syndrome
PEI	Post exercise ischemia
PET	Positron emission tomography
PICORE	Proximal inversion with a control for off-resonance effects
PNS	Peripheral nervous system
QUIPSS II	Quantitative imaging of perfusion using a single subtraction, version II
RF	radiofrequency
RM-ANOVA	Repeated measures analysis of variance
ROI	Region of interest
RVLM	Rostral ventrolateral medulla
SAR	Specific absorption rate
SMC	Smooth muscle cell
SNA	Sympathetic nerve activity
SNS	Sympathetic nervous system
SVD	Small vessel disease
TE	Echo time
TI	Inversion time
TR	Repetition time

VA	Vertebral artery
VASO	Vascular space occupancy

Contents

Chapter 1

Chapter 2

Chapter 3

Chapter 4

Chapter 5

Chapter 6

Chapter 7

Chapter 8

Appendix A

Chapter 1

Introduction

Maintaining constant delivery of blood carrying oxygen and nutrients is of utmost importance for healthy brain function. An intricate system that balances supply and demand of arterial blood within the brain underlies healthy cerebrovascular physiology. A problem in the supply of arterial blood can have severe short- and long-term consequences. Acute cerebral ischemia can cause fatal stroke, while chronic stiffening of the cerebral vasculature can lead to small vessel disease. There is a considerable body of research into the regulation of the cerebrovasculature and cerebral blood flow (CBF) because this knowledge aids in diagnosis, treatment and prevention of cerebrovascular pathology. However, a severe confound in research concerning the cerebrovasculature is the limited amount of *in vivo* human data available that assesses function and physiology of key cerebral structures: the brainstem and the cerebral arteries themselves. The work presented in this thesis aims to provide non-invasive imaging tools that can be used to further the understanding of cerebrovascular function and physiology.

In this thesis we investigate questions around the sympathetic regulation of the cerebrovasculature as an example system for application of our imaging tools, while it is acknowledged that it is an interplay between many factors that regulate CBF. For instance, the vasculature can be affected locally by specific actions, e.g. increases in CBF of the motor cortex can be induced by a simple finger tapping task, while there are systemic factors that can influence whole brain vasculature, e.g. an increase in intra-arterial carbon dioxide is a strong vasodilatory stimulus that leads to whole brain increases in CBF. However, controversy still exists over the contribution of the sympathetic nervous system to regulation of CBF and an important cause for this controversy is the lack of human in vivo data on sympathetic regulation of the cerebrovasculature. Therefore, the branch of research investigating sympathetic regulation of the cerebrovasculature is one that may benefit from having non-invasive measurements of cerebrovascular function and physiology. Note that throughout this thesis CBF is used to define the amount of blood delivered to the brain parenchyma in ml/100 g/min (ml of arterial blood delivered to 100 g brain tissue per minute).

Arterial spin labelling (ASL) is a magnetic resonance imaging method that facilitates non-invasive measurement of cerebral blood flow. Therefore ASL is used throughout this thesis to assess cerebrovascular physiology. Chapter 2 contains an overview of the principles of magnetic resonance imaging and arterial spin labelling methods.

The sympathetic nervous system plays a key role in regulating the supply of arterial blood because of the sympathetic nerve fibres innervating the cerebral macrovasculature. Stimulation of these fibres is regulated by nuclei located in the brainstem. Chapter 3 contains an overview of the anatomy of the cerebrovasculature, brainstem and the sympathetic regulation of cerebrovascular tone.

Chapter 4 contains the process of optimising multi inversion time pulsed arterial spin labelling imaging to measure the cerebrovascular physiology in the brainstem, an area that is difficult to image with perfusion weighted imaging. The experiment described in Chapter 4 addresses the challenges of ASL imaging of the brainstem. In addition, the feasibility of the brainstem optimised ASL protocol is tested by measuring increased CBF in the brainstem. Elevated perfusion is induced by hypercapnia, an established stimulus that increases CBF because of the potent vasodilatory effect of carbon dioxide.

The ASL protocol introduced in Chapter 4 is applied to a clinical cohort in Chapter 5, in which an exploratory perfusion imaging study is performed on patients with poly-cystic ovary syndrome (PCOS) and healthy controls. PCOS has recently been linked to hyperactivity of the sympathetic nervous system, and it is because of this that we hypothesised that differences in cerebrovascular physiology of the brainstem exist between PCOS patients and healthy controls. In addition, the relatively large number of participants (i.e. 38) allowed us to investigate the relationship between mean arterial blood pressure and cerebral blood flow, which gives an indication of the areas within the brain that are either involved in regulation of or are affected by variations in systemic blood pressure.

In addition to the brainstem optimised ASL method, this thesis presents innovations in arterial spin labelling methods that facilitate measurement of cerebral arterial compliance. Chapter 6 introduces the ASL imaging protocol that enables direct measurement of this marker of vascular health of individual cerebral arteries. The novel technique for measuring cerebral arterial compliance (AC) was based on the brainstem optimised perfusion protocol. In the latter, a two-compartment model was used that included fitting of a macrovascular compartment, which was discarded in the perfusion analysis. However, exploring the macrovascular compartment showed that there was valuable information in the macrovascular signal and in Chapter 6 it is shown how this can be used to assess arterial compliance of individual cerebral arteries.

Chapter 7 contains the application of both the brainstem optimised ASL and arterial compliance measurement to assess the role of the sympathetic nervous system in regulation of cerebrovascular physiology. In a group of healthy volunteers sympathetic outflow is elevated by isometric forearm contraction followed by post exercise ischemia and both methods introduced in chapters 4 and 6 are applied to investigate how elevated sympathetic nervous activity changes cerebrovascular physiology.

The final chapter contains an overview of the main findings of this thesis. In addition, an eye is cast on the future; further developments regarding the herein presented methods are highlighted, as well as avenues of research in which the brainstem optimised ASL and arterial compliance measurements can be of use.

Chapter 2

Magnetic resonance imaging of cerebrovascular physiology

MRI is an established non-invasive technique that is already used to investigate cerebrovascular function and anatomy. In this thesis pulsed arterial spin labelling is further developed to assess cerebrovascular physiology. This chapter first contains an overview of the principles of MRI, after which an overview is given of the techniques of interest in this thesis.

2.1 Principles of MRI

Spin

Nuclear magnetic resonance imaging (MRI) is a technique that uses inherent properties of nuclei in atoms to create images from objects or organisms placed in a magnetic field. Not all existing nuclei are suitable for MRI, because not all have a net *spin*. In order to explain *spin* it is important to realize that atom nuclei contain 2 different types of particles: neutrons and positively charged protons. Each of the particles in the nucleus has an *angular momentum* or *spin*, a quantum mechanical property which is analogous to the angular momentum of a spinning top[1]. However, instead of having a continuous range of possible values, the angular momentum of an individual particle can only be +1/2 or -1/2. Whether a nucleus is suitable for MRI depends on whether it has a net angular momentum of the nucleus; any nucleus with an even mass number and an even charge number has no net momentum. Examples of atoms with momentum are phosphor-31, oxygen-17, and nitrogen-15. However, with its natural abundance of 99.9% hydrogen-1 (^{1}H), with a net *spin number* of 1/2, is commonly used for MRI experiments[1]. Note that the spin number of hydrogen means that there are two energy states in which the nucleus can be in a polarising magnetic field: a low (-1/2) and high (+1/2) energy state.

In the absence of a strong magnetic field, hydrogen nuclear spins of organic tissue are randomly orientated. When a strong magnetic field is applied to the tissue, a small portion of spins align with this field resulting in a net magnetisation vector within the tissue. The main magnetic field is also called $\boldsymbol{B_0}$. At the physiological temperature of 37 °C and a B_0 of 1.5 Tesla only 0.00001 % of the spins aligned parallel with the magnetic field are not cancelled out by anti-parallel spins, resulting in net magnetisation along B_0[1]. The hydrogen spins precess with the so-called Larmor frequency (ν), which is calculated by multiplying the gyromagnetic ratio of the atom (42.6 MHz/T for hydrogen) with the strength of B_0 in Tesla (T). For hydrogen at 3 Tesla the Larmor frequency is 128 MHz[1].

An additional magnetic field (B_1) can be applied that oscillates with the Larmor frequency, which causes the hydrogen spins to rotate with this additional field and can temporarily change their orientation. The result of this is that the net magnetisation is ‘tipped’ away from the B_0 direction towards the transverse plane perpendicular to the direction of the static magnetisation. This transverse magnetisation can be detected because it results in a changing voltage through a receiver coil. The angle of this perturbation of the net magnetisation depends on the strength and duration of the B_1 field and is called *flip angle*. When B_1 is switched off all hydrogen spins will align to B_0 again and the net magnetic vector is restored; a process called *relaxation* (illustrated in Figure 2.1). Important conventions are that the direction of B_0 is also called the z-direction, and that the transverse plane is determined by the x- and y-direction. Also note that the net magnetisation vector precesses around the z-axis, and that it is therefore convenient to consider a rotating frame of reference in which the transverse plane rotates around the z-axis (denoted by the x’- and y’-directions).

Relaxation

As is illustrated by Figure 2.1, during relaxation two processes occur: the recovery of the longitudinal magnetisation (M_Z) and the decay of the transverse magnetisation (M_T). The recovery of M_Z occurs because of thermal energy transfer within the tissue between the perturbed hydrogen atoms and the magnetic field of the surrounding *lattice*, which is the structure in which nuclei are held. Thermal energy transfer occurs such that after hydrogen atoms are perturbed by an additional magnetic field, energy dissipates into the lattice into the equilibrium state related to the B_0 field strength. The rate of recovery of M_Z therefore depends on the type of tissue, i.e. the type of lattice, and B_0 field strength. The time constant of this *spin-lattice* relaxation process is called T_1 and denotes the time it takes to reduce the difference between the current value of M_Z and the equilibrium magnetisation by a factor of *e*.[1,2] The relaxation curves of the longitudinal and transverse magnetisations are derived from the *Bloch equations*. The T_1 relaxation curve describing the recovery of M_Z to the equilibrium magnetisation is:

$$M_z(t) = M_0 + (M_z(0) - M_0)e^{-t/T_1} \qquad \text{Eq. 2.1}$$

where M_0 is the equilibrium magnetisation and $M_Z(0)$ depends on the applied flip angle, e.g. $M_Z(0) = 0$ in the case of a 90° pulse.

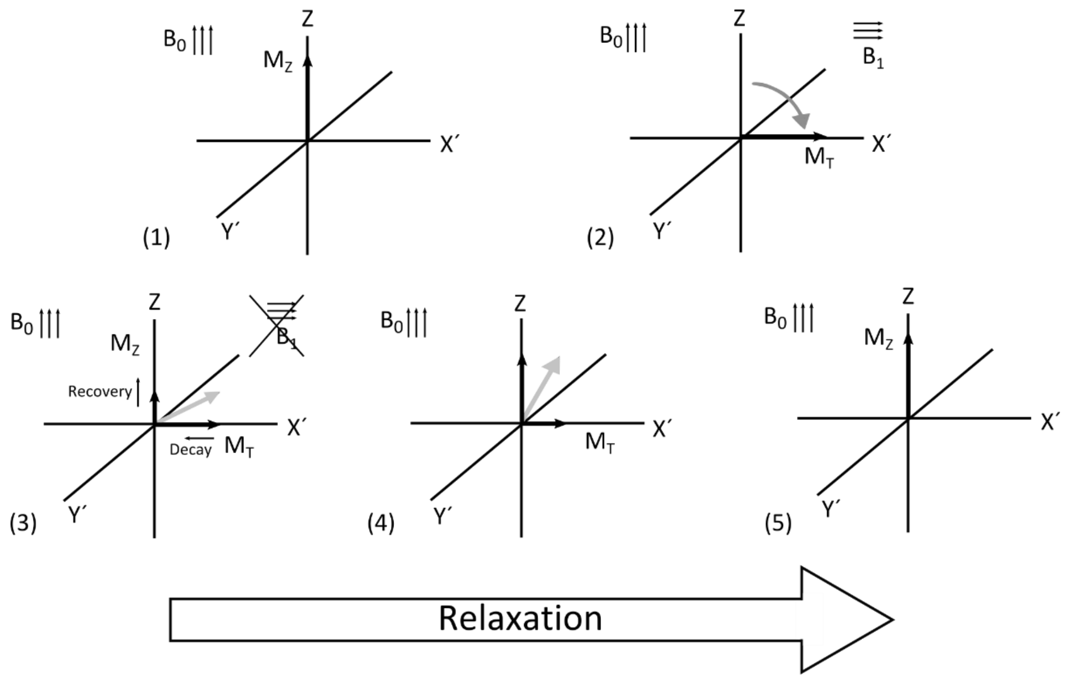

Figure 2.1. (1) Schematic of the net equilibrium magnetisation vector (M_Z) which is a summation of all hydrogen atoms in tissue, when a main (static) magnetic field is present (B_0). (2) Net magnetisation can be ‘tipped’ into the transverse plane when an additional magnetic field (B_1) is applied that oscillates with the Larmor frequency of hydrogen. The net magnetisation that results in the transverse plane is called M_T. Note that here an example is given from a 90° pulse, but that the angle with which this perturbation is performed depends on the strength and duration of B_1. Relaxation is the process in which the net magnetisation vector (grey vector in 3-5) is restored in the z-direction when B_1 is switched off. In this process M_Z gradually recovers, while M_T decays away. Note that the x’- and y’-axes represent a rotating frame of reference.

Secondly, there is the decay of the transverse magnetisation M_T, which occurs because of dephasing of the hydrogen spins, after the perturbation of M_Z by B_1 brought all the hydrogen spins in phase. Dephasing is a result of irregularities in the magnetic field, i.e. spins deviating from the Larmor frequency, on two different scales. On the molecular level all hydrogen nuclei in different molecules have their own random movements causing them to precess with frequencies that slightly deviate from the Larmor frequency, which means that overtime dephasing of the spins occurs as soon as B_1 is switched off. This process of relaxation is called spin-spin or T_2 relaxation and the time constant T_2 denotes the time it takes for M_T to decay away[2]. On a larger scale the presence of inhomogeneities in the B_0 field causes dephasing in a similar manner as T_2 relaxation. Field inhomogeneities arise in particular near boundaries of tissues with different magnetic susceptibilities. Examples of this are the air/tissue boundaries near the sinuses in the human head or between blood vessels and tissue, because of the strong magnetic effects of deoxyhaemoglobin[1]. These field inhomogeneities cause rapid dephasing of the hydrogen spins, which occurs with time constant T_2'.[2] The time constant with which the transverse M_{XY} decays away (T_2^*) is then determined as follows:

$$\frac{1}{T_2^*} = \frac{1}{T_2} + \frac{1}{T_2'} \qquad \text{Eq. 2.2}$$

An important difference between the dephasing of hydrogen spins caused by molecular interactions and the dephasing caused by field inhomogeneities is that the latter is reversible with a 180° pulse, while the former is not. A schematic of measured signal in the transverse plane can be seen in Figure 2.2. After a single B_1 pulse a free induction decay (FID) curve is detected that oscillates and decays exponentially with a relaxation rate determined by T_2^*. If 180° pulses are included in the experiment it can be seen that the signal lost from dephasing spins due to field inhomogeneities is recovered, but that due to T_2 relaxation over time the transverse signal decays nonetheless. The T_2 relaxation curve describes the decay of the transverse magnetisation due to T_2 relaxation:

$$M_T(t) = M_T(0)e^{-t/T_2} \qquad \text{Eq. 2.3}$$

where $M_T(0)$ is the transverse magnetisation directly after the application of B_1. Note that the time course of T_2^* relaxation is obtained by substituting $1/T_2$ with $1/T_2^*$ from Eq. 2.2.

Spatial specificity

When imaging of organic tissue, for instance a human head, is of interest it means that a two- or three-dimensional map needs to be created showing the spatially varying density of hydrogen spins. Note that the above paragraphs describe how signal is generated by bringing hydrogen spins in a state in which they precess with the Larmor frequency of a strong magnetic field, followed by perturbing the spins with an additional field in a different direction, but oscillating with the same frequency, such that they resonate with the additional field. In order to create spatial specificity in an object it is necessary to have a spatially varying Larmor frequency, which can be induced by creating a spatially varying static magnetic field. For this purpose, and in addition to a large coil generating the static B_0 field, an MRI scanner has gradient coils which manipulate the B_0 field such that it varies spatially[1].

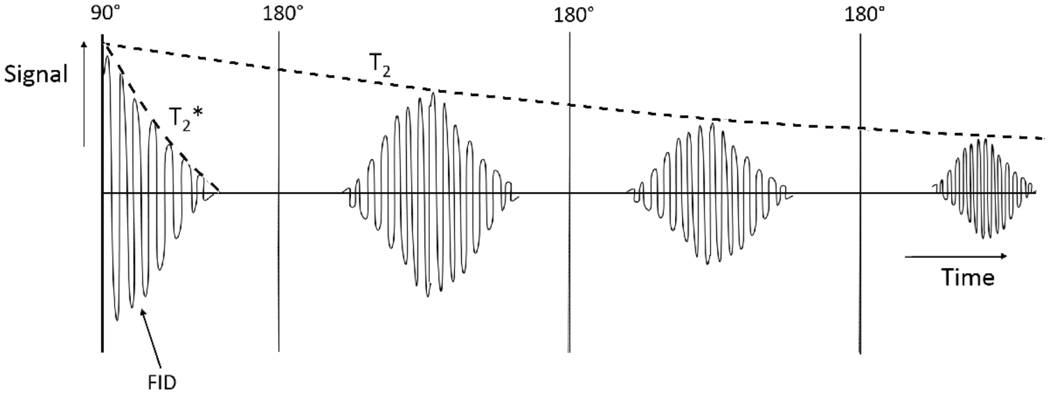

Figure 2.2. Schematic of transverse signal in a pulse sequence. Note that after a 90° pulse there is a free induction decay (FID) signal that decays away within T_2* because of local inhomogeneities in the magnetic field. These can be recovered by application of a 180° pulse. However, note that despite 180° pulses the signal decays because of dephasing of hydrogen spins based on molecular interactions. An acquisition scheme that uses 180° pulses to create read-out echoes is also called a spin echo acquisition.

Slice selection of an object within an MRI scanner occurs in the presence of a linear gradient in B_0, generated by a gradient coil. As a result the hydrogen spins in the sample have a Larmor frequency depending on their location. Slice selection is accomplished by a B_1 magnetic field that is oscillating with the frequency equal to the hydrogen spins in the slice of interest. Note that spins precessing with a different frequency from B_1 are not affected, because no energy transfer between the B_1 field and these spins occurs. In order to make the signal within the slice spatially selective, i.e. to create a 2D image, there are two additional coils that create orthogonal gradients within the slice; the x- and y-directions (if z has been chosen as the slice selective direction)[1]. It is common for the x-direction in two-dimensional acquisitions to be denoted as the *frequency encoding* direction, in which spatially varying frequencies are created in a similar manner as for the slice selection process, but in a direction orthogonal to the slice selective direction (illustrated by Figure 2.3). The y-direction is orthogonal to both the slice selection and frequency encoding direction and is also called the *phase encoding* direction. In the presence of phase encoding gradients spins accumulate phase depending on their spatial location along the phase encoding gradient direction (illustrated by Figure 2.4).

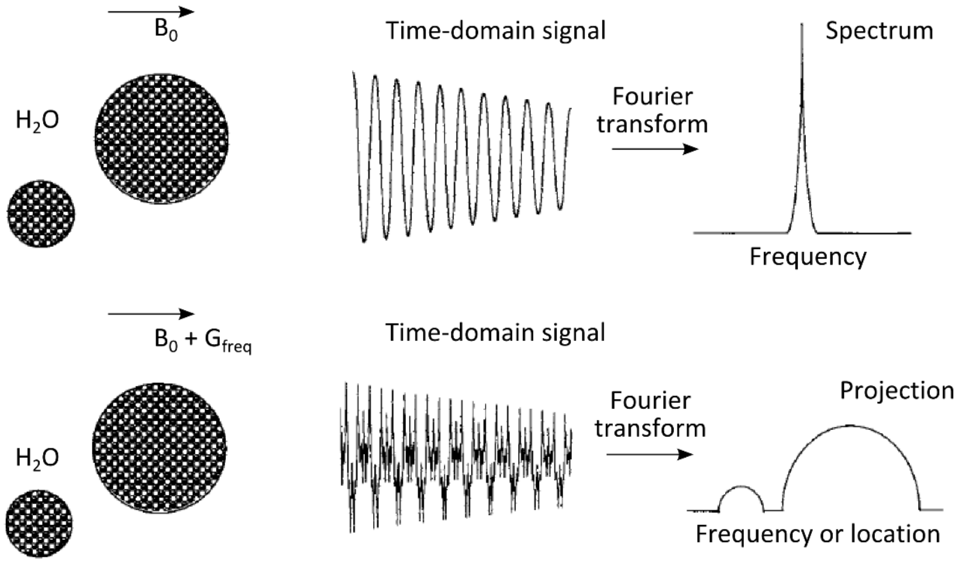

Figure 2.3. Schematic of frequency encoding by a frequency encoding gradient (G_{freq}). The top row shows that the time-domain signal of two plates of water in a B_0 field, in the absence of a frequency encoding gradient, contains a single frequency (the Larmor frequency of water). The origin of the spins (small or large plate) cannot be determined in the top row. The bottom row shows the same plates of water in presence of G_{freq}, in which spins have a spatially varying precessing frequency. The Fourier transform of the time domain signal is a projection of the plates of water; the amplitude at each frequency in the spectrum is proportional to the amount of spins with that frequency. *Image adapted from "Handbook of MRI pulse sequences" (Figure 8.1)*[3].

The signal that is measured during the read-out period is the transverse magnetisation originating from all the spins within the selected slice, which results in an envelope of signal with frequencies resulting from the modulation caused by the frequency and phase encoding gradients and the amplitude of these signals is dependent on the spin density within the image. In other words, a frequency spectrum is acquired that is dependent on the spatial variation in spin densities within the object. In order to obtain a map of the spin densities, i.e. the NMR image, the acquired signal in the spatial frequency domain is transferred into the spatial domain with a Fourier transform. The spatial frequency domain in which the signal is acquired is also called k-space[1,4].

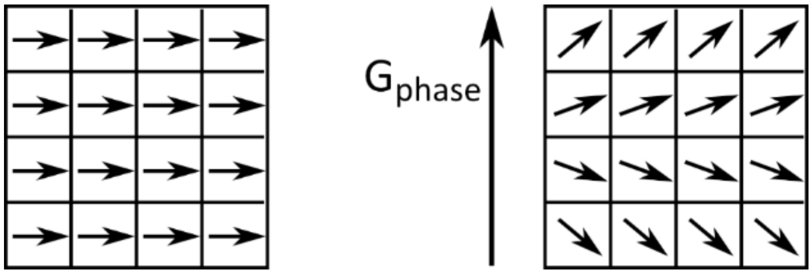

Figure 2.4. Schematic of effect of phase encoding gradient (G_{phase}). An image is divided into 16 pixels, the arrows indicate the transverse magnetisation directly after a 90° radiofrequency pulse. On the left, it can be seen that in the absence of G_{phase} all spins have the same phase, directly after the 90° pulse. However, after the application of G_{phase} the phase of the transverse magnetisation varies along the phase encoding direction. *Image adapted from "Handbook of MRI pulse sequences" (Figure 8.8)*[3]

Data acquisition in k-space

There are several manners in which k-space data can be sampled, but for the purpose of this thesis it is important to know two common trajectories: Cartesian and spiral trajectories[4]. The most common read-outs in MRI are Cartesian, in which k-space data are acquired line-by-line. The example in Figure 2.5A shows an echo planar imaging (EPI) read-out in which all lines of k-space are acquired after a single excitation pulse. EPI is a fast acquisition scheme, but typically has a relatively low resolution[4]. It is also possible to acquire a single line of k-space data after an excitation pulse, which is slower than EPI but is commonly used to give higher resolution images[4]. Figure 2.5B illustrates a spiral trajectory, in which k-space data is acquired by spiralling out from the centre of k-space (spiral-out trajectory). Advantages of the spiral-out trajectory are that it is a fast acquisition trajectory, as it does not require gradient loading at the start of acquisition, and that it covers k-space in a more efficient manner than a Cartesian read-out, skipping the corners in which there is low signal[5]. Another advantage from spiral versus Cartesian read-outs comes from the limited speed in which the gradient coils can be loaded, which means that in a spiral acquisition the origin of k-space is rapidly oversampled. This last feature makes spiral imaging robust against motion induced by flow or cardiac pulsations, as these processes affect in particular the signal acquired near the origin of k-space because the lower k-space frequencies have higher spectral energy than high k-space frequencies[6]. In the k-space periphery spectral energy is already low, meaning that phase changes induced by cardiac pulsations are of less importance.

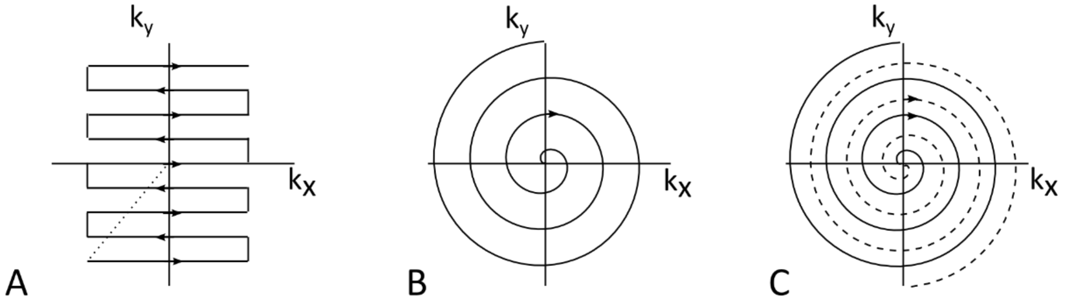

Figure 2.5. Examples of read-out trajectories of k-space. (A). An example of Cartesian read-out in which k-space is read line-by-line. The example shows the read-out in echo planar imaging. Note that the dashed line indicates loading of the gradients before read-out can start. (B). Example of spiral trajectory. Note that this example shows a spiral-out trajectory, but that it is also possible to start at the periphery of k-space and apply a spiral-in read-out. (C). Interleaved read-out with two spiral interleaves. Note that a similar multi-shot trajectory can also be used with a Cartesian read-out.

Differences between Cartesian and spiral read-outs are prominent in the generation of image artefacts. The two different encoding directions in Cartesian read-outs result in different artefacts in relation to the gradient direction. For instance, off-resonance spins (i.e. spins precessing with a different frequency than the encoded Larmor frequency) in a Cartesian read-out result in displacement of the signal along the frequency encoding direction[3]. While unwanted phase shifts along the phase encoding direction result in wrap-around artefacts: signal from one side of the image (e.g. the top) is acquired as if it originates from the opposite site (e.g. the bottom) due to phase shifts of the hydrogen spins[3]. A spiral trajectory has the same spacing in the k_y- and k_x-directions and off-resonance spins cause displacement of signal in all directions, i.e. spiral blurring[5]. However, the amount of blurring decreases with shorter read-out durations: the shorter the duration of the spiral trajectory, the less phase is accumulated to cause off-resonance effects[5].

Another aspect of k-space data sampling is that acquisition can be done with a single shot (as Figure 2.5AB) or with multiple shots (Figure 2.5C). Note that the example in Figure 2.5C is given for the spiral acquisition, but that the EPI acquisition can also be acquired in multiple shots. The advantage of using a multi-shot acquisition is that the acquisition window, i.e. the duration of a single trajectory, can be shorter to cover the same range in k-space. The shorter acquisition window means that there is a higher signal to noise ratio for the signal acquired at the periphery of k-space, where high spatial frequencies are encoded, because less signal has decayed away. Moreover, multi-shot spiral trajectories oversample the k-space origin even more than single shot spiral acquisitions, reducing motion artefacts resulting from flow and cardiac motion even further[7]. However, with going from a single shot to a multi-shot acquisition a trade-off needs to be made, because bulk motion between the shots (i.e. head motion of the subject) is detrimental for image reconstruction. In addition, total image acquisition becomes longer, because each shot is acquired in one repetition time.

Generating contrast

Magnetic resonance images are maps in which signal is related to proton densities. However, the density of hydrogen is similar in different organic tissues, e.g. muscle (79.2%) and grey matter (77.4%)[8], which results in little contrast if relying on proton density alone[1]. Fortunately, the relaxation times of perturbed hydrogen spins varies widely between organic tissues and contrast can be generated by exploiting the differences in these T_1, T_2 and T_2* relaxation times.

A high resolution structural scan of the brain in which there is a clear contrast between grey and white matter, is commonly made with T_1-weighting. In such an image, grey matter has a lower intensity than white matter because the T_1 of grey matter is longer than white matter (1200 ms and 860 ms at 3T, respectively[1]) and imaging takes place before M_z for both tissues has recovered (illustrated by Figure 2.6). One example of a fast image acquisition scheme with T_1-weighting is a Fast Spoiled Gradient Echo (FSPGR) sequence in which a low flip angle and short TR (TR < 10 ms) are used. The speed of this acquisition scheme results in steady state M_z values because there is not sufficient time between excitation pulses for the signal to recover. In an FSPGR sequence the steady state M_z values are dependent on the T_1 relaxation times of the tissues[9]. Note that in a FSPGR sequence the echo time (TE), which is the time between an excitation pulse and the time of image acquisition, is as short as possible (TE << TR).

Another example, often used in functional imaging, is generating a T_2* weighted contrast, such that there is little effect of differences in longitudinal magnetisation (for instance using long TR, i.e. TR >> T_1). Echo times (TE) are set in such a way that contrast arises from

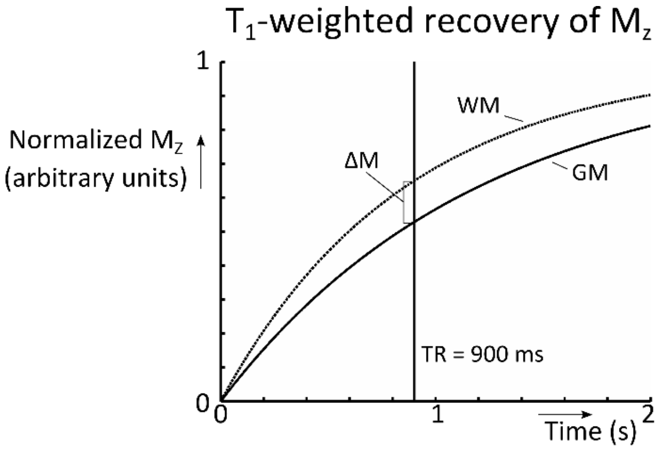

Figure 2.6. Schematic of T_1-weighted recovery of the longitudinal magnetisations of grey matter (GM) and white matter (WM) after an excitation pulse with a 90° flip angle. Note that if a repetition time (TR) is chosen between the T_1 from both tissues, i.e. 900 ms, signal difference (ΔM) between GM and WM is large despite having similar proton densities. *Image created based on "Principles of nuclear magnetic resonance and MRI" by Jezzard and Stuart*[1].

differences in T_2* relaxation within tissues[1]. The fact that T_2* relaxation times are in part dependent on dephasing caused by local inhomogeneities in the magnetic field is a property exploited in functional blood oxygenation-level dependent (BOLD) imaging.

Signal in BOLD imaging depends on the oxygen level in the blood, because of the difference in magnetic properties between oxyhaemoglobin and deoxyhaemoglobin. The latter is a paramagnetic molecule, which means that it causes inhomogeneities in the local magnetic field, while oxyhaemoglobin is diamagnetic (does not change the local magnetic field)[10]. It is therefore possible to use MRI to measure changes in oxygenation levels in the blood; when local metabolism increases there is a decrease in local deoxyhaemoglobin, because of the increased oxygen supply through greatly increased blood flow. The decrease in local deoxyhaemoglobin leads to a more homogeneous magnetic field and therefore an increase in T_2*. In BOLD imaging the TE is set similar to the T_2* of blood (30 ms at 3 T), such that changes in local oxygenation can be detected[1]. BOLD imaging is often referred to as functional imaging, because local changes in oxygenation are, amongst other things, dependent on local activity levels. BOLD imaging is therefore commonly used to assess tissue function.

2.2 Arterial spin labelling

Contrast can also be generated by sensitizing the intensity within an image to the amount of blood delivered to the tissue within the volume of interest, which is referred to as *perfusion imaging.* The following section contains an overview of perfusion imaging with a technique called arterial spin labelling (ASL), because this is the method used throughout this thesis to assess cerebrovascular physiology. In ASL hydrogen in arterial blood is labelled to map tissue perfusion. At least two images are made; a control image, in which no labelled blood is present, and a tag image containing blood that is tagged before it flows into the imaging plane or volume. The difference between the tag and control images is proportional to tissue perfusion, which is also called cerebral blood flow (CBF) when imaging the brain. For quantification of CBF models are fit to the difference in signal intensities that calculate perfusion as the amount of blood delivered per 100 g brain tissue per minute (ml/100 gr/min)[11,12].

Magnetic labelling occurs by inverting[13] or saturating[14] the longitudinal magnetisation of blood before it flows into the imaging volume. This means that at image acquisition, the labelled spins that have flowed into the imaging volume have less longitudinal magnetisation than the stationary spins within the image. Subtracting this labelled image from a control image, acquired without labelling, results in a difference image in which the signal intensities are proportional to the amount of delivered blood.

There are two main types of ASL labelling scheme: pulsed (PASL)[13,15,16] and (pseudo) continuous ASL (pCASL)[11,17]. In pulsed ASL (PASL) the label takes place by a brief pulse covering a large slab of tissue (i.e. 10-20 cm). Pseudo continuous ASL evolved from continuous ASL (CASL), in which spins are tagged as they flow through a thin tagging plane created by a relatively long radiofrequency (RF) pulse, e.g. 1-2 seconds in duration[17]. However, the impracticality of a long and continuous RF pulse, such as high specific absorption rates (SAR) and the high demand on system hardware, led to the development of pCASL in which the single RF pulse is substituted for a train of short RF pulses[18,19].

Throughout this thesis PASL is the perfusion imaging method of choice, despite the theoretical advantage of pCASL. The latter has the potential to give a better signal-to-noise ratio (SNR) than PASL because of the longer temporal duration of the label, simply resulting in more signal being generated[20]. However, one drawback of pCASL is the substantial amount of magnetization transfer (MT) resulting from a train of short RF pulses. This effect will decrease signal in the image: a continuous off-resonance pulse (the label, which is off-resonance for the imaging volume) will saturate the magnetization of free water protons in the image because of magnetisation transferred from protons bound to macromolecules, which are excited by the off-resonance pulse[21]. This means that signal decrease in the label image comes from the labelled blood or from the MT effect and, without correcting for the latter, perfusion is overestimated. To correct for MT in the image it is possible to do local tagging with a separate RF coil[11] or to acquire the control image with the same amount of MT[11]. Both methods however have drawbacks, the first requires additional hardware, while for the second method it is important that there is symmetry between the labelling pulse and the control pulse to give the same amount of MT without labelling the blood[11].

In addition, an advantage of PASL over pCASL methods is that the instantaneous labelling pulse in PASL is less sensitive to the blood flow velocity within the labelling slab, making inversion of blood more efficient[20,22]. In pCASL, efficiency of the inversion decreases when the blood flow velocity through the labelling plane becomes faster[22]. The decrease of labelling efficiency in pCASL is of particular importance when perfusion imaging is used in an experiment in which blood flow velocities are expected to change; flow velocity increases with a functional task or with an increase in partial pressure of carbon dioxide (hypercapnia)[22].

PASL pulse sequences

There are three different pulsed ASL sequences that are widely used in CBF research; Flow-sensitive Alternating Inversion Recovery (FAIR)[16,23], Echo-Planar Imaging and Signal Targeting with Alternating Radio frequency (EPISTAR)[15], and Proximal Inversion with a Control for Off-Resonance Effects (PICORE)[24]. These methods differ in the manner of creating the labelled image, in which inflowing blood is inverted with a 180° pulse, and a control image in which the static protons sense the same magnetisation as in the labelled image, but arterial blood is not inverted. In FAIR, the label image is created after a global non-selective inversion of all spins and the control image is acquired after a selective pulse on the imaging slice[25]. Note that this means that at time of imaging the control image has arterial blood with fully relaxed hydrogen spins, while in the label image the blood contains inverted spins. EPISTAR is one of the earliest methods for PASL in which a thick inversion band proximal to the imaging volume is applied before the label image is acquired, while the control image is acquired after application of the same inversion band distal to the imaging volume[15]. The inversion bands are created by off-resonance RF pulses in the presence of a gradient field that enables selection of the correct inversion band. PICORE imaging uses the same proximal inversion approach as EPISTAR to create the label image, but the control image is acquired after the same RF pulse is applied without a slice-selective gradient switched on[24]. This means that, in comparison to FAIR and EPISTAR, no blood is labelled superior to the imaging volume of the control acquisition with the PICORE technique, as illustrated by Figure 2.7. PICORE is therefore used throughout this thesis.

One issue with the original PICORE technique is that the instantaneous inversion band results in a spatially defined labelled bolus. The downside of this spatially defined bolus is that when there is a global increase in cerebral blood flow, as happens in hypercapnia for instance, measurement of this increase in perfusion might be underestimated because of the increased flow velocity in the inversion band. This underestimation is a result of the same amount of hydrogen spins being labelled compared to a baseline CBF measurement, despite the higher flow velocity through the inversion band. In order to circumvent this issue and make the PASL bolus time dependent, i.e. when blood flows faster more spins are labelled, Wong et al.[13] introduced Quantitative Imaging of Perfusion Using a Single Subtraction – version II (QUIPSS II). In this scheme the inversion band is saturated with two additional RF pulses that destroy the signal of the perturbed spins left in the inversion band after an initial inversion time (TI_1). The implication of this is that TI_1 defines the duration of the labelled bolus: labelled blood starts to leave the inversion band directly after the PICORE inversion pulse and at TI_1 no more labelled blood leaves the inversion band. Note that, as long as TI_1 is shorter than the time it takes for the trailing edge of the labelled bolus to reach the proximal end of the inversion band, this leads to a labelled bolus with a width defined by time (i.e. TI_1). A schematic of this imaging technique can be seen in Figure 2.8.

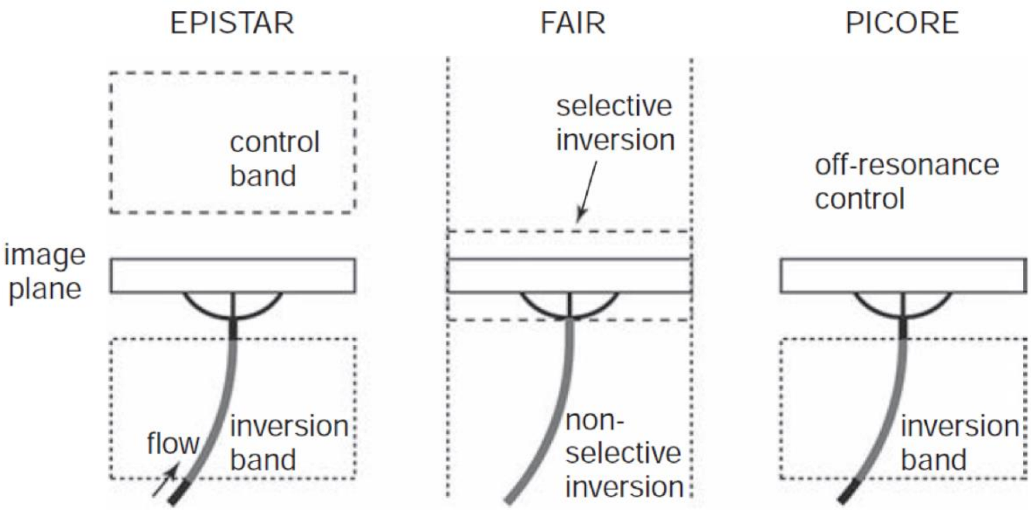

Figure 2.7. Schematic of the three main methods for PASL. All three methods are designed such that the static spins in the image plane sense the same magnetisation in the label and control images. In EPISTAR and PICORE the label image is acquired after a proximal inversion band, while in FAIR the label image is acquired after non-selective, global inversion of hydrogen spins. The control image in EPISTAR is acquired after application of the same inversion band superior to the image plane while in FAIR the control image is acquired after inversion of only the image plane. In both EPISTAR and FAIR the control image may have signal from labelled spins that have entered the image plane from above. PICORE does not have this issue, because the control image is acquired without inversion of spins, but with an off-resonance RF pulse. *Image from "Introduction to Functional Magnetic Resonance Imaging" by R.B. Buxton, Fig. 13.3*[25].

The kinetic curve of the PASL signal

The signal difference generated by subtraction of the tag from the control image is proportional to the amount of blood delivered to the tissue, but requires further calculations to be quantified as cerebral blood flow in ml/100 g/min. Figure 2.9 illustrates the difference signal over time in an image from a PASL experiment with a QUIPSS II cut off. Note that there are three phases to this curve[12]: (1) there is no signal before labelled blood has arrived in the image. (2) After the transit time (Δt), i.e. the time it takes the labelled blood to travel from the distal end of the inversion band to the image plane, labelled spins start to arrive in the image for the duration of the bolus (TI_1). (3) After all the labelled spins have arrived, signal decays away over time because of relaxation of the longitudinal magnetisation and because of venous clearance.

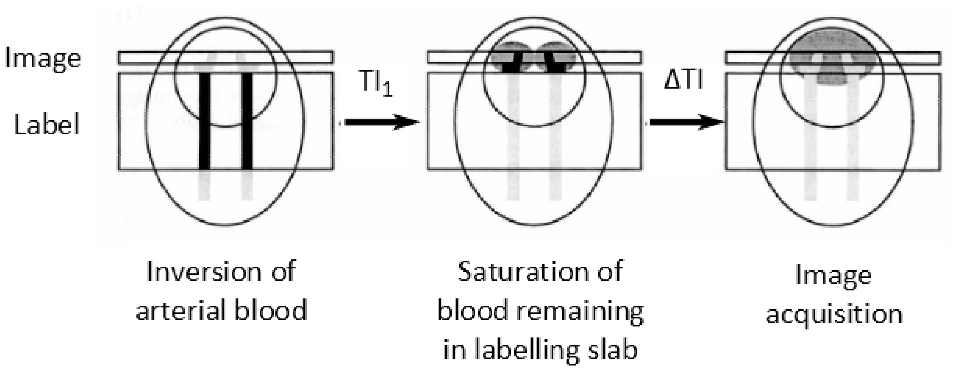

Figure 2.8. Schematic of PICORE labelling with a QUIPSS II cut off. Inversion of the blood takes place with a brief, spatially selective pulse below the imaging plane. After a certain time delay (TI$_1$) the inverted blood remaining in the labelling slab is saturated again, i.e. the arterial blood flowing out of the labelling slab after this inversion will no longer have inverted longitudinal magnetisation. An image is acquired after a certain delay time (ΔTI), such that the inversion time of the pulse sequence is equal to the sum of TI$_1$ and ΔTI. In the schematic large arteries are represented by light grey lines, labelled blood is represented by thick black lines, labelled spins that have perfused brain tissue are in dark grey. *Image adapted from Wong et al.*[13]

The kinetic curve from Figure 2.9 has a mathematical description that takes the processes of the labelled spins into account (delivery, exchange between blood and tissue, and relaxation)[12]:

$$\Delta M(t) = \begin{cases} 0 & t < \Delta t \\ \frac{2\alpha M_{0,blood} f e^{-\frac{t}{T_{1app}}}}{R}\left(e^{Rt} - e^{R\Delta t}\right) & \Delta t \leq t \leq \Delta t + \tau \\ \frac{2\alpha M_{0,blood} f e^{-t/T_{1app}}}{R}\left(e^{R(\Delta t+\tau)} - e^{R\Delta t}\right) & \Delta t + \tau < t \end{cases} \qquad \text{Eq. 2.4}$$

$$R = \frac{1}{T_{1app}} - \frac{1}{T_{1,blood}}$$

$$T_{1app} = \frac{1}{T_{1,tissue}} + \frac{f}{\lambda}.$$

In Eq. 2.4, *f* is the cerebral blood flow, $M_{0,blood}$ is the equilibrium magnetisation of blood, α is the labelling efficiency of the inversion, $T_{1,blood}$ and $T_{1,tissue}$ are the relaxation constants of hydrogen spins in blood and tissue, τ is the bolus duration, and λ the tissue-blood partition coefficient, indicating the volume of blood per gram of brain tissue (λ = 0.9 ml/g)[12]. Note that Eq. 2.4 illustrates that PICORE PASL with a QUIPSS II cut-off is performed with a 180° pulse that causes inversion of the equilibrium magnetisation of blood and that therefore the signal is proportional to 2*$M_{0,blood}$ multiplied with the labelling efficiency of the inversion (α = 0.90

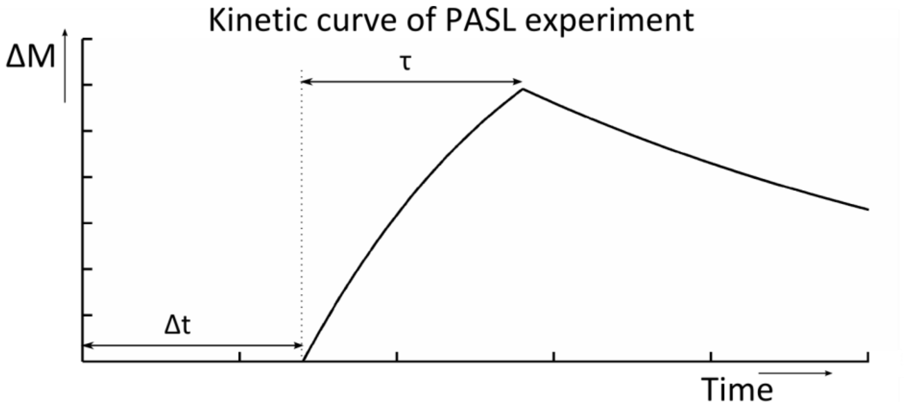

Figure 2.9. Schematic of kinetic curve of the difference signal (ΔM) in an image from a PASL experiment, when labelling takes place at t = 0. Note the three phases over time: there is no signal before labelled blood arrives in the image. At t = Δt the leading edge of the bolus arrives and the difference signal increases for the duration of the labelled bolus (τ). After arrival of the trailing edge of the bolus (t = Δt + τ) signal starts to decay away due relaxation of the longitudinal magnetisation of the labelled spins and due to venous clearance.

for PASL[12]). The amount of signal present in the imaging volume of interest also depends on the amount of blood delivered (or the cerebral blood flow), which is why the kinetic curve is scaled by the factor $2\alpha M_{0,blood}f$.

Furthermore, in Eq. 2.4 the factors R and $T_{1,app}$ are introduced for ease of notation[12,26]. These relaxation factors take into account that the longitudinal magnetisation decays away with the T_1 relaxation constant of arterial blood as soon as the inversion pulsed is switched off. When the arterial blood arrives in the image, it is assumed that immediate exchange of hydrogen takes place between the blood and the brain tissue, and therefore relaxation occurs with the T_1 relaxation constant of tissue. However, venous clearance of the labelled blood has a small effect on the relaxation time of the labelled hydrogen spins in tissue, which is why the relaxation time is modulated by the fraction of total tissue water leaving per second (i.e. $T_{1,app}$ contains the modulation with f/λ)[12].

The equilibrium magnetisation for blood can be measured in a voxel filled with arterial blood, without any tissue present. However, in practice it is difficult to have such a voxel when imaging the human head. Instead $M_{0,blood}$ is commonly calculated based on a calibration scan in which the equilibrium magnetisation of another tissue is determined, for which voxels are present that only contain this type of tissue, e.g. cerebrospinal fluid or white matter[13]. To determine the longitudinal magnetisation of the reference tissue a single repetition time (TR) scan is performed (effectively TR = ∞), such that there is no saturation of the reference tissue.

The kinetic curve from Figure 2.9 describes the signal of a voxel only containing tissue, in which an immediate exchange of the labelled hydrogen spins into the brain parenchyma is assumed when labelled blood enters the image voxel. Although this models works well for the majority of voxels within the brain, there are also voxels that have a substantial macrovascular compartment. As a result, early signal within these voxels originates from labelled arterial blood that is to perfuse more distal brain areas or will perfuse the brain tissue within the same voxel (illustrated by Figure 2.10). Fitting the single compartment model (Eq. 2.4) to the kinetic curve of voxels with a macrovascular compartment results in overestimation of cerebral blood flow. Chappell et al. have therefore introduced an extension to the single compartment model that fits the arterial blood volume fraction within the voxel[26]:

$$\Delta M(t) = \Delta M_{tiss}(t) + \Delta M_{art}(t) \tag{Eq. 2.5}$$

where $\Delta M_{tiss}(t)$ is described by Eq. 2.4 and $\Delta M_{art}(t)$ models the passing arterial bolus assuming plug flow:

$$\Delta M_{art}(t) = \begin{cases} 0 & t < \Delta t_{art} \\ 2\alpha M_{0,blood} e^{-t/T_{1,blood}} aBV & \Delta t_{art} \le t \le \Delta t_{art} + \tau_{art} \\ 0 & \Delta t_{art} + \tau_{art} < t \end{cases} \tag{Eq. 2.6}$$

where aBV is the arterial blood volume fraction of the voxel, Δt_{art} is the arrival time of the labelled bolus in the macrovasculature of the voxel and τ_{art} the duration of the labelled bolus. Eq. 2.6 models the arterial compartment under the assumption of plug flow and the relaxation of the spins within the label occurs with the T_1 relaxation time of blood.

In Chappell's model the macrovascular compartment is modelled assuming plug flow, i.e. there is an instant rise in signal when labelled blood arrives in the voxel and an instant decrease in signal at the end of the bolus duration (Figure 2.10). However, different models of this arterial input function exists that take dispersion of the labelled bolus into account, by convolution of Eq. 2.6 with a Gaussian kernel,[27] or assume laminar flow[28]. However, these

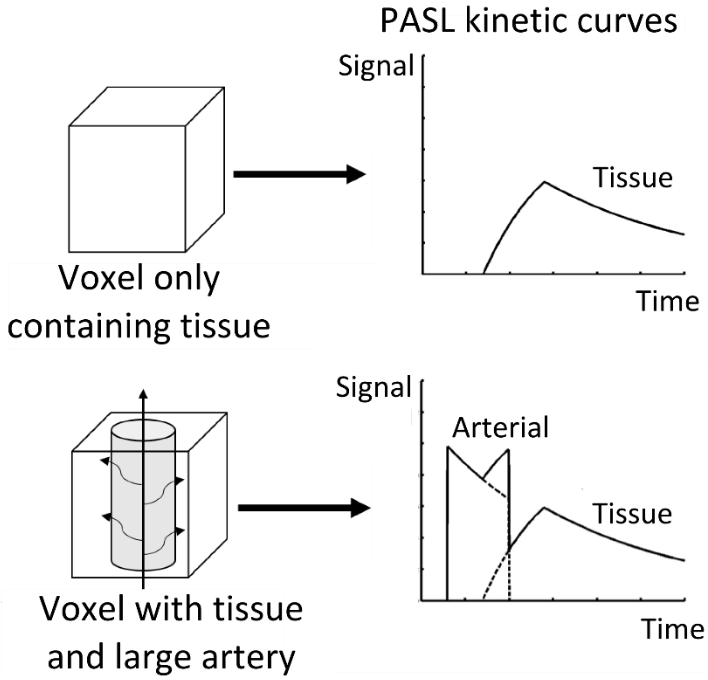

Figure 2.10. Schematic of voxels without and with a relatively large arterial compartment and their PASL kinetic curves. Top: for a voxel without large arteries PASL signal can be modelled with a single compartment model to assess tissue perfusion, as introduced by Buxton et al.[12]. Bottom: The kinetic curve of a voxel with a large artery (solid line) will have an early arterial component, which represents labelled blood flowing through the voxel (arrows) that is either going to perfuse distal brain tissue or is going to traverse the vasculature within the voxel to perfuse the local tissue. Fitting a single compartment model to the kinetic curve of the bottom voxel will overestimate local tissue perfusion. Chappell et al.[26] therefore introduced a two compartment model that fits the macrovascular component and estimates the volume fraction of the voxel that contains large arteries. The two compartments fitted by Chappell's model are printed in dashed lines.

more elaborate models of the arterial input function require one or more parameters to be fit in addition to the Δt_{art} and aBV, which either requires more data to be collected or assumptions to be made on some of the parameters included in the analysis. An example is the Gaussian dispersion on the labelled bolus that Wu et al. use[27], which introduced the extra parameter of the width of the Gaussian convolution kernel introduced to Eq. 2.6. Instead of fitting this parameter, Wu et al. use 3 different values for the width of the kernel and use the best match to model the arterial input function. Wu et al. mention that fitting of the width of the Gaussian curve results in unreliable estimations of this parameter due to large variation in the ASL data.

Sampling of kinetic curve

In a PICORE experiment with a QUIPSS II cut-off there are four unknown parameters when fitting Eq. 2.5: *f*, aBV, Δt and Δt_{art}. Note that because of the QUIPSS II cut-off the bolus duration is set ($\tau = \tau_{art} = TI_1$), $M_{0,blood}$ is estimated via a calibration scan, and the remainder of parameters are taken from the literature (labelling efficiency, tissue-blood partition coefficient, and T_1 relaxation times). Having four unknown variables means that in a PASL experiment there need to be at minimum four measurements along the kinetic curve to not have an underdetermined model, without having to make an assumption on any of the unknown parameters. It is because of this that many PASL experiments are multi inversion time experiments, which means that the kinetic curve of the imaging volume is sampled at different time points after labelling.

2.3 Techniques to measure arterial blood volume

Estimating the arterial blood volume fraction is important for measurement of arterial compliance. Although PICORE with a QUIPSS II cut-off in combination with Chappell's two compartment model can assess arterial blood volume, as described above, other MRI methods exist that measure arterial blood volume non-invasively. A brief overview of these methods is given here.

Combination of ASL preparations with a Look-Locker read-out can be used to assess cerebral arterial blood volume[29,30]. The Look-Locker read-out allows rapid sampling of the inversion recovery from the labelled spins, because it acquires the same image at different inversion times in a single repetition time[29,31]. Using a Look-Locker read-out makes the PASL signal more sensitive to the macrovascular compartment, because each acquisition within a repetition time destroys the longitudinal magnetisation of the labelled blood resulting in low signal to noise when the labelled blood arrives in the microvasculature. A specific model is needed that fits the PASL kinetic curve taking the decay of signal due to the Look-Locker read-out into account. Brookes et al. created such a model, based on their combination of pulsed ASL modalities (FAIR and EPISTAR) with a Look-Locker read-out to assess arterial blood volume[29]. One drawback of Brookes' approach is that the Look-Locker read-out in principle is a single slice acquisition and it is difficult to acquire multiple slices because of the short spacing between the read-out pulses (<100 ms[29,32]) and the requirement to adapt the kinetic curve model to include the effects of the read-out pulses of neighbouring slices[29].

However, using a Look-Locker read-out does enable the acquisition of dynamic angiography images with ASL signal weighting, as done by Günther et al.[33] and Okell et al.[30,32]. By introducing flow compensation to the Look-Locker read-out sequence signal from static spins is suppressed, which increases sensitivity to signal from large arteries in Look-Locker acquisitions even further[34]. Moreover, the pulse sequence used by Okell et al.[32] uses a vessel-encoded pseudo continuous ASL[35] inversion of arterial blood, which enables measurement of the origin of arterial blood volume fraction. As an example, the mixing of blood in the basilar artery originating from the left and right vertebral arteries can be assessed with vessel-encoded dynamic angiography[32]. Including the appropriate model, again taking the longitudinal decay of the label because of the read-out pulses into account, allows for quantification of the arterial blood volume fraction within the vessels[30].

The arterial blood volume fraction can also be measured without the use of a model, but by including vascular crushing with bipolar gradients in the ASL imaging sequence[36,37]. Bipolar gradients, i.e. combinations of a positive and negative gradient of equal size, attenuate signal in voxels with flowing spins. In case a voxel only contains stationary spins applying a spatially localized gradient followed by the same gradient with opposite direction does not have a net effect on voxel intensity because all spins undergo the same amount of rephasing and dephasing. However, when a voxel contains flowing spins the application of such a bipolar gradient will decrease voxel intensity because of the net phase difference between flowing and stationary spins[38]. The size of this phase difference depends on the velocity of the spins, i.e. the higher their velocity the bigger the net phase difference, and on the strength of the bipolar gradient moment, with a stronger moment also leading to a larger phase difference. The maximum velocity that can be detected unambiguously is often denoted by v_{enc} and is usually set to 3 cm/s to crush the signal from large arteries in ASL experiments[36,39].

In order to measure the macrovascular compartment with vascular crushing, two ASL series need to be performed: one in which the kinetic curves are determined without bipolar gradients and one in which the kinetic curves are assessed with bipolar gradients. The difference between these two curves gives the macrovacscular kinetic curve, i.e. blood in large arteries is flowing faster than the v_{enc}. Petersen et al. use this method to calculate voxel wise arterial blood volume fractions by calculating the ratio of the area under the macrovascular kinetic curve to the area under a theoretical kinetic curve of a blood filled voxel[36]. The latter is determined by correcting the equilibrium magnetisation of a voxel filled with venous blood in the sagittal sinus, to obtain the equilibrium magnetisation of oxygen rich arterial blood[36].

A combination of ASL with a balanced steady state free precession (bSSFP) read-out module has also been proposed to assess arterial blood volume[40]. In bSSFP a train of radiofrequency pulses is used to create a non-zero steady state of both the longitudinal and transverse magnetisations[9]. The steady state signal of any tissue in bSSFP is governed by its T_2/T_1 ratio, as well as the repetition time and flip angle of the radiofrequency pulses used to create the steady state[9,40]. Yan et al.[40] use a FAIR labelling scheme in combination with a single slice bSSFP read-out, in which signal from arterial blood is high due to the relatively high ratio of T_2/T_1 of arterial blood (0.165s/1.6s[41]) compared to blood in tissue (0.08/1.3s[1]). In their experiment, Yan et al. use a combination of flip angle and repetition time that saturates the signal from the static brain tissue, including blood arriving in the capillary bed of brain tissue, even further enhancing the signal to noise ratio of inflowing labelled blood[40,42]. Furthermore, Yan et al. use a multiphase bSSFP read-out that allows voxel wise sampling of the PASL signal curve with 27 time steps of 92 ms after a single FAIR inversion pulse[40]. The resulting arterial signal curve is divided by a theoretical signal curve from an arterial blood filled voxel to obtain quantified maps of arterial blood volume, in a similar manner as in the model free approach used by Petersen et al.[36]

Inflow vascular-space-occupancy with dynamic subtraction (iVASO-DS)[43] is a method similar to the FAIR technique and aims to quantify the precapillary arterial blood volume. iVASO-DS is based on vascular-space-occupancy (VASO), an imaging technique that was introduced to provide cerebral blood volume maps in blood oxygenation-level dependent imaging[44]. In VASO an image in which inflowing blood is nulled is acquired by a non-selective inversion (180°), directly followed by another slice selective 180° pulse before image acquisition.

Effectively, in this so-called ‘nulled’ image the static spins have not undergone magnetic inversion, while flowing spins originating from outside the slice have undergone inversion. The time of image acquisition is set such that the magnetisation of the spins in the blood is nulled, meaning that the only remaining signal comes from extravascular hydrogen spins. In iVASO-DS an additional control image is acquired with no inversion of blood signal, and therefore signal is present from tissue and blood[43]. The difference between the control and nulled image therefore is proportional to the amount of arterial blood volume, which is quantified by calculation of $M_{0,blood}$ in a similar manner as in the ASL perfusion quantification as described in the previous section.

2.4 Overview of developments of PASL included in this thesis

Overcoming low SNR of brainstem imaging

One of the key structures involved in regulation of cerebrovascular physiology is the brainstem. However, perfusion imaging of the brainstem itself is difficult. Part of the problem in brainstem PASL imaging is the intrinsically low signal to noise ratio of ASL caused by the natural refresh rate of blood within the brain. The average human cerebral blood flow is approximately 60 ml/100 g/min[25], which means that per second only 1 ml of fresh blood is delivered to 100 ml of tissue. The latter means that the signal difference of interest during ASL imaging is only about 1 % of the overall signal intensity[45]. In addition to the intrinsically low SNR in ASL, the brainstem suffers from signal loss because of magnetic field inhomogeneities caused by the nearby sphenoid sinus. Another important aspect in brainstem imaging is including Chappell’s two compartment model, because the arterial contribution to the PASL signal is relatively large due to cerebrovasculature surrounding the brainstem. Chapter 4 contains the developments made to address the challenges of brainstem ASL imaging.

Synchronising measurement of aBV with cardiac cycle

One non-invasive measure of cerebrovascular health is arterial compliance of cerebral arteries, which requires measurement of arterial blood volume at different pressure levels.

From the methods to assess arterial blood volume described in the previous section, only the combination of FAIR with balanced steady state free precession has been synchronized with the cardiac cycle[46]. Yan et al. have shown the feasibility of using the differences in arterial blood volume over the cardiac cycle, i.e. in systole and diastole, to assess cerebral arterial compliance[46]. However, one drawback of their method is that it is a single slice method, which is difficult to extend to a 3D acquisition because this would require speeding up the read-out duration; a larger volume needs to be covered before the signal of the inversion pulse decays away[42]. Currently, it takes approximately 3 minutes to acquire an arterial blood volume map of a single slice with dynamic angiography with a balanced steady state free precession read-out[40], which makes acquisition of multiple slices with separate scan series inefficient.

In this thesis a non-invasive method to assess arterial compliance of cerebral arteries is introduced in chapter 6, which uses a PICORE pulsed ASL sequence in combination with a multi-slice spiral gradient echo acquisition scheme. Retrospective synchronisation of the PASL images with the cardiac cycle is used to assess arterial blood volume in systole and diastole. Arterial compliance is calculated by dividing the difference in arterial blood volume between systole and diastole by the difference in blood pressure (pulse pressure).

Chapter 3

Sympathetic regulation of the cerebrovasculature

Whether sympathetic regulation of the cerebrovasculature is a significant factor in maintaining adequate cerebral blood flow is still a matter of debate. Although a lot is known about the anatomical pathways and key structures involved in generating sympathetic nerve activity, for instance that the brainstem contains nuclei that play an important role in the sympathetic nervous system, this knowledge is mainly based on animal or ex-vivo human data. Verification of the effects of sympathetic nerve activity on human cerebrovasculature has yet to be carried out in vivo and this chapter addresses why it is important to do so. However, first an overview is given of the structure of the cerebrovasculature, sympathetic nervous system and the brainstem.

3.1. Cerebrovascular anatomy

Major cerebral arteries

The internal carotid (ICA) and vertebral arteries (VA) are the main arteries supplying arterial blood to the brain. The internal carotid arteries originate from the common carotid arteries, located bilaterally in the neck, while the vertebral arteries branch from the subclavian arteries and run through the cervical portion of the spinal cord. The vertebral arteries anastomose at the level of the brainstem to form the basilar artery, which bifurcates at the level of the midbrain (in the brainstem) to form the left and right posterior cerebral arteries. Both internal carotid arteries bifurcate to form the middle and anterior cerebral arteries. The Circle of Willis is an important anastomosis formed by the communicating arteries between the posterior and middle cerebral arteries, and between the middle and anterior cerebral arteries. An example of the cerebrovasculature, together with a schematic overview of the major cerebral arteries, can be seen in Figure 3.1.

Cerebral arterial walls

The cerebral arterial walls consist of three layers: (1) the inner tunica intima, containing a single layer of endothelium cells and the internal elastic lamina; (2) the tunica media, which contains smooth muscle cells, elastin, and collagen fibres; (3) the outer tunica adventitia, which mostly contains collagen fibres and perivascular nerves[47]. In cerebral arteries the tunica adventitia is small compared to peripheral arteries. Instead the cerebral arteries have a larger tunica media with a large number of smooth muscle cells. For instance, the internal carotid arteries can have up to 20 layers of smooth muscle cells in the tunica media. The number of layers of smooth muscle cells progressively declines along the cerebral vascular tree, with the penetrating arterioles only having a single layer of smooth muscle cells, illustrated in Figure 3.2[47]. The tunica adventitia of the large cerebral arteries contains a dense structure of perivascular nerves originating from the peripheral nervous system. Like the layers of smooth muscle cells, the density of perivascular nerves decreases along the cerebrovascular tree. The pial arteries, i.e. arteries on the surface of the cortex, are still innervated by perivascular nerves while the penetrating (or intracerebral) arterioles are solely innervated by neurons originating from areas within the brain[47–49].

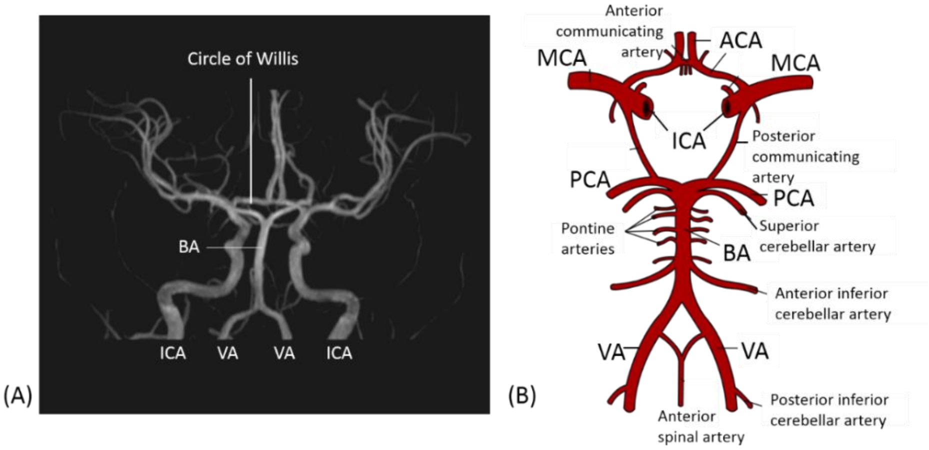

Figure 3.1. (A) Time of flight angiogram of healthy cerebrovasculature. The main supply of arterial blood comes from the internal carotid (ICA) and vertebral arteries (VA). The VA joins up at the level of the caudal pons to form the basilar artery (BA), which together with the ICA supplies the Circle of Willis. The major arteries branching from the Circle of Willis are the anterior (ACA), middle (MCA) and posterior (PCS) cerebral arteries. (B) Schematic of the major cerebral arteries. *(Schematic adapted from Gray's Anatomy*[50]*.)*

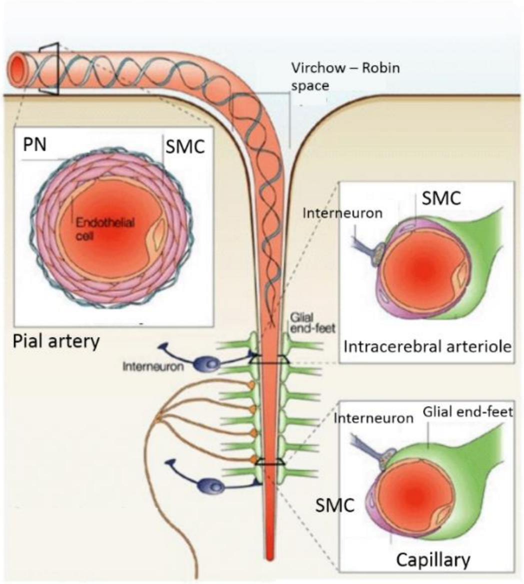

Figure 3.2. Pial arteries have a dense structure of perivascular nerves (PN, blue) originating from the peripheral nervous system in the outer layer (tunica adventitia). The thick middle layer (tunica media) consists of smooth muscle cells (SMC, purple), elastin and collagen fibres (the latter two not shown in the figure). Both the outer layer and the tunica media become progressively thinner along the vascular tree; the intracerebral arterioles and capillaries are innervated by neurons originating within the brain (interneurons originating in the cortex and neurons originating from sub-cortical areas), have a single layer of smooth muscle cells, and are surrounded by glial end-feet (such as from astrocytes). *Figure from Cipolla et al.*[47]

In addition, the density of perivascular nerves is heterogeneous over the brain, with the internal carotid arteries being more densely innervated by perivascular nerves than the vertebral and basilar arteries[51].

3.2. Structure of the sympathetic nervous system

The autonomic nervous system (ANS) controls the smooth muscle cells (SMC) and glands in the human body and is not subject to voluntary control[52]. The ANS contains the sympathetic (SNS) and parasympathetic nervous system, which broadly function as antagonists[52]. The SNS is commonly known as the “fight or flight” division of the ANS because increased sympathetic nerve activity (SNA) will lead to an “excited state” with physiological features such as increased blood pressure (BP) due to vasoconstriction and elevated heart rate, inhibition of the digestive system, deep breathing, and dilated pupils[53,54]. The parasympathetic nervous system is responsible for maintaining homeostasis at rest and parasympathetic effects on organs are therefore often counteracting sympathetic effects; increased parasympathetic nerve activity causes vasodilation, decreased heart rate, stimulation of the digestive system and constricted pupils[52,53].

In both the sympathetic and parasympathetic nervous systems innervation pathways controlling the SMC and glands consist of only two neurons: a preganglionic neuron originating in the brainstem or spinal cord and ending in a peripheral ganglion, i.e. cluster of nerve cells, and a postganglionic nerve fibre that originates from a peripheral ganglion and ends in a plexus in close vicinity of SMC or glands (see Figure 3.3)[52]. Both preganglionic fibres, as well as the postganglionic fibres in the parasympathetic nervous system, use acetylcholine as a neurotransmitter[52]. The postganglionic neurons in the sympathetic nervous system use norepinephrine as neurotransmitter, which is released in the vicinity of SMC from swellings in the neuronal plexus[52,53]. Because norepinephrine is also known as noradrenaline, sympathetic postganglionic neurons are often referred to as adrenergic fibres[53]. Another potent sympathetic neurotransmitter is neuropeptide Y, which is released from varicosities in the sympathetic plexus in a similar manner as norepinephrine[48,49].

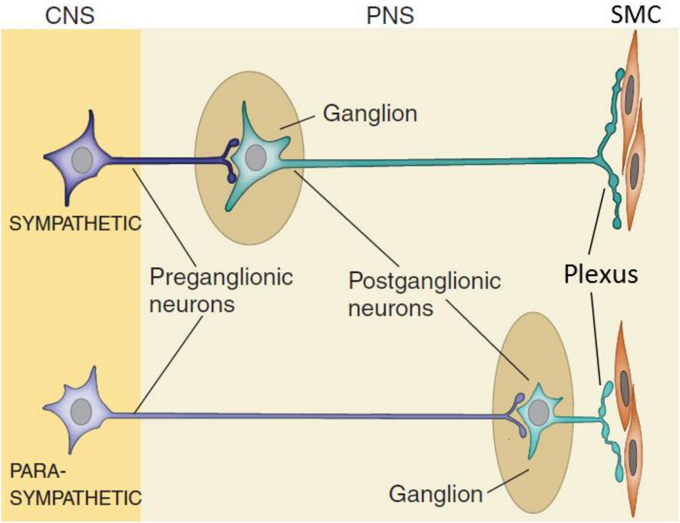

Figure 3.3. Both sympathetic and parasympathetic pathways consist of two neurons; a preganglionic neuron originating in the central nervous system (CNS) and a postganglionic neuron in the peripheral nervous system (PNS). All neurons use the neurotransmitter acetylcholine, except for the postganglionic sympathetic neurons. The latter are also called adrenergic neurons because they use the neurotransmitter norepinephrine (also called noradrenaline). The postganglionic neurons form a plexus in the vicinity of the smooth muscle cells (SMC). Note that this schematic does not show that in a ganglion there are always more postganglionic neurons originating than preganglionic neurons terminating. *Figure adapted from Figure 28.1 in "The central nervous system: structure and function" by Per Brodal*[52].

The sympathetic perivascular nerves innervating the internal carotid arteries originate from the superior cervical ganglion, located in the peripheral nervous system adjacent to the C2 and C3 discs of the spinal cord. As illustrated by Figure 3.4, the sympathetic preganglionic neurons that end in the superior cervical ganglion originate from the first thoracic spinal disc (T1) within the central nervous system[48,52]. The sympathetic nerves innervating the vertebral and basilar arteries originate from the stellate ganglion[49].

3.3. Anatomy of the brainstem

The brainstem is located inferior to the cerebrum and superior to the spinal cord. The brainstem contains many structures and nuclei involved in critically important physiological processes in the human body and because of its location it functions as an important relay station[55]. However, in the following an overview is given of the anatomy that solely focuses on the nuclei of the brainstem important for generating sympathetic nerve activity. For an

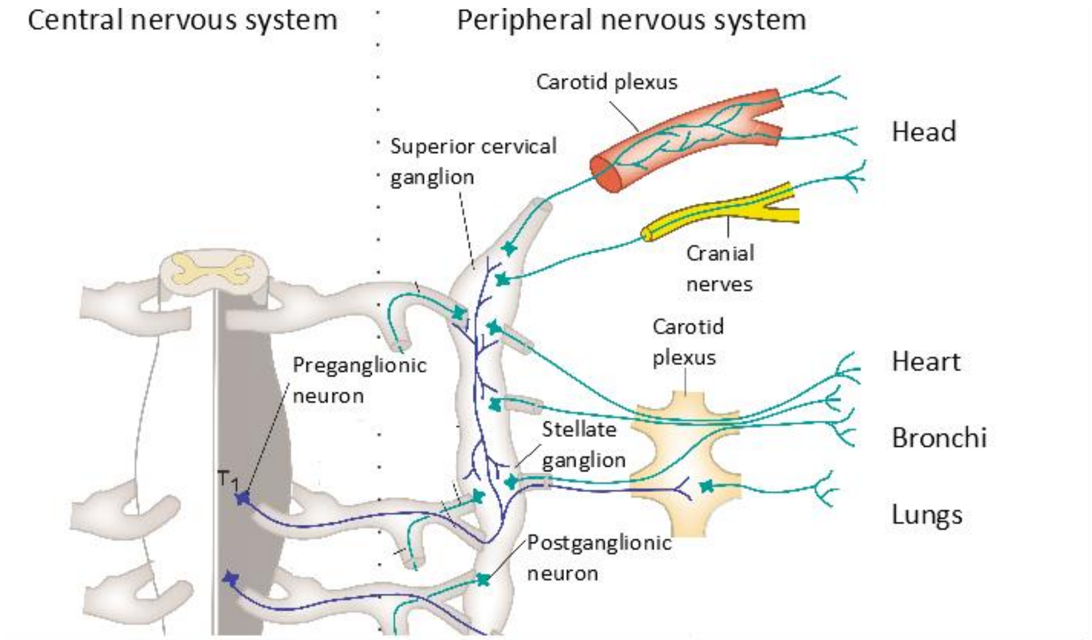

Figure 3.4. Schematic overview showing the origin of sympathetic perivascular innervation of the cerebrovasculature. Sympathetic preganglionic neurons leave from the first thoracic spinal disc (T1) to reach the superior cervical ganglion, which is located in the peripheral nervous system, but is adjacent to the second and third cervical spinal discs (C2 and C3). Sympathetic postganglionic neurons leave the superior cervical to innervate the heart, head and cerebral vessels. Note how the schematic here shows the carotid plexus at the internal carotid artery, but this sympathetic plexus continuous along the cerebrovascular tree until the pial arteries. It only disappears at the level of the intracerebral arterioles and capillaries (see Figure 3.2). Note that in addition to innervating the heart, bronchi and lungs, there are postganglionic neurons from the stellate ganglion to the vertebral and basilar arteries, which are not included in the schematic here. *Figure adapted from Figure 28.7 in "The central nervous system: structure and function" by Per Brodal.*[52]

elaborate description containing all nuclei and functions of the brainstem the reader is referred to *Duvernoy's Atlas of the Human Brain Stem and Cerebellum*[55].

The brainstem is subdivided into three segments (Figure 3.5): the most ventral segment is called the medulla oblongata (or simply medulla), superior to the medulla is the pons, and the most dorsal segment is called the mesencephalon (or midbrain). The brainstem mostly contains white matter, which consists of myelinated neurons of the central nervous system. Clusters of neuronal cell bodies form the brainstem nuclei (grey matter) and are found scattered throughout the three segments of the brainstem[56]. The blood supply in the medulla mainly originates from the anterior spinal artery, while arteries supplying the pons mainly

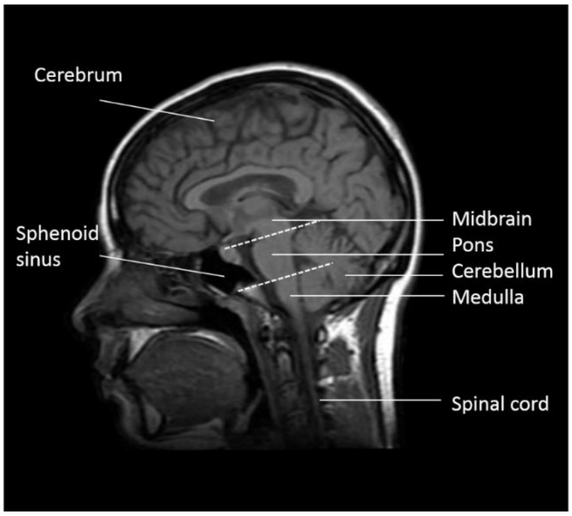

Figure 3.5. T1 weighted MRI of the brain (sagittal slice). The brainstem connects the cerebrum with the cerebellum and the spinal cord. It consists of three segments: the medulla oblongata (medulla), pons, and mecencephalon (midbrain). Note that the brainstem is located closely to the sphenoid sinus.

branch from the basilar artery, and arteries branching from the posterior cerebral arteries supply the midbrain (see Figure 3.1B)[55].

The main sympathetic centres are located in the medulla of the brainstem (Figure 3.6)[55]. The nucleus of the solitary tract (*Latin: nucleus tractus solitarus*, NTS) lies centrally in the medulla and is segmented in three portions: the rostral (rNTS), mid (mNTS), and caudal (cNTS) segments. The NTS is the principal afferent system in the brainstem and receives nerve fibres that are important for autonomic processes, such as respiratory and cardiovascular control. An important note is that the NTS mainly contains parasympathetic centres, but that these are modulated by sympathetic centres that are located intertwined with the dorsal motor nucleus of the vagus (DMV). In addition, the mNTS projects onto the sympathetic centres in the ventrolateral medulla (VLM), which are the rostral (RVLM) and caudal (CLVM) nuclei in the ventrolateral medulla. The RVLM in turn has efferent fibres that project onto the sympathetic centres in the spinal cord via the tractus intermediolateralis.

The brainstem is well connected with higher brain regions[57]. One of the important connections of the autonomic nuclei in the medulla is the dorsal longitudinal fasciculus (DLF), a nerve fibre running between the caudal NTS and hypothalamus (see Figure 3.6)[55]. Via this nerve fibre, the hypothalamus can mediate (para)sympathetically regulated processes such as blood pressure, heart rate and respiratory control[57]. Other regions of the brain that are known to mediate these physiological processes have projections to the hypothalamus, via which they stimulate the sympathetic nuclei in the brainstem[58]. The anterior cingulate cortex, for instance, mediates autonomic processes such as increasing blood pressure or heart rate in emotional or cognitive stress[58]. In addition, the cerebellum has reciprocal connections[59] with the hypothalamus and has been shown to be mediating autonomic processes[60].

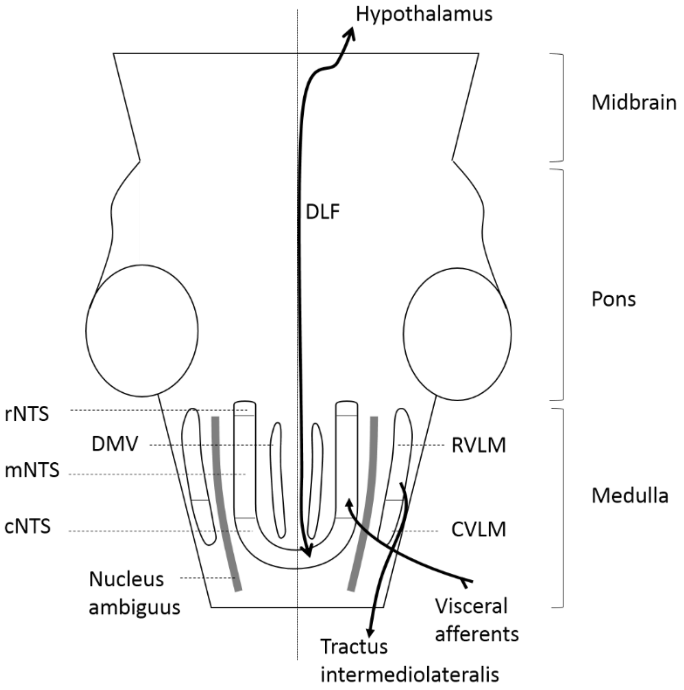

Figure 3.6. Schematic of coronal section of the brainstem illustrating the main (para)sympathetic nuclei within the medulla. The dorsal motor nucleus of the vagus nerve (DMV) lies in the dorsomedial medulla. The nucleus of the solitary tract (NTS) is divided in three portions: the rostral (rNTS), mid (mNTS), and caudal (cNTS) portions. The ventrolateral medulla has two portions: rostral (RVLM) and caudal (CVLM). Many interconnections exists between the dorsomedial and ventrolateral nuclei in the medulla. The mNTS receives afferent fibres important in respiratory and cardiovascular control. The autonomic nuclei of the brainstem receive information from higher brain regions via the dorsal longitudinal fasciculus (DLF), which connects the cNTS with the hypothalamus. The RVLM projects to the spinal sympathetic centres via the tractus intermediolateralis. *(Schematic adapted from Duvernoy's atlas of the human Brain Stem and Cerebellum, Fig 3.13)*

3.4. Sympathetic regulation of cerebrovascular tone

Active constriction or dilation of cerebral arteries is dependent on the tone of the smooth muscle cells within the arterial walls. Contraction of smooth muscle cells works via cross-bridge cycling between myosin and actin molecules, a process regulated by free calcium ions (Ca^{2+}) within the cells. Ca^{2+} activates an enzyme (myosin kinase) that regulates phosphorylation of a light chain on the myosin filament, which facilitates cycling of cross bridges between myosin heads and actin filaments leading to contraction of the SMC. Relaxation of smooth muscle cells occurs when the Ca^{2+} concentration within the cell decreases below a critical level, which activates myosin phosphatase, an enzyme that splits the phosphate from the myosin light chain, and results in detachment of the myosin head from the actin filaments[61,62]. A schematic of this process can be seen in Figure 3.7. Smooth muscle cells show a ‘latch’ system: after initiation of contraction there can be a balance between active myosin kinase and myosin phosphatase that results in an equilibrium in which there is no ‘cycling’ of myosin heads along the actin filaments. The level of constriction that is maintained in this equilibrium can vary and is referred to as the *tone* of the smooth muscle cell[49,61]. Note that the actin filaments are attached to so-called ‘dense bodies’ that are located throughout the cell and its membrane, illustrated by Figure 3.8.

Many mechanisms that influence smooth muscle cell tone affect the level of free Ca^{2+} within the cells. Via a variety of receptors and sensors in their membranes smooth muscle cells are susceptible to numerous factors in the blood (e.g. neurotransmitters, carbon dioxide, nitric oxide), to changes in mechanical stretch (e.g. changes in blood pressure), and to local factors in the surrounding extracellular matrix (e.g. ion concentrations, electrical coupling via the dense bodies, astrocytes, and pericytes)[61–64]. Here we focus on sympathetic regulation of the smooth muscle cell tone, which occurs independently from, but can be modulated by, the above factors. Sympathetic regulation of smooth muscle cell tone occurs via the release of neurotransmitters (mainly norepinephrine, but also neuropeptide Y) from the varicosities in the plexus surrounding the cerebral arteries (see section 3.2). These neurotransmitters bind to adrenergic α_1-receptors on the smooth muscle cells which facilitates an influx of Ca^{2+} ions through channels in the cell membrane and induces release of Ca^{2+} from the sarcoplasmic reticulum within the cell into the cytosol[49,61,65].

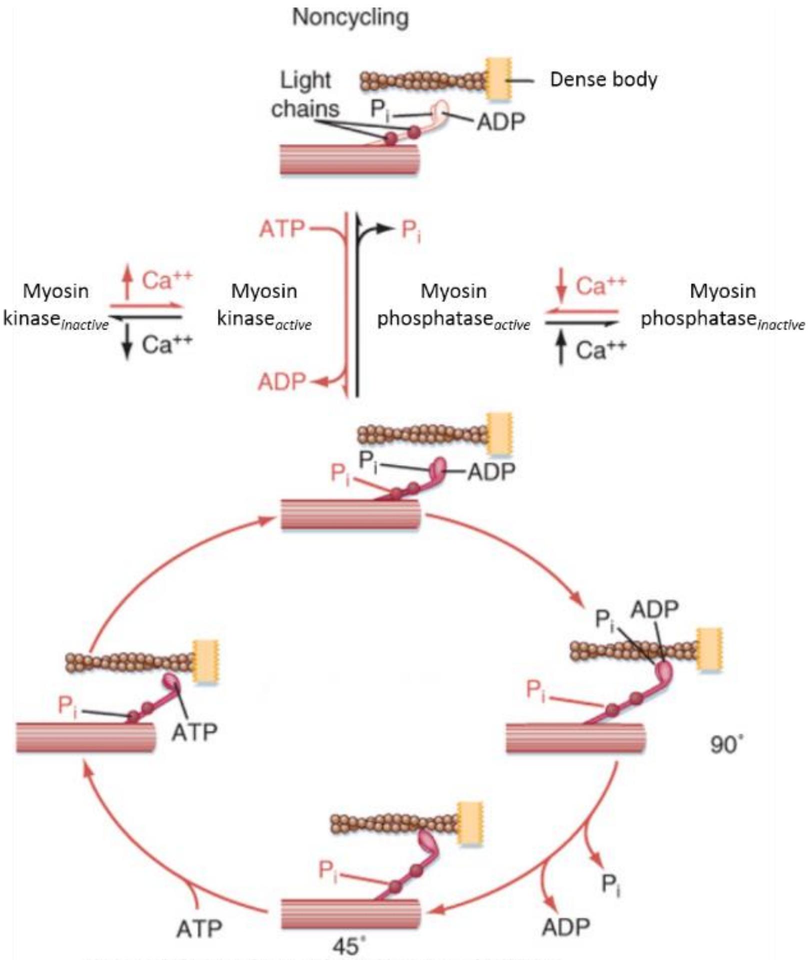

Koeppen & Stanton: Berne and Levy Physiology, 6th Edition.
Copyright © 2008 by Mosby, an imprint of Elsevier, Inc. All rights reserved

Figure 3.7. Schematic of contraction mechanism in smooth muscle cells. Contraction occurs because of cross-bridge cycling between myosin heads and actin filaments, the latter attached to a dense body (here yellow structures) within the cell. Cross-bridge cycling is enabled via Ca^{2+} induced activation of myosin kinase, which in turn phosphorylates one of the light chains on the myosin filament. While the myosin filament is phosphorylated, cross bridge cycling occurs; the myosin attaches to the actin filament, when bound adenosinediphosphate (ADP) and phosphate (P_i) are split from the myosin head, inducing a change in morphology of the myosin filament (decreasing the angle between the myosin head and the myosin body from 90 to 45 degrees). With binding of adenosinetriphosphate (ATP), the myosin head reattaches to the actin but on a different binding site, which means that the myosin and actin filaments are sliding alongside each other. The next cycle is initiated by splitting the ATP bound to the myosin head into ADP and P_i. When the free Ca^{2+} concentration drops below a threshold value, myosin phosphatase is activated. This enzyme splits the phosphate from the myosin light chain, which inhibits binding of the myosin head to the actin filaments. *(Image adapted from Koeppen & Stanton: Berne and Levy Physiology.*[66]*)*

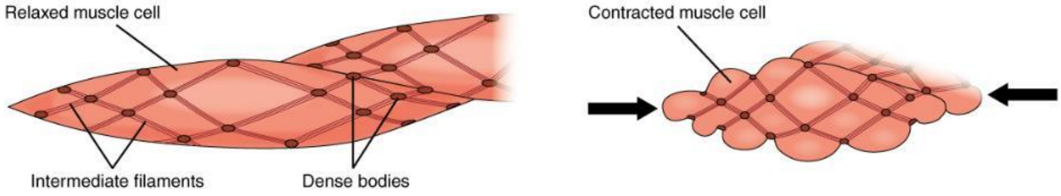

Figure 3.8. Schematic of smooth muscle cells in arterial walls. On the left cells are in relaxed state. Note that intermediate filaments connect dense bodies spread throughout the cells. The intermediate filaments contain contraction complexes consisting of actin and myosin filaments. Note that there are dense bodies coupling adjacent cells and facilitating transmission of contraction/relaxation. Upon activation of the contraction mechanism of the intermediate filaments these shorten and as a result the cells are in a contracted state, as illustrated on the right. *(Image from Human Anatomy & Physiology*[67]*)*

Release of sympathetic neurotransmitters is controlled by the RVLM: stimulation of the RVLM increases the release of neurotransmitters and inhibition causes a decrease in neurotransmitter release. In general, a stimulus that requires a need for a change in sympathetic outflow is sensed by the central or peripheral nervous system and transmitted to the nucleus of the solitary tract (NTS) in the dorsomedial medulla (Figure 3.6), which in turn leads to modulation of the RVLM. One well-known example of such a pathway is the baroreflex; baroreceptors in the aorta and common carotid arteries sense an increase in pressure, which is signalled to the NTS directly via visceral afferent nerves. The NTS then decreases stimulation to the caudal ventrolateral medulla (CVLM), which in turn leads to a decrease in inhibition of the RVLM. The RVLM therefore increases sympathetic nerve activity, which leads to cerebral (and peripheral) vasoconstriction.

3.5. Is non-invasive measurement of sympathetic regulation of cerebrovascular physiology needed?

In addition to sympathetic regulation, cerebral blood flow is influenced by other factors, such as blood pressure and blood gases, and there is controversy about the relative contribution of each of those at different physiological states[68]. For instance, the relationship between sympathetic activity and carbon dioxide levels in the blood remains uncertain, as there have been reports about changed[69] and unchanged[70] cerebrovascular reactivity to carbon dioxide due to increased sympathetic outflow. Moreover, because of such contradictory and heterogeneous effects of augmented sympathetic activity reported in the current literature controversy exists about whether or not the sympathetic nervous system plays a significant role in cerebral blood flow regulation at all[71]. Interestingly, as Ainslie and Brassard point out in their review, an important reason for this controversy is the current lack of in vivo human measurements that can directly measure the role of the sympathetic nervous system in cerebrovascular regulation[71].

Indeed, the majority of existing knowledge about the role of the sympathetic nervous system in regulation of cerebrovascular function and physiology is based on animal or ex vivo experiments, from which translation to in vivo human work is difficult. Firstly, there are confounding differences between species in sympathetic regulation of the cerebrovasculature. For instance, in humans and rats sympathetic regulation of cerebral smooth muscle cells mainly occurs via α_1 adrenergic receptors on the cell membrane, while in cats and dogs the majority of the adrenergic receptors on the cerebral smooth muscle cells are α_2-receptors[49]. Because α_2-receptors are less sensitive to norepinephrine, the implication of this is that the vasoconstrictive response to administration of norepinephrine is weak in cats and dogs compared to in humans[72]. In addition, there are important differences in anatomy between species. One example is that, unlike in humans, in rats the internal carotid arteries form an integral part of the Circle of Willis[73]. This means that the majority of blood flow to the rat brain originates from the carotids, while in man there is a considerable contribution of vertebral blood flow[74]. One implication of this difference in anatomy is that caution should be taken in translation of results from experiments with rats in which only the internal carotids or only the vertebral arteries are sympathetically stimulated.

Secondly, results from ex vivo experiments including human arteries are difficult to translate into in vivo function because of several factors, such as degradation of cerebral arteries after harvesting[75] and the difficulty of mimicking the complex in vivo environment[76]. The importance of experimental set-up when assessing the cerebrovasculature was highlighted by a study examining mechanical properties of rat carotid arteries in vivo, in situ and in vitro and significant differences in carotid distensibility were found between these three states[76]. Factors that influenced the in vitro (or ex vivo) changes in distensibility were the difference in shear stress induced by flowing blood compared to the solution used in vitro to mimic blood, the absence of vasoactive agents from arterial blood, and having the correct blood pressure oscillations[76]. Problematic with in situ experiments, e.g. open craniotomies, is that there are changes in transmural pressure and the amount of carbon dioxide when arteries are exposed[76,77]. Both of these factors influence the diameter of cerebral arteries, which confounds translation of in situ measurements to in vivo regulation of the cerebrovasculature.

In the literature cerebral blood flow velocity through the middle cerebral artery measured with transcranial Doppler ultrasound (TCD) is used to investigate sympathetic regulation of the cerebrovasculature in humans non-invasively[68,71]. For instance, changes in middle cerebral blood flow velocities during exercise and after pharmacological blockage of the superior cervical ganglion are attributed to sympathetic denervation[78]. A drawback of TCD is that it cannot give a measure that is directly related to sympathetic nerve activity because it cannot measure arterial geometry, such as volume or diameter, and changes in blood flow velocity can only be interpreted by making the assumption that there is no change in diameter of the middle cerebral artery[78–80]. Assessing the extent of sympathetic regulation of the human cerebrovasculature requires in vivo measurement of a direct effect of increased sympathetic nerve activity, such as the increase in tone of cerebrovascular smooth muscle cells. One option could therefore be measurement of the compliance of cerebral arteries, i.e. the change in volume of an artery given a change in pressure, which is inversely related to the stiffness of arterial walls (and tone of the smooth muscle cells). Note that due to the heterogeneous dispersion of sympathetic perivascular nerves in the cerebrovasculature it is of interest to have a measure that can assess compliance of individual cerebral arteries.

In investigating sympathetic regulation of cerebral blood flow another important factor is being able to assess the function and physiology of the medulla, because of the nuclei regulating sympathetic activity within this brain region (Figure 3.6). The first steps in assessing the function of the medulla in sympathetic regulation have been made by Macefield and his colleagues, who used simultaneous measurement of blood oxygenation-level dependent (BOLD) imaging and microneurography (a measurement of sympathetic outflow)[81–83]. This research group was the first to show in vivo that there are areas in the human brainstem that show activity correlated to the generation of sympathetic nerve activity. Moreover, Macefield et al. could even demonstrate a positive correlation between sympathetic nerve activity and the rostral ventrolateral medulla and negative correlation between sympathetic nerve activity within the caudal ventrolateral medulla and the nucleus of the solitary tract[83]. However, an important confound from BOLD imaging is that this signal is highly dependent on local hemodynamic parameters such as the amount of arterial blood present and the cerebral blood flow and therefore does not give quantitative measurement of cerebral physiology within the medulla[10].

Cushing's mechanism

The above paragraphs highlight the importance of having non-invasive measurements that can investigate the role of sympathetic nerve activity in healthy regulation of cerebrovascular physiology. However, such measurements are also important to tease apart mechanisms related to cerebrovascular pathology. A complete picture of the function and physiology of the medulla is of particular importance when it comes to in investigating *Cushing's mechanism*[84], a theory suggesting that long-term control of systemic blood pressure occurs via pressure sensitivity of the medulla. In this hypothesis it is suggested that hypoperfusion of the medulla induces increased sympathetic outflow to maintain adequate perfusion to the brainstem[84,85]. The term "Cushing's mechanism" has evolved from a wide range of experiments in animal and man coming from over a 100 years of research; Cushing himself showed in 1901 that compression of the brainstem in the ischemic brain of dogs drives up blood pressure leading to death (Cushing's *reflex*)[86], while recent human work has shown that in normotensive patients at risk of hypertension ("borderline" and "white coat" hypertensives) sympathetic nerve activity is already elevated before they become clinically hypertensive[87]. Within the framework of Cushing's mechanism the latter is explained by the increased cerebral arterial stiffness associated with hypertension, which increases cerebrovascular resistance of the vertebral and basilar arteries and therefore cause hypoperfusion of the brainstem, which in turn is responsible for the increase in sympathetic outflow[84,85].

Also in the investigations regarding Cushing's mechanism, the link of hypoperfusion of the brainstem with elevated sympathetic nerve activity has been established mostly through animal or in vitro experiments[88,89]. Waki et al.[88] showed that induced hypoxia of the rat medulla leads to a sympathetically mediated increase of BP. While an in vitro preparation of the brainstem and heart, including the surrounding vasculature, of neonatal pre-hypertensive spontaneously hypertensive rats showed that an increase in vascular resistance of the arteries supplying the brainstem caused an increase in sympathetic activation of the heart[89]. In vivo human evidence for the link between medullar hypoperfusion and increased sympathetic outflow is limited due to the difficulty of measuring cerebral blood flow within the human brainstem[90]. In order to expand the investigation of Cushing's mechanism with in vivo human experiments it would therefore not only be of use to have a measure of cerebrovascular resistance in the arteries supplying the medulla, but also to have a measure of cerebrovascular physiology within the brainstem.

The sympathetic nervous system and pathology

In addition to the implication of the sympathetic nervous system in Cushing's mechanism, elevated sympathetic outflow has been related to a plethora of pathologies. For instance, patients suffering from sleep apnoea show increased sympathetic nerve activity, which is hypothesized to be due to the recurrent hypoxia and hypercapnia caused by the apnoea[91]. Obesity is correlated with increased sympathetic outflow because of the accompanying insulin resistance: increased insulin in the blood plasma increases sympathetic nerve activity[92]. The exact mechanisms behind insulin mediated increases in sympathetic outflow are complex and therefore still under investigation. It has been shown that insulin enhances the gain of the baroreflex and that insulin mediated glucose metabolism in the hypothalamus may be responsible for elevated sympathetic outflow[93].

Pathologies in which sleep apnoea and obesity are important comorbidities are therefore also correlated with increased sympathetic nerve activity, such as poly-cystic ovary syndrome[93]. Having non-invasive imaging tools that are able to assess the role and regulation of the sympathetic nervous system would therefore be of interest for research fields regarding pathologies in which sympathetic outflow is altered.

3.6. Potential applications of the cerebral arterial compliance measurement

Although in this thesis the sympathetic nervous system is used as an example system for the application of the cerebral arterial compliance measurement, this method is applicable to investigation of cerebrovascular health in general. For instance, the compliance measurement can be used to assess the effects of vasoactive drugs on the cerebrovasculature or it can be applied to investigate the effects aging has on stiffening of the cerebral arteries.

One example of the latter would be the application of the arterial compliance measurement to assess the development of small vessel disease (SVD). When arterial compliance decreases, i.e. arteries become stiffer, they lose the ability to smooth the pulsatile blood flow and as a consequence downstream arterioles and capillaries are exposed to pulsatile blood pressure[94]. This increase in blood pressure pulsatility in the distal arterial bed in turn causes deterioration of vessel walls, which in the brain manifests as cerebral small vessel disease[94]. The prevalence of cerebral SVD increases with ageing and has also been linked to cognitive decline in patients with dementia and Alzheimer's Disease[95]. Although the mechanisms underlying development of cerebral SVD are still poorly understood, it is evident that arterial stiffening is highly linked to this pathology[96]. Measuring AC of cerebral and brain feeding arteries may therefore give valuable insight in the development and treatment of cerebral SVD.

To summarise, having non-invasive measurements of human cerebral arterial compliance and medullar (brainstem) function and physiology will facilitate in vivo investigation of sympathetic regulation of the cerebrovasculature. Such tools would not only be useful to clear the controversies surrounding healthy sympathetic regulation, which exists because of contradictive results of animal and ex vivo experiments, but will also enable non-invasive investigation of mechanisms behind (cerebrovascular) pathologies such as *Cushing's mechanism* and poly-cystic ovary syndrome.

Chapter 4

In Vivo Assessment of Human Brainstem Cerebrovascular Physiology

The brainstem is involved in critical physiological processes, including control of cardiovascular and respiratory functions. This study implements a multi inversion time pulsed ASL (MTI PASL) imaging sequence that addresses the challenges of brainstem imaging and aims to measure normal and elevated brainstem perfusion in healthy volunteers. An initial experiment was performed to obtain the kinetic curve of the label in the brainstem and consequently to estimate the label arrival times and tissue perfusion in seven participants. A second experiment estimated the brainstem cerebral vascular reactivity (CVR) to hypercapnia in ten participants. Images were acquired with a gradient echo sequence with two spiral interleaves and short echo time (TE = 2.7 ms). Data were analysed with a two-compartment model, including a tissue and arterial component. In both experiments, perfusion in the brainstem was significantly lower than in cortical grey matter (repeated measures ANOVA, $p < 0.05$), which is as expected since the brainstem consists of grey and white matter, the latter typically showing lower perfusion. The brainstem CVR found here is comparable with previous reports obtained with PET imaging. MTI PASL in combination with a two-compartment signal model can be used to assess brainstem perfusion and cerebral vascular reactivity.

4.1. Introduction

The brainstem plays a key role in many physiological processes central to the survival of the organism. Recent functional MRI studies have investigated the involvement of brainstem nuclei in the control of cardiovascular function[81], respiration[97], pain processing[98] and arousal[99]. Brainstem pathology can be life-threatening or can lead to severe disability. For example, acute brainstem ischemia can lead to the locked-in syndrome[100], while chronic hypoperfusion of the brainstem is implicated in essential hypertension[84].

Positron emission tomography (PET) has been used in clinical studies of brainstem pathologies[101,102] to assess cerebral glucose metabolism and cerebral blood flow (CBF). However, PET requires the administration of a radioactive tracer. MRI-based arterial spin labelling (ASL) offers a non-invasive way to measure tissue perfusion in which the water in arterial blood is labelled as it flows through major brain feeding arteries[15]. Currently there is a limited number of ASL studies that include the brainstem and those studies that do often use ASL techniques optimised for the whole brain[103,104], rather than accounting for the local label kinetics of the brainstem. Furthermore, the presence of magnetic field inhomogeneities causes signal drop-out in regions near boundaries between air and tissue such as between the brainstem and the sphenoid sinus.

Another challenge of brainstem perfusion imaging with ASL is the relatively large contribution of macrovascular signal to the tissue perfusion signal[45]. Note that the aim of ASL is to measure *tissue perfusion*, which means that the signal of interest arises from water that has passed into the brain parenchyma and not from labelled blood still present in the macrovasculature. Signal from voxels in and around major arteries such as the basilar artery, which runs alongside the rostral aspect of the pons, contains a relatively large arterial blood volume fraction (aBV). One approach to minimize the arterial signal is to apply bipolar gradients to reduce signal from moving spins[105–107]. This, however, will extend the echo-time increasing bulk susceptibility artefacts and reducing signal acquired. Furthermore, applying bipolar gradients means that it is impossible to measure aBV, or requires the doubling of the total acquisition time because of the need to acquire images with and without crushing[36]. Recently, modelling approaches to account for macrovascular signal in the ASL kinetic curve have been developed[26,108]. The two-compartment model previously described by Chappell is used here[26].

The transit time of the tagged blood from the labelling location to the capillary bed, here referred to as *tissue arrival time* (Δt_{tiss}), constrains the time of image acquisition (post-labelling delay) required to ensure that labelled spins have entered the microvasculature of the tissue of interest. The Δt_{tiss} varies across the brain[105,109] as does the *arterial arrival time* (Δt_{art}), the time it takes the blood to go from the tag location to the macrovascular bed in the region of interest[105]. Because the kinetic curve of the magnetic label in the brainstem has not been fully investigated, both the Δt_{tiss} and Δt_{art} have yet to be estimated for the brainstem. Their estimation would permit more efficient ASL data acquisition schemes in the future. Knowledge of the Δt_{tiss} in the brainstem, as for any brain region, would enable optimal timing of image acquisition, minimising T_1 decay of the label, especially useful when a restricted set of post-labelling delays or a single post-labelling delay is desired.

The aims of the present study were threefold. First, we improve signal acquisition in the brainstem by using a short echo time spiral acquisition, which resulted from pilot studies investigating image acquisition. Second, we characterise the kinetic curve of the magnetic label in the brainstem. From these data we estimated brainstem perfusion parameters (i.e. CBF, Δt_{tiss}, aBV and Δt_{art}). Tracking of the labelled blood over time was done by acquiring perfusion weighted images at several delay times using multi inversion time pulsed ASL (MTI PASL)[110]. Finally, we aimed to demonstrate the feasibility of MTI PASL to measure perfusion changes by performing a hypercapnic challenge to increase blood flow. This enabled assessment of the cerebral vascular reactivity (CVR) to hypercapnia in the brainstem, a measure of the vascular reserve[111,112].

4.2. Material and Methods

Imaging data were acquired on a 3 T whole body MRI system (GE Excite HDx, Milwaukee, WI) using an eight-channel receive-only head coil. Informed consent was obtained from all volunteers under ethical approval from the Cardiff University School of Psychology Ethics

Committee and all experiments were performed in accordance with the guidelines stated in the Cardiff University Research Framework (version 4.0, 2010).

4.2.1. Improving signal acquisition in the brainstem

Gradient echo spiral-out image acquisition was implemented because spiral trajectories enable the use of short echo times (TE), leading to less dephasing effects and therefore improved signal recovery. We performed a pilot study with 5 healthy volunteers to investigate the use of multiple (2 and 4) spiral interleaves to reduce distortion in the brainstem[7]. Three gradient echo spiral-out series were acquired for each participant: (1) 100 images acquired with one interleaf, (2) 50 images acquired with 2 interleaves, and (3) 25 images acquired with four interleaves. Each series lasted 5 minutes. Results from this pilot study showed that using two interleaves led to an increase in temporal signal to noise ratio (TSNR) in the brainstem, calculated on a voxel wise basis as the mean signal over time divided by the temporal standard deviation of the signal. Pair wise comparison of median TSNR in the brainstem, after a repeated measures ANOVA (F(2,8), $p<0.001$), showed that using two interleaves significantly improved TSNR in the brainstem compared to using a single interleaf ($p<0.001$). Examples of images acquired with 1 and 2 interleaves can also be seen in Figure 4.1. Based on the results of this pilot study the acquisition parameters in the current study were as follows: 2 spiral interleaves, short echo (TE = 2.7 ms), reconstructed matrix 64x64, voxel size = 3x3x7 mm^3, slice gap 1 mm, bandwidth 125 kHz, acquisition window 11 ms.

4.2.2. Assessing the kinetics of the spin label

Image acquisition

Seven young, healthy volunteers (3 female, mean age 29.6 ± 4.9 years) were recruited to the initial study to investigate the kinetics of the label in the brainstem. Gradient-echo spiral imaging, as described above, was used with the following acquisition parameters: 2 interleaves, echo time (TE) = 2.7 ms, matrix = 64x64, voxel size = 3x3x7 mm^3, slice gap = 1 mm, 14 slices (whole brain coverage). Slices were tilted 10°-15° from the axial to the coronal plane to reduce signal loss due to dephasing in the brainstem resulting from through-slice susceptibility-induced gradients[113]. Automated linear shimming with built-in software (GE

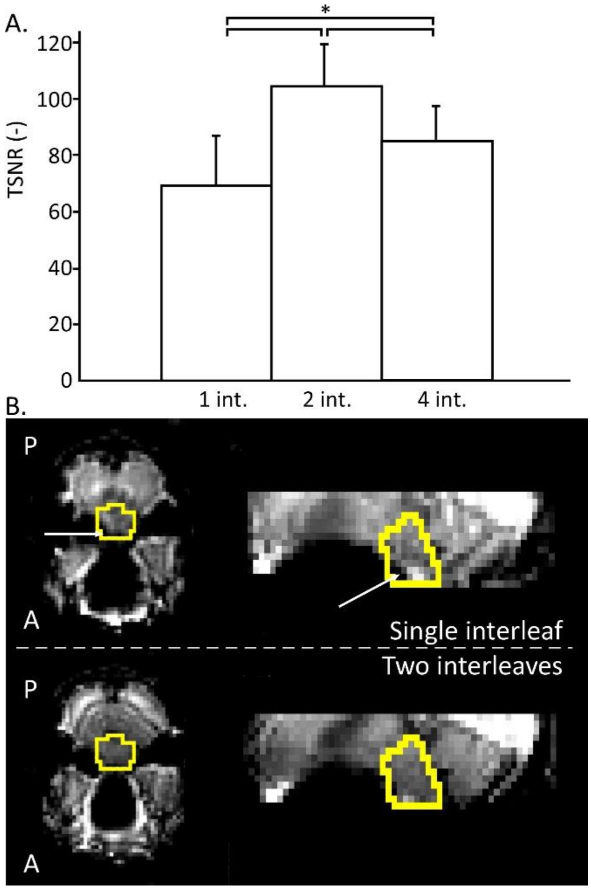

Figure 4.1. **A**. Median TSNR of the brainstem (group averages, N=5) for image acquisitions with 1, 2, and 4 spiral interleaves (int.). * Significantly different (pair wise comparison after RM-ANOVA, $p<0.05$). **B**. Images from the pilot studies comparing acquisitions with a single spiral interleaf (top row) and two spiral interleaves (bottom row). Brainstem outlined in yellow. Note the signal drop-out in the brainstem in the single spiral image (white arrows). The two interleaved spiral image has less distortion, because of a reduced acquisition window[7], shown by a more homogenous signal distribution in the brainstem and the better defined cerebellum. *A = anterior, P = posterior*.s

HDx) was performed. Perfusion weighting was performed with multi inversion time pulsed ASL[26] (13 TIs: 100 ms, 200 ms, 300 ms, 400 ms, 500 ms, 600 ms, 700 ms, 1000 ms, 1300 ms, 1600 ms, 1900 ms, 2200 ms, 2500 ms). A PICORE tagging scheme was used with a QUIPSS II[13] cut off at 700 ms for TI > 700 ms. Label thickness was 200 mm with a 10 mm gap between the distal end of the labelling slab and the most proximal imaging slice. A variable TR (1000 ms – 3400 ms) was used such that imaging time was minimized. Ten control-tag pairs were acquired for each inversion time, resulting in a total acquisition time of 18 mins.

A calibration scan necessary for quantification of the perfusion maps was acquired in the beginning of each session to calculate the equilibrium magnetisation of cerebrospinal fluid ($M_{0,CSF}$). The acquisition parameters for this CSF were the same as for the perfusion weighted scans, except for being acquired with fully relaxed magnetisation and no labelling was applied. An image with minimal contrast was also acquired to map the coil sensitivity profile (same acquisition parameters except for TE = 11 ms, TR = 2 s, and 8 interleaves). Furthermore, a T1-weighted structural image (3D FSPGR) was acquired for registration purposes (TE = 2.9ms, TR = 7.8 ms, flip angle = 20°, voxel size = 1x1x1 mm^3).

Pre-processing

The time series of images was motion corrected using *3dvolreg* within AFNI (http://afni.nimh.nih.gov/afni[114]). Brain extraction was performed on the first image of the raw motion corrected series and the CSF calibration image with BET within the FMRIB Software Library v5.0 (FSL-http://fsl.fmrib.ox.ac.uk[115]). The CSF image was registered to the perfusion series using FLIRT within FSL and a mask of the lateral ventricles was used to calculate $M_{0,CSF}$. This mask was made by first applying a threshold at 95% of the maximum signal intensity to the CSF image and then using AFNI's *3dclust* to find the largest cluster of voxels in a cube covering a large area of the brain, including both ventricles, in this masked image. The equilibrium magnetisation for arterial blood ($M_{0,blood}$) was then calculated according to methods previously described by Wong et al.[13] with CSF as a reference.

Kinetic curve analysis with the two-compartment model

The un-scaled difference images were created for each inversion time by subtracting consecutive tag and control images and averaging the result. Kinetic curves of the label were fitted on a voxel-by-voxel basis using Chappell's two-compartment model[26] to separate tissue signal from arterial signal. In short, this model uses the following equation:

$$\Delta M(t) = \Delta M_{tiss}(t) + \Delta M_{art}(t) \qquad \text{Eq. 4.1}$$

where $\Delta M_{tiss}(t)$ is the signal in a perfusion-weighted difference image directly caused by tissue perfusion and therefore dependent on CBF and Δt_{tiss} and $\Delta M_{art}(t)$ is the signal intensity which is caused by magnetic label still present in the macrovasculature and therefore depends on aBV and Δt_{art}. $\Delta M_{tiss}(t)$ is described by the general kinetic model for pulsed ASL,

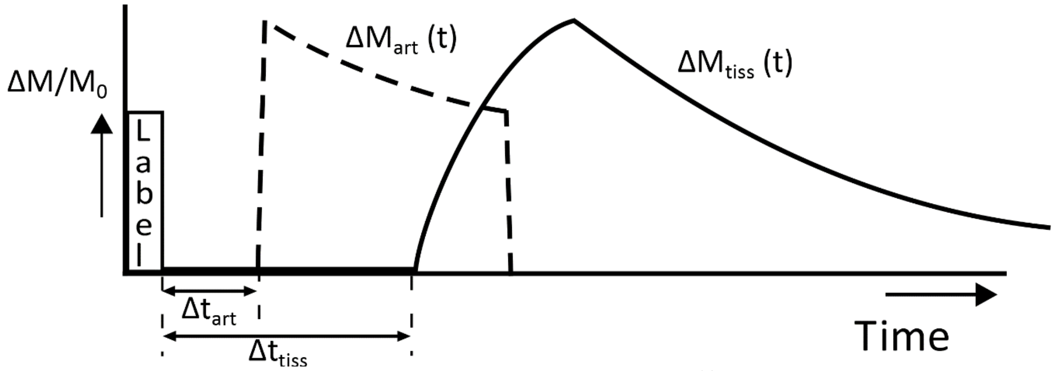

Figure 4.2. Schematic of Chappell's two compartment model[26]. If a voxel has a significant macrovascular compartment an arterial model is fitted to the data (ΔM_{art}), as well as a tissue perfusion model (ΔM_{tiss}). The model also permits estimation of arterial arrival time (Δt_{art}) and tissue arrival time (Δt_{tiss}). Voxels without a significant macrovascular contribution will only have ΔM_{tiss} fitted to the data.

previously published by Buxton et al.[12]. The two-compartment model contains an automatic relevance determination (ARD) algorithm that uses the perfusion weighted data to do a voxel wise assessment of the aBV, which in turn is used to calculate $\Delta M_{art}(t)$. If, as a result of the ARD, aBV is set to 0, Eq. 4.1 is reduced to $\Delta M(t) = \Delta M_{tiss}(t)$. A schematic representation of the model can be seen in Figure 4.2. Chappell's two-compartment model is incorporated as *oxford_asl* in the BASIL toolkit within FSL. The output of *oxford_asl* includes unscaled CBF maps, and maps of the estimated aBV, Δt_{art}, and Δt_{tiss}. In addition, maps containing the variance of each parameter estimate are calculated and can be used to calculate confidence intervals (CI). Here, the un-scaled CBF maps were scaled with $M_{0,blood}$ to convert CBF in ml/100 g/min. Coil sensitivity correction was then performed by dividing the CBF maps by a normalised version of the minimal contrast image. Before normalisation the minimal contrast image was smoothed with an edge-preserving algorithm (SUSAN within FSL, FWHM = 5 mm)[116].

Registration and ROI analysis

Region averages for CBF, Δt_{tiss}, aBV, and Δt_{art} were calculated for the following ROIs: whole brainstem (BS, including medulla, pons and the dorsal part of the midbrain), grey matter (GM, including cortical and subcortical grey matter), cerebellum (CB), and occipital pole (OP). The last two ROIs were added as reference for the brainstem as it was either the nearest large brain structure at a similar rostral-caudal level (CB) or a distal brain structure (OP) for which longer arrival times would be expected[109]. The Harvard Oxford atlas for cortical and subcortical structures, available within FSL, was used to obtain the four ROIs.

In order to minimise interpolation errors in the perfusion data due to registration the region-based analysis was performed in individual subject space. Registration of the four ROIs from MNI152 standard space (Montreal Neurological Institute, Montreal, QC, Canada) to subject space was therefore performed. For this purpose, the brain extracted image of the motion corrected series (see *Pre-processing*) was registered to MNI152 standard space via the T_1 weighted structural image. The resulting transformation matrix was inverted and applied to each of the four ROI masks.

All registrations were performed using FLIRT, within FSL. After region-based analysis, group average CBF and aBV maps were made by using the transformation matrix for registration of subject space maps to MNI152 standard space.

Within the analysis yielding aBV and Δt_{art} only voxels with a considerable arterial contribution (aBV > 0.1%) were considered in the calculations of regional average aBV and Δt_{art} values. If a ROI on average did not have a large enough arterial contribution, the aBV and Δt_{art} resulting from the two-compartment model were undefined and therefore not reported. If there was considerable arterial blood volume, average aBV is calculated by summing the aBV for the voxels with aBV > 0.1 % and dividing this by all the voxels in the ROI (including those voxels without arterial contribution). Average Δt_{art} is calculated by only considering the voxels within a ROI with measurable aBV.

4.2.3. Hypercapnic cerebral vascular reactivity (CVR)

In general the parameters for the hypercapnia experiment were kept the same as for the first experiment, however the following paragraphs describe the differences in methods between the two experiments.

Image acquisition

Ten young, healthy volunteers (3 female, mean age 30.7 ± 5.0 years) were scanned. Within each scan session two perfusion scans were performed: one in normocapnia and one in hypercapnia, with the scan order randomised between subjects. All acquisition parameters for the perfusion scans remained the same for both conditions. The duration of the perfusion acquisition was reduced from the 18 minutes used in the first experiment to approximately 6 minutes to limit the duration of the hypercapnic challenge. Therefore, 6 inversion times (200 ms, 400 ms, 600 ms, 1000 ms, 1600 ms, 2200 ms) and 8 tag-control pairs per inversion time were acquired.

Hypercapnic respiratory challenge

Subjects breathed through a tight-fitting face mask covering nose and mouth (Quadralite, Intersurgical, Wokingham, Berskhire, UK). Gases were delivered from gas cylinders connected to an in-house built and manually operated system of flow meters. Gases were humidified for the comfort of the participant. A gas mixing chamber, as close to the face mask as possible, had three feeding lines coming in for the delivery of medical air, 5% CO_2, and medical oxygen, the latter incorporated as a safety backup but not used during experimentation.

During the *normocapnic* (NC) period participants breathed medical air (20.9% O_2 balance N_2) with a flow rate of 35-40 L/min. Baseline end-tidal CO_2 pressure ($P_{ET}CO_2$) was determined at the start of each scan session, when participants were breathing medical air for approximately 5 minutes. *Hypercapnia* (HC) was manually controlled by mixing medical air with 5% CO_2 until $P_{ET}CO_2$ was raised by 7-8 mmHg above individual participant's baseline. Two minutes of hypercapnia were established to stabilise $P_{ET}CO_2$ prior to image acquisition.

Physiological monitoring

A sampling line connected to the face mask was used to monitor end-tidal CO_2 and O_2 concentrations. A respiratory belt was placed just below the ribs to monitor ventilation and a pulse oximeter finger cuff was used to obtain cardiac traces.

Cerebral vascular reactivity

In addition to the ROI analysis of CBF, Δt_{tiss}, aBV and Δt_{art} as described above, the data analysis of the hypercapnia experiment included assessment of cerebral vascular reactivity to illustrate the feasibility of MTI PASL to measure changes in brainstem perfusion. The CVR is defined here as a change in tissue perfusion between NC and HC due to the change in $P_{ET}CO_2$ and is therefore reported as a percentage change in CBF per mmHg (%/mmHg).

Statistical analysis

Comparison of the physiological parameters between different ROIs was performed with repeated measures ANOVA (RM-ANOVA) in SPSS Statistics for Windows, Version 20.0 (IBM Corp, Armonk, New York, USA) using *ROI* (i.e. BS, CB, OP, and GM) as the independent factor and CBF, aBV, Δt_{art} and Δt_{tiss} as dependent factors. A two-way RM-ANOVA was performed with the data of the hypercapnia experiment in which *physiological state* (i.e. normocapnia or hypercapnia) was added as an independent factor. Follow-up pair-wise comparisons were performed as appropriate using the Bonferroni correction. In some cases, the assumption of sphericity for the data did not hold (i.e. differences between ROI averages do not have equal variances). In those cases the Greenhouse-Geiser correction for sphericity was used and this is reported by using F_{corrGG} instead of F in the Results section. Results are stated as *mean ± standard deviation,* except where explicitly stated as *mean ± standard error of the mean* to illustrate the confidence in the obtained mean values.

4.3. Results

Experiment 1: label kinetics

Repeated measures ANOVA (F(3,18) = 8.6, p<0.01) and the follow-up pair wise comparisons showed that mean brainstem CBF (31.4 ± 10.1 ml/100 g/min, 68% CI 20.0 – 43.1 ml/100 g/min) was significantly lower (p<0.05) than in grey matter (44.7 ± 12.1 ml/100 g/min, 68% CI 33.3 – 56.5 ml/100 g/min). Tissue perfusion in the cerebellum and occipital pole was also significantly different from that in the brainstem (p<0.05, Figure 4.3A). Group average tissue perfusion kinetic curves can be seen in the second row of Figure 4.4. From these curves it

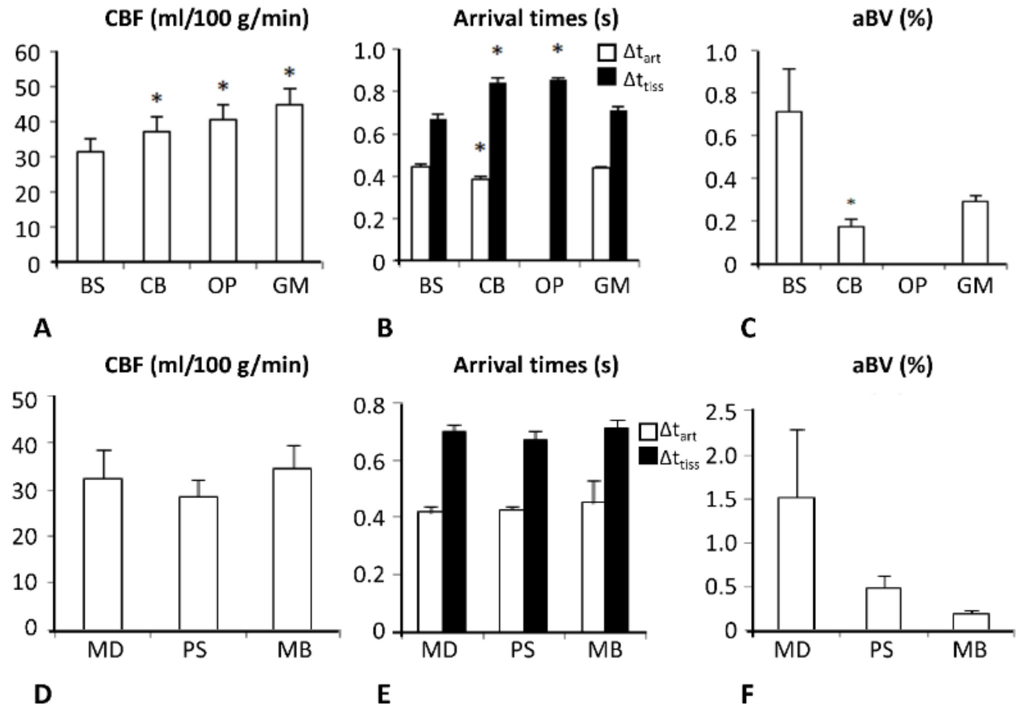

Figure 4.3. **A, D**. Group mean CBF in ml/100 g/min. **B, E**. Arrival times in seconds. Note that no Δt_{art} is reported for OP because this ROI did not have significant aBV (explained in more detail in the Methods section). **C, F.** Group average aBV in %. Error bars in all bar charts reflect the standard error of the mean. BS = brainstem, CB = cerebellum, OP = occipital pole, GM = grey matter, MD = medulla, PS = pons, MB = mid brain. **Significantly different from corresponding brainstem value (Pair wise comparison after RM-ANOVA, $p < 0.05$).*

was calculated that maximum perfusion weighted signal for the brainstem occurs 100 ms earlier than for the grey matter (1.3 s compared to 1.4 s, respectively).

Arterial arrival times for the brainstem, cerebellum and grey matter were 444 ± 31 ms (68 % CI 341 – 551 ms), 384 ± 37 ms (68% CI 268 – 503 ms), and 438± 21 ms (68 % CI 336 – 542 ms), respectively (see B). RM-ANOVA showed a significant difference in Δt_{art} between these ROIs ($F_{corrGG}(1,6) = 7.9$, $p < 0.05$), with the cerebellum having a significantly shorter Δt_{art} than the brainstem ($p<0.05$). No Δt_{art} is reported for the occipital pole, as this ROI had no measurable aBV. Regional tissue arrival times do show significant differences between regions (see Figure 4.3B), with the brainstem having significantly shorter Δt_{tiss} than the cerebellum and occipital pole (pair wise comparisons after RM-ANOVA, $p<0.001$).

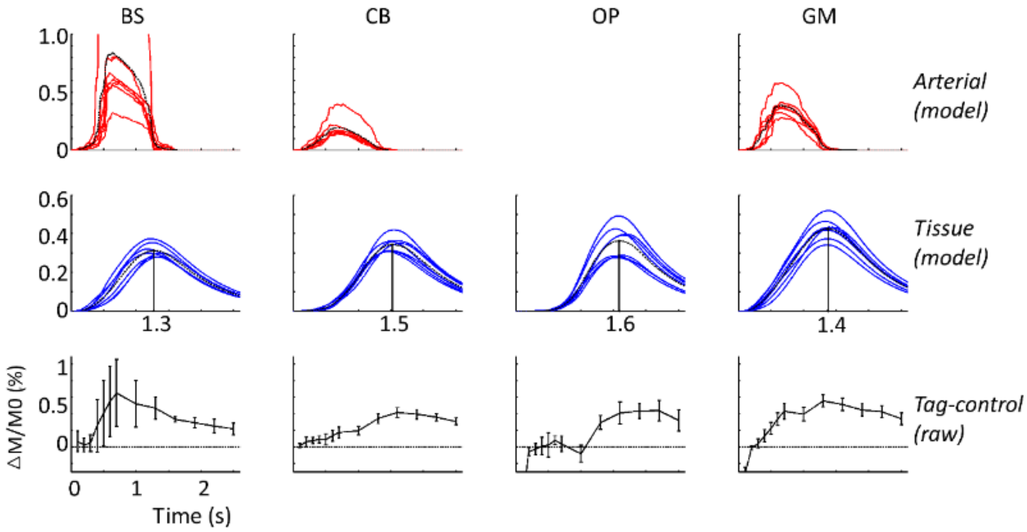

Figure 4.4. Regional average kinetic curves resulting from the model and raw difference signal for (from left to right) the brainstem (BS), cerebellum (CB), occipital pole (OP), and grey matter (GM) in the feasibility experiment (N = 7). Top row: modelled kinetic curve of magnetic label in the macrovasculature. Individual kinetic curves in red, group averaged kinetic curve in dashed black. Middle row: modelled tissue perfusion curve (signal in microvasculature). Individual kinetic curves in blue, group averaged kinetic curves in dashed black. Bottom row: average signal in raw difference images, error bars indicate the standard deviation over 7 subjects.

The modelled kinetic curves in Figure 4.4 show that the brainstem had the largest aBV of all the ROIs analysed, which was also reflected by the high signal intensity at early TIs in the raw tag-control difference (bottom row in Figure 4.4). However, there was no significant difference (pair wise comparison after RM-ANOVA, $p = 0.063$) between brainstem and grey matter aBV (see Figure 4.3C). Furthermore, the occipital pole had no significant macrovascular contribution (average aBV < 0.1%).

Repeated measures ANOVA showed that there were no significant differences in perfusion parameters between the sub regions of the brainstem (medulla, pons and mid-brain in Figure 4.3D, E, and F).

Experiment 2: Hypercapnic CVR

Baseline $P_{ET}CO_2$ was 39.4 ± 2.4 mmHg in NC and 47.3 ± 1.9 in HC, a mean increase of 7.9 ± 1.9 mmHg (*N= 10*). Two-way repeated measures ANOVA showed that the CBF significantly increased during HC (F(3,27) = 12.0, $p<0.001$). Average grey matter perfusion (cortical and subcortical) was significantly higher than in the brainstem, both in NC and HC (pair wise comparisons after RM-ANOVA, $p<0.05$). Brainstem CBF increased from 43.8 ± 11.5 ml/100 g/min in NC to 55.7 ± 15.9 ml/100 g/min in HC, while grey matter perfusion increased from 52.6 ± 10.4 ml/100 g/min in NC to 67.3 ± 12.8 ml/100 g/min in HC. Perfusion values for the remainder of ROIs can be seen in Figure 4.5A. Group mean perfusion maps resulting from the hypercapnia experiment are shown in Figure 4.6. The cerebral vascular responses for the brainstem (3.8 ± 5.7 %/mmHg, SEM = 1.8 %/mmHg) and grey matter (3.5 ± 1.9 %/mmHg, SEM = 0.6 %/mmHg) were not significantly different (RM-ANOVA, $F_{corrGG}(2,15) = 1.95$, p = 0.180).

As expected, aBV showed significant increases during hypercapnia throughout the whole brain (RM-ANOVA, $F_{corrGG}(1,9) = 14$, $p<0.01$), as can be seen in Figure 4.5B and also illustrated

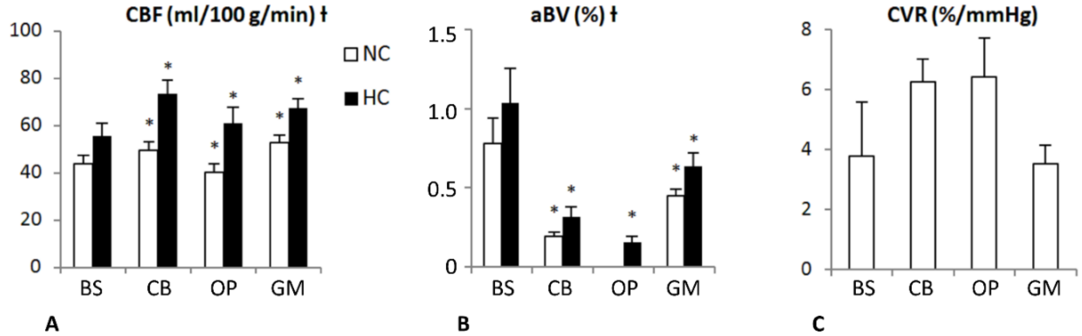

Figure 4.5. **A**. Average CBF per ROI (ml/100 g/min). All analysed ROIs had significantly higher CBF in HC than in NC (pair wise comparisons after RM-ANOVA, $p<0.05$). Furthermore, all analysed ROIs, had significantly higher CBF in both NC and HC than the brainstem (pair wise comparisons after RM-ANOVA, $p<0.05$). **B**. Average aBV per ROI (%). Note that the brainstem had significantly higher aBV in NC and HC than all other brain regions (pair wise comparisons after RM-ANOVA, $p<0.05$). The OP had no significant aBV in NC (aBV < 0.1%), but did have significant aBV in HC. For all brain regions the increase in aBV during HC was significant (pair wise comparisons after RM-ANOVA, $p<0.05$). **C**. Group average CVR per ROI (%/mmHg). No significant differences were found between the CVR of the brainstem and the remainder of ROIs. Error bars in all three bar charts reflect the standard error of the mean. BS = brainstem, CB = cerebellum, OP = occipital pole, GM = grey matter, NC = normocapnia, HC = hypercapnia. **Significant difference with corresponding value for the brainstem (pair wise comparison after RM-ANOVA, $p<0.05$). ł Significant difference between values in NC and HC, over all ROIs (see text for details).*

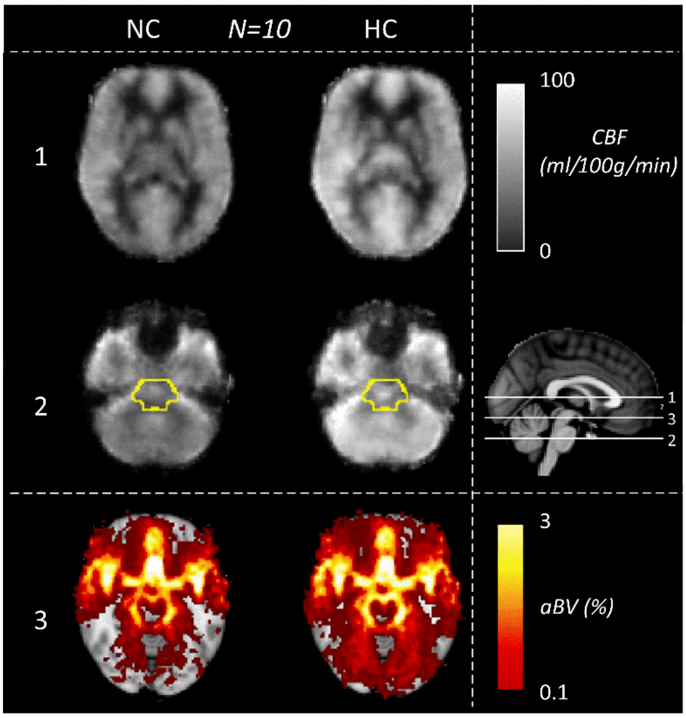

Figure 4.6. Group average perfusion maps (CBF in ml/100 g/min) and arterial blood volume maps (aBV in %) from the hypercapnia experiment (N=10). Maps are in MNI standard space. The sagittal view on the right shows the locations of the axial slices on the left. The superior axial slice (slice 1) goes through the corpus callosum (top row). Slice 2 is an axial slice through the pons. In slice 2 the brainstem is outlined in yellow (mask from the Harvard Oxford subcortical atlas). Slice 3 (bottom row) is an axial slice through the midbrain, at the level of the Circle of Willis.

by group average aBV maps (Figure 4.6). In both NC and HC, the brainstem had the highest aBV from all analysed brain regions (pair wise comparisons after RM-ANOVA, $p<0.01$), as can be seen in Figure 4.5B. The occipital pole had no significant aBV in NC (aBV < 0.1%), but during HC the aBV increased to 0.16 ± 0.1 %. Group mean aBV maps can be seen in Figure 4.6 (bottom row), which shows how the aBV delineated cerebral macrovasculature (e.g. the Circle of Willis).

In the hypercapnia experiment there were minimal differences in arrival times and modelled maxima of label kinetic curve, both between ROIs and physiological states. Mean arrival times, both Δt_{art} and Δt_{tiss}, did show a trend towards a decrease in HC but this decrease was only significant for the tissue arrival time in the GM (pair wise comparison after RM-ANOVA, $p<0.05$).

4.4. Discussion

Kinetic curves of the magnetic label in the brainstem can be obtained by acquiring perfusion images with MTI PASL and short-echo interleaved spiral read-out to yield CBF and arrival time estimates. Separating the macrovascular and microvascular signal using Chappell's two-compartment model was useful in the brainstem because of the high arterial contribution to the perfusion signal. This contribution is illustrated by the relatively large $\Delta M/M_0$ at TI < 700 ms in the BS, as can be seen in the bottom row of Figure 4.4. Furthermore, the hypercapnia experiment showed that increases in brainstem perfusion can be measured with the current perfusion imaging and analysis method, as illustrated by the detected cerebral vascular response in the brainstem. To the best of our knowledge, this study is the first to use arterial spin labelling to not only estimate CBF, but also assess CVR, Δt_{tiss}, Δt_{art}, and aBV in the brainstem of healthy participants.

Brainstem perfusion

Brainstem CBF was significantly lower than (cortical and sub-cortical) grey matter CBF. This may be expected since the BS consists of both grey and white matter in close proximity, the latter widely accepted as having lower perfusion[117]. Previous studies also reported CBF lower in the brainstem than in global GM[103,118]. Furthermore, the brainstem CBF of approximately 40 ml/100 g/min reported in the hypercapnia experiment coincides with the CBF reported by Khalili-Mahani et al.[103], who used pseudo continuous ASL to measure perfusion effects of alcohol and morphine on the whole brain and reported similar baseline brainstem CBF. In addition, Ito et al.[118] performed a hypercapnia experiment with positron emission tomography and found similar brainstem CBF.

Brainstem CVR

The hypercapnia experiment showed the expected increases in CBF throughout the whole brain. In particular, the average grey matter CBF in hypercapnia (67.3 ± 12.8 ml/100 g/min at $P_{ET}CO_2$ of 47 ± 1.9 mmHg) coincides with the value found by Noth et al.[112], who performed a similar hypercapnic experiment with a pulsed ASL perfusion measurement and found an average GM CBF of 71.3 ± 5.9 ml/100 g/min at $P_{ET}CO_2$ of 46.3 ± 0.8 mmHg. The average GM

CVR of 3.5 ± 1.9 %/mmHg is comparable to previously reported values measured with ASL[111,112,119], indicating that brainstem MTI PASL is able to measure CVR in grey matter.

Brainstem CVR values found here are similar to previously reported values measured with different imaging modalities[118,120]. Heistad et al.[120] used radio isotopes to measure vascular responses in anaesthetised dogs and found similar CVR in pons and medulla: both approximately 6 %/mmHg compared to 3.8 ± 5.7 %/mmHg for the whole brainstem here. Ito et al.[118] reported a brainstem CVR of 11.4 ± 14.9 %/mmHg measured with positron emission tomography (PET) in eleven healthy men, which is almost 3 times larger than here. However, this might be explained by the surprisingly low reported increase in arterial CO_2 pressure of only 3 mmHg with a hypercapnic challenge using an inspired gas mixture containing 7% CO_2. In comparison, here an average increase of almost 8 mmHg in $P_{et}CO_2$ is found with a gas mixture containing only 5% CO_2, which is comparable to other literature reports using similar respiratory challenges[111].

Note that the intersubject variability of our measured brainstem CVR is relatively large (3.8 ±5.7 %/mmHg). Contributing to this is the low signal to noise ratio (SNR) of perfusion imaging in the brainstem. One solution for reducing the inter-subject variability of brainstem CVR would be longer data acquisition, i.e. more than 8 tag-control pairs per inversion time, since analysis of our data with just 4 tag-control pairs resulted in an increase in inter-subject variability of approximately 70% (*data not shown*).

Arrival times

Arterial arrival times resulting from the first experiment are higher than previously reported values (>400 ms here vs <400 ms elsewhere[105,107]), which could be explained by the use of different pulsed ASL techniques. Here the arterial compartment of the model contains an almost instantaneously increasing slope (see $\Delta M_{art}(t)$ in Figure 4.2), leading to a rapid inflow of labelled blood being modelled. This effect results in the Δt_{art} depending strongly on the first TI where signal intensity in the unscaled difference images is larger than zero (TI = 400 ms, bottom row Figure 4.4). Reported methods for measuring Δt_{art} differ, for example Chen et al.[105] used flow-sensitive alternating inversion recovery, a pulsed ASL method which does not require a gap between the label and imaging plane and Ho et al.[107] report Δt_{art} within the visual cortex (occipital pole) based on a single slice for which the labelling plane was positioned closer to the occipital pole than in the current study. In both these studies, the label travelled a smaller distance before arriving at the imaging plane, likely explaining the shorter arterial arrival times.

Tissue arrival times as calculated from the kinetic curve experiment compare favourably with previously reported Δt_{tiss} in MTI pulsed ASL experiments[105–107,110,121]. The difference in Δt_{tiss} between proximal and distal brain regions is comparable (250-300 ms in all six studies, including the current experiment) and is also reflected by the maxima in modelled tissue perfusion curves (1.3 s in BS, 1.6 s in OP, Figure 4.4). In literature, Δt_{tiss} ranges from 500 ms to 950 ms[105–107,110,121], which also coincides with the values reported here. On average, studies including additional gradients to crush flow in large arteries have slightly shorter average arrival times for proximal ROIs[105,106], which might be caused by the flow crusher gradients not completely removing macrovascular signal[26].

The brainstem Δt_{art} (444 ± 31 ms) and Δt_{tiss} (670 ± 51 ms) found in the kinetic curve experiment coincide with the data in the un-scaled tag-control images, as can be seen by comparing the modelled arterial and tissue kinetic curves with the tag-control curve in Figure 4.4, giving face validity to the two-compartment model in the brainstem. In combination with the shorter time to maximum perfusion signal in the brainstem compared to grey matter (1.3s in the BS, 1.4s in the GM in Figure 4.4), the arrival time findings imply that for future single inversion time ASL experiments concerning the brainstem it could offer more rapid imaging and a higher signal to noise ratio to use a shorter inversion time than for whole brain ASL imaging.

In the measurement of hypercapnic CVR the use of only six inversion times, with gaps of ≥200 ms between TIs, resulted in lower sensitivity to differences in arrival times. This led to less measured interregional dispersion and limited detection of decreased arrival times in HC, which are expected to be ±100 ms shorter than in NC (based on previous results by Ho et al.[107]).The smaller number of inversion times in the measurement of hypercapnic CVR compared to our assessment of the kinetic curve resulted in lower sensitivity to differences in arrival times and thus less measured inter-regional dispersion and limited detection of changed arrival times in hypercapnia compared to normocapnia. Nevertheless we did observe a significant decrease in Δt_{tiss} (but not in Δt_{art}) during HC in grey matter. This finding suggests that changes in arterial and tissue arrival times due to a functional challenge (i.e. hypercapnia) might (partly) have separate mechanisms. This suggestion has also been made by Ho et al.[107], who found that both Δt_{art} and Δt_{tiss} decreased in the visual cortex during visual stimulation, but while the decrease in Δt_{art} was constant with different stimulation strength the Δt_{tiss} decreased more with stronger stimulation. To thoroughly investigate this ´uncoupling´ of arrival times for hypercapnia we would suggest a MTI PASL experiment with more than 6 inversion times.

Physiological noise

The choice of interleaved spiral acquisition adds certain difficulties to addressing the problem of physiological noise in the brainstem. Respiratory motion and cardiac pulsation are two important sources of physiological noise in brainstem imaging in addition to those mentioned in the introduction[122]. Established methods exists to reduce this physiological noise retrospectively from the imaging data such as RETROICOR[123], which determines cardiac and respiratory phases per image slice and regresses these components from the MR time series. Here the use of RETROICOR is confounded because two consecutive repetition times are used to create a single image.

However, the use of two interleaves in itself decreases the presence of physiological motion because of the fact that one image is a combination of measurements at two time points, each acquired with a k-space trajectory starting at the k-space origin (the same spiral, but shifted 180 degrees). As a result, a dense sampling of the origin of k-space occurs and therefore an interleaved spiral acquisition would be expected to be less sensitive to low-frequency physiological noise than a single spiral acquisition[7].

Signal to noise

It would be desirable to increase image resolution, both in-plane and through-plane, given the small structures that are of biological interest in the brainstem[81,97]. The voxel sizes used here (63 mm^3) do not enable cerebrovascular assessment of individual brainstem nuclei, most of them with diameters < 1 mm[55]. The current data do allow investigation of sub regions in the brainstem (i.e. medulla, pons, and mid-brain). However, no significant differences between these regions were found in perfusion or arrival times so far (Figure 4.3D-F). Not finding significant differences between these regions, even in arrival times, is likely to be partly explained by the fact that the sub regions are small, decreasing the already low signal to noise ratio even further. Increasing SNR of pulsed ASL, for example by imaging at stronger field strengths (e.g. 7 T) or adding denoising methods, could permit perfusion weighted imaging with higher resolution.

Previous studies have shown up to 3-fold increases in SNR of ASL images by using 3D acquisition methods such as 3D GRASE and 3D FSE spiral acquisitions[124]. The advantage of 3D image acquisitions coming from the fast read-out of the imaging volume, instead of a 2D slice-by-slice acquisition, resulting in a higher signal to noise ratio in particular in imaging regions further away from the label. In addition, 3D imaging techniques enable the use of background suppression of the static tissue because the variation in acquisition time of different slices is removed[124]. Brainstem ASL might especially benefit from a 3D FSE spiral acquisition, because of reduced sensitivity to magnetic susceptibility variations compared to 3D GRASE[124]. However, due to software limitations it was not possible to include a 3D FSE spiral acquisition in the current study.

Another possibility for increasing SNR in perfusion imaging would be to use pseudo continuous ASL (pCASL) instead of pulsed ASL, as under ideal circumstances the SNR of pCASL is higher than for PASL due to the extend duration of the labelling[20]. However, a limitation of pCASL is that the labelling efficiency decreases with increasing blood velocity risking the underestimation of increases in CBF[22]. Therefore, particularly in studies where changes in blood flow are to be expected, such as evaluation of CVR using hypercapnia, caution needs to be taken with interpreting the results from pCASL images. However, similar caveats must be considered with PASL. A large spatial bolus width in PASL, such as used here, aims to desensitise PASL methods to blood velocity by ensuring that the trailing edge of the bolus is subject to a saturation pulse at the cut-off time[13]. However, if in this case blood velocities are larger than 29 cm/s (label width 200 mm, cut-off at 700 ms) the current PASL method would also underestimate CBF in hypercapnia. Because average blood velocities in the vertebral and internal carotid arteries in healthy volunteers have been reported to be 22 cm/s and 29 cm/s respectively at a similar $P_{et}CO_2$ level in hypercapnia as used here[125], there is some risk of underestimating CBF and CVR in the current study arising in particular from the component of blood in the carotid arteries.

Applications of brainstem perfusion measurements

As mentioned in the introduction possible clinical application of measures for brainstem vascular function is to aid diagnosis and assessment of treatment of pathologies. Another possible application of the medullar physiology measurement is in the investigation of the role of the sympathetic nervous system in healthy and pathological state, as this brainstem area contains nuclei important in regulation of sympathetic nerve activity. Measurement of brainstem CBF and CVR with pulsed ASL as introduced here has the advantage over PET of being non-invasive and easily applicable in the clinic because there is no need for on-site production of radioactive tracers. A drawback of the current multi inversion time ASL method for clinical application is the relatively long imaging time (e.g. 20 minutes to obtain 13 inversion times). However, the estimation of brainstem arrival times enables design of single inversion time perfusion imaging specifically for the brainstem and although having a single TI prevents explicit arrival time measurements, it will enable CBF and CVR measurements with considerably shorter acquisition time.

In contrast with ASL, Blood oxygenation-level dependent (BOLD) imaging is limited to measuring transient responses to a (functional or physiological) task which are dependent on neural activation and baseline haemodynamics[10]. Without knowledge of this baseline state, comparison of BOLD activation maps between different physiological, e.g. drugs or disease, states is rendered difficult[10,97]. Therefore, in addition to giving a direct measure of brainstem physiology, the current perfusion methods would also complement brainstem BOLD imaging studies.

Brainstem MTI PASL has resulted in robust estimation of the kinetic curve of the magnetic label in the brainstem. The outcome of this study includes estimates of plausible values for brainstem perfusion and arterial and tissue arrival times. Furthermore, MTI PASL for brainstem perfusion imaging was validated by measurement of increased perfusion during hypercapnia, resulting in an estimate of cerebral vascular reactivity in this brain region. These measures of brainstem cerebrovascular function have the potential to be of use in diagnosis and follow-up of brainstem related pathologies and can be used to complement BOLD imaging.

Chapter 5

Investigation of cerebral perfusion in women with poly-cystic ovary syndrome

Application of brainstem optimised arterial spin labelling methods

Poly-cystic ovary syndrome (PCOS) is an endocrine disorder which affects almost one in ten women. Recently it has been hypothesized that the sympathetic nervous system (SNS) is implicated in the pathogenesis of PCOS. One of the key brain regions within the SNS is the medulla (MD), which is part of the brainstem. Our recently optimised method to assess brainstem perfusion (Chapter 4) offers a tool to investigate cerebrovascular changes in the medulla that may be a consequence of PCOS. Therefore this chapter contains an example of applying our brainstem optimised MTI PASL technique in a clinical cohort. Results are presented of measurement of cerebrovascular physiology of the MD in 19 women with PCOS and 19 healthy controls. No differences in hemodynamic parameters within the MD were found between PCOS patients and healthy controls, suggesting that there are no underlying differences in physiology between these groups of participants.

Exploratory voxel wise analyses investigating potential correlations between cerebral perfusion and cardiovascular control are included in this chapter. Results from these analyses suggest that hypoperfusion of the medulla is associated with elevated systemic blood pressure and that there may be cerebral regions other than the brainstem involved in (sympathetically mediated) cardiovascular control. This experiment therefore illustrates that our recently optimised perfusion measurements can also be used to asses cerebral control of cardiovascular function.

5.1. Introduction

Poly-cystic ovary syndrome (PCOS) is an endocrine disorder which affects almost one in ten women[126]. According to the 3rd PCOS workshop consensus of 2012 the three criteria for diagnosis of PCOS are hyperandrogenemia, oligo- or anovulation, and polycystic ovaries on ultrasound examination[126]. However, PCOS is a very heterogeneous condition with many comorbidities; in addition to the aforementioned main criteria in women with PCOS there is a higher prevalence of acne, irregular hair growth (hirsutism and alopecia), insulin resistance, obesity, sleep apnea, and hypertension[93,126]. It is because of these features that recently a theory has been developed that the sympathetic nervous system (SNS) is implicated with the pathogenesis of PCOS[93,127], as from previous research it is known that hyperactivity of the SNS is related to obesity [128], sleep apnea[129] and hypertension[54].

The SNS is commonly known as the "fight or flight" division of the autonomic nervous system and increased sympathetic nerve activity (SNA) will lead to an "excited state" with physiological features such as increased blood pressure (BP), elevated heart rate, deep breathing, and dilated pupils[53,54]. One of the key control centres within the SNS is the medulla (MD), the most distal part of the brainstem (BS), because this subcortical brain region contains nuclei involved with respiratory, cardiac, and vasomotor control[55]. Functional magnetic resonance imaging (fMRI) with blood oxygenation-level dependent (BOLD) contrast in humans has recently given *in vivo* evidence of the medulla's function within the SNS, in particular in control of respiration[97] and BP[130]. Moreover, from animal research it is know that hyperactivity of the neurons originating within the medulla indeed leads to increased SNA[131]. Combining this information with the hypothesis of over activity of the SNS in women with PCOS, here we postulate that there are differences in function and physiology of the medulla between women with PCOS and healthy controls.

In order to assess changes in the medulla's physiology we use multi inversion time pulsed arterial spin labelling (MTI PASL), an imaging method that assesses hemodynamic parameters such as arterial blood volume (aBV) and cerebral blood flow (CBF)[26,109]. The location of the medulla within the brainstem, however, does make PASL imaging of this brain structure challenging because of the presence of magnetic field inhomogeneity caused by the nearby sphenoid sinus, and physiological noise due to cardiac and respiratory motion. In this study we will therefore use MTI PASL methods that address these challenges, which we have recently introduced for assessment of brainstem cerebrovascular physiology[132] (*Chapter 4*).

To the best of our knowledge, this study is the first to investigate CBF in women with PCOS. It is because of this that this chapter not only contains an analysis of cerebrovascular parameters in the medulla, but also exploratory analyses to investigate whether PCOS is related to changes in perfusion in brain regions other than in the brainstem. A recent review by Critchley et al.[133] summarizes neuroimaging experiments that investigate blood oxygenation-level dependent (BOLD) activity correlated with sympathetically mediated processes, such as heart rate variability and skin conductance responses. Critchley's review shows that cortical and subcortical regions involved with cognitive and emotional processes may mediate sympathetic outflow to regulate the 'arousal' state of the human body. For instance, in healthy subjects performing cognitive tasks the anterior and posterior cingulate cortex (ACC and PCC) show BOLD activity correlated with heart rate variability[58] and spontaneous fluctuations in skin conductance responses have shown to be correlated with a network of cerebral regions, including the prefrontal cortex, PCC, and thalamus[134]. Therefore, if PCOS patients indeed have elevated SNA compared to healthy controls, there may also be differences in regional CBF between these groups of women other than in the brainstem.

We also present an analysis of the relationship between cerebrovascular physiology and blood pressure, which enables investigation of *Cushing's mechanism*[84]. This theory suggests that hypoperfusion of the medulla triggers an increase in sympathetic nerve activity and blood pressure to maintain adequate blood flow to the brainstem. This theoretical frame work has arisen from combining over a 100 years of human and animal research into blood pressure control and it aims to assess the mechanisms behind essential hypertension, i.e. hypertension without a clear cause[84,85]. Cushing's mechanism suggests that an increase in cerebrovascular resistance in the brainstem and/or surrounding vasculature is responsible for the decrease in perfusion in the medulla (CBF_{MD}). However, due to difficulty of measuring human CBF_{MD} studies that have directly measured both BP and hypoperfusion of the medulla are restricted to animal experiments[88,89]. Here we therefore use our recently optimised PASL method for brainstem perfusion assessment[90] to measure human medullar cerebrovascular physiology in relation to mean arterial blood pressure. We hypothesize that, because of Cushing's mechanism, CBF and aBV within the medulla are negatively correlated with blood pressure, which would indicate that women with a higher resting blood pressure have higher vascular resistance in the medulla and are less able to compensate hypoperfusion to the brainstem.

Lastly, the combination of the voxel-wise CBF data and the blood pressure measurements in 38 volunteers also enabled an exploratory study to investigate regions in the brain that may be correlated to blood pressure. This is of particular interest because of the accumulating evidence that there are more brain regions involved in cardiovascular control than solely the nuclei within the brainstem[58,81,135]. In addition to Critchley et al.[58] showing that the limbic system might mediate heart rate variability, Nisimaru et al.[135] showed that regions within the cerebellum are mediating cardiovascular output. We therefore hypothesize that an exploratory voxel-wise correlation analysis will elicit regions within the cerebellum and limbic system with significant correlations between CBF and MAP.

Note that the aim of this experiment therefore not only is to show the feasibility of applying our recently optimised brainstem perfusion method to investigate differences in a clinical cohort but also to show that our method can be used to investigate cerebral control of systemic cardiovascular function.

Collaboration

The results presented here are part of an elaborate study run with the aforementioned hypothesis of increased SNA in women with PCOS[93]. This study is currently being run by Andrew Lansdown and Aled Rees from the Cardiff University Centre for Endocrine and Diabetes Sciences and comprises elaborate investigation of endocrine markers (via blood tests), sleep patterns, and neuroimaging variables of sympathetic nerve activity in women with PCOS. As part of my PhD in the Cardiff University Brain Research Imaging Centre (CUBRIC), I helped with the design of the neuroimaging branch of the PCOS study and ran all the MRI scans, which included several structural and functional MRI acquisitions. Here we focus solely on the perfusion scans with the method described in chapter 4[136]. Results are presented with permission of the principal investigators of the PCOS study (A.L. and A.R.).

5.2. Methods

Imaging data were acquired on a 3 T whole body MRI system (GE Excite HDx, Milwaukee, WI) using an eight-channel receive-only head coil. Informed consent was obtained from all volunteers under ethical approval from the local ethics committee.

Forty participants (20 patients and 20 controls) were recruited for the exploratory PCOS study. The controls were age- and BMI-matched with the PCOS patients, which was one of the criteria of the exploratory study to enable control for potential differences in endocrine factors, sleep patterns and imaging markers attributed to age or BMI instead of PCOS. For the work presented in this chapter, it is important to correct for age because of the known decrease in CBF associated with aging[137]. In addition, there have been imaging studies showing that regional CBF values are correlated with BMI[138].

Participants were classified as PCOS patients if they presented with at least two out of three of the following symptoms: ovulatory dysfunction (OD), androgen excess (AE) and poly-cystic ovaries on ultrasound scan (USS). Due to time restrictions there were 2 participants for whom no (complete) perfusion data sets were acquired. Therefore results are presented here for 19 PCOS patients and 19 healthy controls. Relevant information, including testosterone blood levels, is stated in Table 5.1 and Table 5.2.

Image acquisition

Multi inversion time pulsed ASL (PICORE with QUIPSS II cut-off at 700 ms[13]) was acquired with a spiral gradient read-out[132]. Label thickness was 200 mm with a 10 mm gap between the distal end of the labelling slab and the most proximal imaging slice. The image acquisition parameters were: echo time = 2.7 ms, minimised repetition time, single interleave, voxel size 3.5x3.5x7 mm^3, slice gap 1 mm, 14 slices (emphasis on covering the brainstem, for some volunteers excluding the top of the brain). Eight control-tag pairs were acquired for the

Table 5.1. Diagnosis criteria for the 19 PCOS patients included in the CBF experiment.

Criterion	Number of patients
OD & AE	5
AE & USS	3
OD & USS	1
OD, AE, and USS	10

OD = Ovulatory dysfunction, AE = Androgen excess, USS = poly-cystic ovaries on ultrasound

following inversion times (TIs): 150, 300, 450, 600, 1000, 1333, 1667 and 2000 ms. Before the MTI PASL sequences two calibration scans were acquired. First, a so-called CSF scan with the same acquisition parameters as for the PASL scans, except for being acquired with fully relaxed magnetisation and without a labelling pulse. This image was used to acquire the equilibrium magnetisation of cerebrospinal fluid ($M_{0,CSF}$). Second, an image with minimal contrast was acquired to map the coil sensitivity profile with the same acquisition parameters as for the CSF scan, except for TE = 11 ms, TR = 2 s, and 8 spiral interleaves. The total acquisition time of the perfusion scans, including calibration scans, was approximately 10 minutes.

A T_1-weighted structural scan (3D FSPGR, TE = 2.9ms, TR = 7.8 ms, voxel size = 1x1x1 mm^3) was acquired for registration purposes.

Physiological measurements

Cardiac traces were acquired with finger photoplethysmography and monitoring of the respiratory cycle was performed with a pneumatic belt placed just below the rib case. Resting brachial arterial blood pressures were measured noninvasively before the start of the scan session. Mean arterial pressure (MAP) was calculated from the systolic and diastolic blood pressures (MAP = 2/3 * diastolic blood pressure + 1/3 * systolic blood pressure).

Data processing

The PASL time series were corrected for head motion (mcflirt within the FSL toolbox v5.0, http://fsl.fmrib.ox.ac.uk) and physiological noise (RETROICOR[123]). Edge-preserving

Table 5.2 Relevant participant information. No significant differences between groups were found in these parameters. (Unpaired t-tests, p > 0.05)

	PCOS (N = 19)	Controls (N = 19)
Age (years)	30.6 ± 4.9	30.3 ± 5.1
BMI	25.7 ± 5.3	26.5 ± 5.1
MAP (mmHg)	83.9 ± 9.6	84.5 ± 8.9
Testosterone (Blood level in nmol/L)	1.5 ± 0.7	1.2 ± 0.3

smoothing was applied to the minimal contrast image (SUSAN[116], within FSL) and the result was used to correct the PASL time series for the coil sensitivity profile, i.e. the PASL time series was divided by the pre-processed minimal contrast image. Average difference images (ΔM) were obtained for each inversion time after tag-control subtraction of the PASL time series. Chappell's two-compartment model, containing both a macro- and microvascular compartment[26], was then used to fit the kinetic curve of the magnetic label on a voxel-by-voxel basis. Chappell's model is described as follows:

$$\Delta M(t) = \Delta M_{tiss}(t, CBF, \Delta t_{tiss}) + \Delta M_{art}(t, aBV, \Delta t_{art}) \quad \text{Eq. 5.1}$$

Note that in addition to CBF in ml/100 g/min, this model also results in estimates of the arterial blood volume (aBV) in volume percentage of the voxel ($\%_v$), arrival time of the labelled bolus in the macrovasculature (Δt_{art}) in ms and arrival time of the labelled bolus in the microvasculature (Δt_{tiss}) in ms. The reader is referred to the work of Chappell et al.[26] for a full description of the model.

Region based analysis

Masks of whole brain grey matter (GM) were created from the T_1-weighted structural scan with *FAST* (available within FSL). In order to obtain masks of the brainstem linear registrations were performed with *FLIRT* (available within FSL) to register each subject's CSF image to the Montreal Neurological Institute (MNI) standard space, via the T_1-weighted structural scan. The transformation matrices resulting from these registrations were concatenated and inverted to obtain the transformation matrix for the registration from MNI standard space to subject space. The latter transformation matrix was used to register the

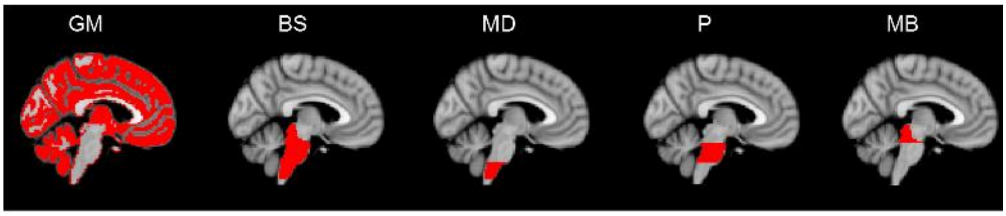

Figure 5.1. The masks used in the region based analysis. Masks (in red) overlaid on the MNI152 standard brain. The masks of the Medulla (MD), Pons (P) and Midbrain (MB) were created from the brainstem mask available within the Harvard-Oxford subcortical atlas.

mask of the brainstem, available within the Harvard-Oxford Subcortical Atlas in FSL, to subject space. The brainstem mask was subdivided into the medulla (MNI standard space: $Z \leq 13$), pons (MNI standard space: $14 \leq Z \leq 24$), and midbrain (MNI standard space: $Z \geq 24$) to calculate CBF, aBV, $\Delta t_{tiss,}$ and Δt_{art} for these regions individually. The masks used in the region-based analysis are shown in Figure 5.1.

Statistics

A mixed effects ANOVA (ME-ANOVA) was performed to compare the ROI averages for the fitted physiological parameters (CBF, aBV, Δt_{tiss}, and Δt_{art}) between the PCOS patients and controls. ROI was used as the within-subject independent factor, with levels Grey Matter, Brainstem, Medulla, Pons, Midbrain, and Subject was used as the between-subject factor, with levels PCOS and Control. Follow-up pairwise comparisons were performed as appropriate using the Bonferroni correction for multiple comparisons.

Because of the known correlations between sympathetic outflow and hypertension[128] and because the medulla is known to contain nuclei involved in sympathetic nerve activity[81,83,131], linear regressions for the hemodynamic parameters within the MD (CBF_{MD}, $\Delta t_{tiss,MD}$, aBV_{MD}, and $\Delta t_{art,MD}$) with MAP were performed.

ME-ANOVA and multiple linear regression were carried out within MATLAB R2012b (Mathworks, Natick, MA, USA).

Exploratory voxel-wise analysis

An exploratory voxel-wise analysis was performed to investigate whether there are any differences in perfusion between PCOS patients and their controls, other than in the brainstem. For this purpose a voxel-wise two sample t-test (3dttest++, within AFNI) was carried out with age, BMI, and MAP as covariates. Z-maps were calculated and significant clusters were determined based on a significance level of $p < 0.01$ ($Z > 2.3$) and $\alpha < 0.01$, allowing for 1 % of the significant clusters to be a false positive (minimum cluster size was 32 voxels).

Within the exploratory voxel-wise analysis of differences in CBF we also included a voxel-wise linear correlation analysis of CBF with MAP with the aim to investigate brain regions that may be mediating or are mediated by blood pressure regulation *(3dttest++, within AFNI)*. Note that these voxel-wise correlations were calculated across PCOS patients and healthy volunteers combined, due to minimal differences in CBF that were found between the groups (see 'Results' section).

Complementary to the exploratory voxel-wise analysis was a voxel-based morphometry (VBM) analysis of the T_1-weighted structural scans to assess whether differences exist in grey matter morphology between PCOS patients and controls. Structural data were analysed with FSL-VBM[139], an optimised VBM protocol[140] carried out with FSL tools[115]. First, structural images were brain-extracted and grey matter-segmented before being registered to the MNI 152 standard space using non-linear registration[141]. The resulting images were averaged and flipped along the x-axis to create a left-right symmetric, study-specific grey matter template. Second, all native grey matter images were non-linearly registered to this study-specific template and "modulated" to correct for local expansion (or contraction) due to the non-linear component of the spatial transformation. The modulated grey matter images were then smoothed with an isotropic Gaussian kernel with a sigma of 3 mm. Finally, a voxel-wise general linear model was applied using permutation-based non-parametric testing, correcting for multiple comparisons across space.

5.3. Results

ROI based analysis

The ROI based analysis showed no significant differences in CBF between PCOS patients and healthy controls (ME-ANOVA, $F(1,36) = 0.3$, $p = 0.60$) , nor were there any significant differences in Δt_{tiss} ($F(1,36) = 0.08$, $p = 0.78$), aBV ($F(1,36) = 0.2$, $p=0.67$), or Δt_{art} ($F(1,36) = 0.008$, $p = 0.93$). Group averages for the resulting physiological parameters per ROI are summarised in Figure 5.2. The ME-ANOVA analyses did show a significant effect of *ROI* on all four hemodynamic parameters ($F(4,36) > 2.5$ and $p < 0.05$ for CBF, Δt_{tiss}, aBV, and Δt_{art}). Some of the main differences of the pairwise comparisons between ROIs were that CBF_{BS} was significantly smaller than CBF_{GM}, and that CBF_{MB} was smallest from all ROIs in the region based analysis ($p < 0.05$). In addition, aBV_{BS} was significantly larger than aBV_{GM} and, in particular, aBV_{MD} was significantly larger than in any of the other ROIs ($p <0.05$).

Linear regression of MAP with CBF_{MD}, $\Delta t_{tiss,MD}$, and aBV_{MD} showed that these hemodynamic parameters tend to decrease with increasing MAP, although none of these correlations was significant (see Figure 5.3). $\Delta t_{art,MD}$ does not seem to be influenced by MAP (see Figure 5.3). However, none of these correlations were significant either ($p > 0.05$). No data is shown for correlations between MAP and the remainder of brain regions (GM, BS, P, MB) because the correlations in these regions were lower than for the MD.

Exploratory voxel-wise analysis

A voxel-wise two-sample t-test with age, BMI, and MAP as covariates resulted in 3 significant clusters of voxels for which CBF was higher in PCOS patients than for healthy controls within the left temporal lobe and the posterior cingulate gyrus (see Figure 5.4 and Table 5.3).

The voxel-wise correlation analysis of CBF with MAP resulted in several regions that were significantly correlated with MAP (Figure 5.5 and Table 5.4). Regions showing negative correlation between CBF and MAP, i.e. decreasing CBF with increasing MAP, include the bilateral temporal pole, ACC and perigenual anterior cingulate cortex (periACC). Regions with positive correlations between MAP and CBF include the bilateral dentate nuclei in the cerebellum.

The VBM analysis did not show any significant differences in grey matter morphology between PCOS patients and healthy controls.

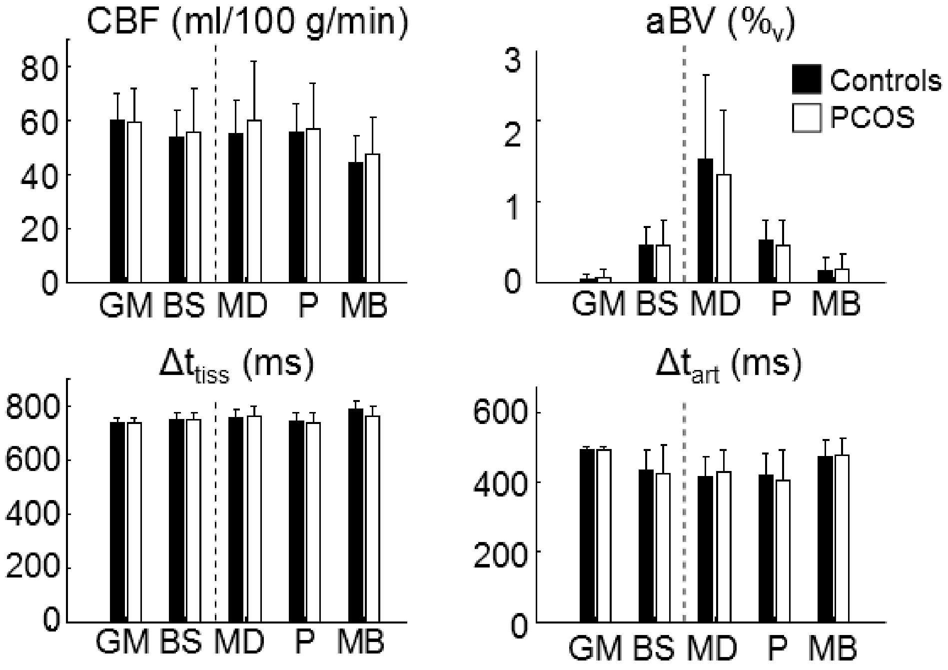

Figure 5.2. Average hemodynamic parameters for healthy controls (solid bars) and PCOS patients (open bars). Each bar graph contains the results of the sub regional masks within the brainstem on the right of the dotted lines. Mixed-effect ANOVAs did not show any significant differences between healthy controls and PCOS patients. Error bars indicate standard deviations. CBF = cerebral blood flow, aBV = arterial blood volume, Δt_{tiss} = tissue arrival time, Δt_{art} = arterial arrival time, GM = grey matter, BS = brainstem, MD = medulla, P = pons, MB = midbrain.

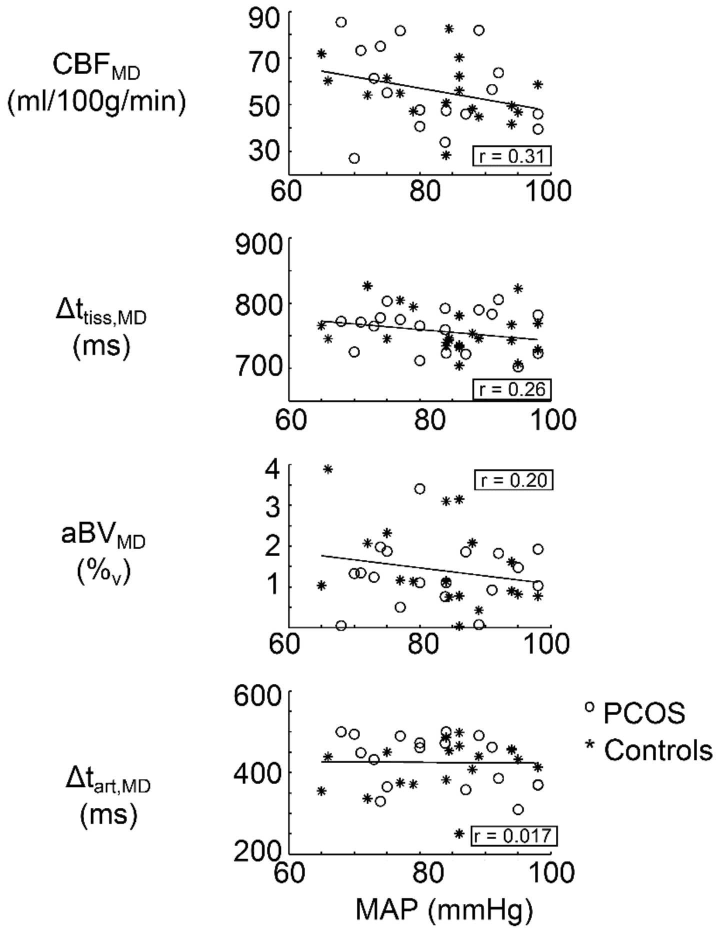

Figure 5.3. Hemodynamic parameters within the medulla correlate with MAP. Correlations are calculated for all participants together, as no significant differences exist between PCOS and controls. It can be seen that CBF$_{MD}$, Δt$_{tiss,MD}$, and aBV$_{MD}$ are decreasing with MAP, while there Δt$_{art,MD}$ seems to be independent of MAP. However, none of these correlation reach significance ($p = 0.07$, $p = 0.13$, $p = 0.25$, $p = 0.92$, respectively). *CBF = cerebral blood flow,* Δt$_{tiss}$ *= tissue arrival time, aBV = arterial blood volume,* Δt$_{art}$ *= arterial arrival time, MAP = mean arterial pressure.*

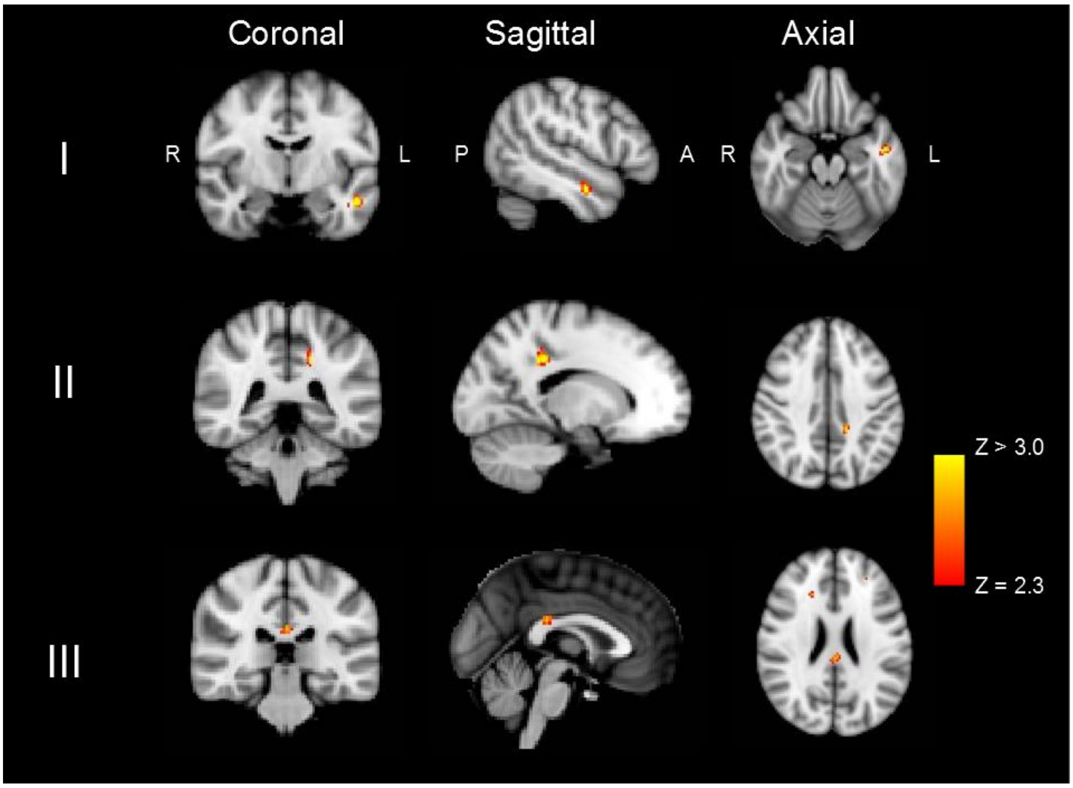

Figure 5.4. Three clusters of voxels that showed significantly (Z > 2.3, α = 0.01) elevated CBF in PCOS patients compared to healthy controls. Results from a voxel-wise two sample t-test with age, BMI, and MAP included as covariates (19 PCOS patients, 19 healthy controls). Clusters are located in the left middle temporal gyrus (I), Cingulate gyrus (Brodmann area 31) (II), and posterior cingulate gyrus (III).

Table 5.3. Clusters of significant differences within CBF between PCOS patients and healthy controls. Results from a voxel-wise two sample t-test with age, BMI, and MAP as covariates.

Brain region (Harvard-Oxford atlases)	Centre of mass MNI standard space x, y, z coordinates (mm)	Max Z-stat	CBF PCOS (ml/100g/min)	CBF Controls (ml/100g/min)
Left middle temporal gyrus	-50, -8, -20	3.2	70.6 ± 17.0	57.0 ± 9.0
Posterior cingulate gyrus (Brodmann area 31)	-16, -40, 38	3.1	22.9 ± 8.4	14.6 ± 5.5
Posterior cingulate gyrus	0, -30, 24	2.9	54.2 ± 15.6	39.4 ± 13.8

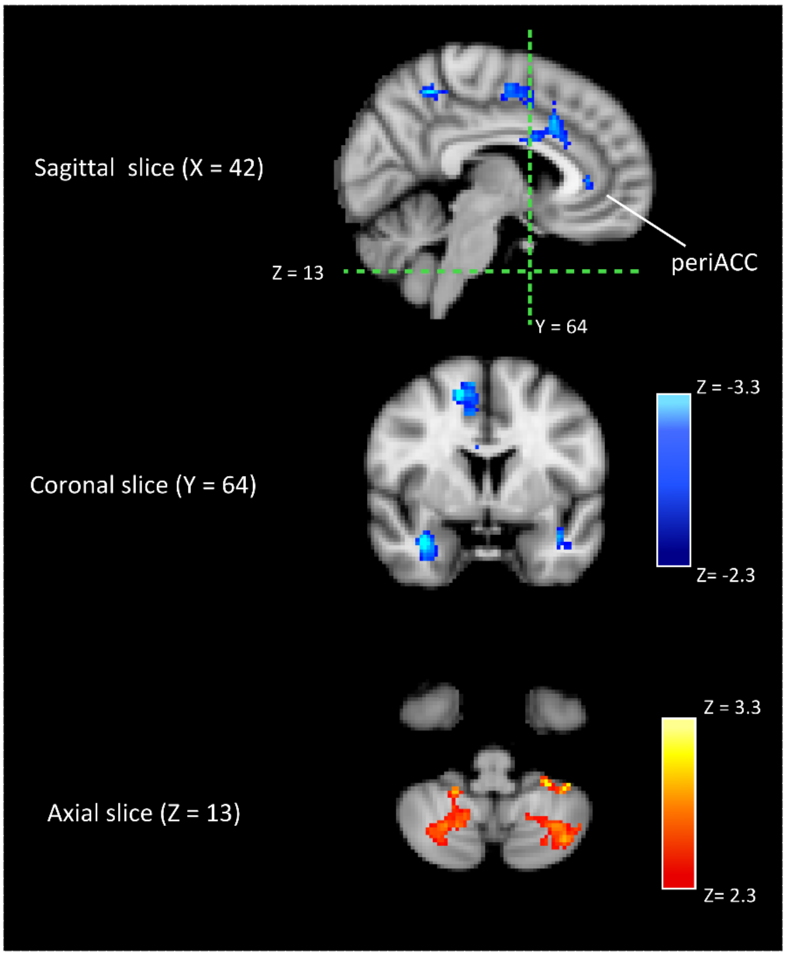

Figure 5.5. Clusters of voxels that show a significant correlation between CBF and MAP, Z-statistics are shown. Clusters were deemed significant if they contained more than 31 voxels (Z > 2.3 and α > 0.01, see 'Methods'). The Z-maps were calculated based on the pooled data of all 38 subjects, because there were minimal differences in CBF in regional and voxel-wise analyses. Note that negative correlations between CBF and MAP are found with regions in the ACC and periACC in the right hemisphere (top image, X = 42) and in the bilateral temporal lobes (middle image, Y = 64). Positive correlations are found in clusters in the bilateral cerebellum (bottom image, Z = 13). The coronal and axial slices shown here are highlighted in the sagittal slice by green dashed lines. Coordinates are in MNI standard space.

Table 5.4. Location of clusters of voxels that show significant negative or positive correlation of CBF with MAP. (BA = Brodmann area).

Brain region (Harvard-Oxford atlases / Duvernoy's atlas)	Centre of mass MNI standard space x, y, z coordinates (mm)	Negative/positive correlation
Supplementary motor cortex	10, -4, 50	-
ACC (BA 24 & 32)	6, 18, 34	-
Right temporal lobe:		
amygdala/BA 28	32, 4, -28	-
Superior temporal gyrus (BA 38)	50, 16, -24	-
Left temporal lobe (planum polare)	-42, 2, -26	-
Right superior cerebellum (superior semilunar lobule/uvula)	18, -88, -26	-
periACC (BA 9/caudate nucleus)	6, 36, 2	-
Right cerebellum posterior lobe (dentate nucleus)	24, -60, -46	+
Left cerebellum:		
posterior lobe (dentate nucleus)	-36, -66, -46	+
middle cerebral peduncle (brachium pontis)	-34, -42, 44	+

5.4. Discussion

The current study investigates hemodynamics of the brainstem, and the medulla in particular, within a cohort of PCOS patients and healthy controls. To the best of our knowledge this is the first study that investigates resting brain perfusion in PCOS patients. The main hypothesis behind the overall PCOS study is that elevated sympathetic outflow is related to PCOS and the medulla is an important control centre for sympathetic nerve activity[93]. However, few differences in cerebral hemodynamics were found between PCOS patients and healthy volunteers. Interestingly, the current experiment enabled exploratory analyses of cerebrovascular physiology in relation to Cushing's mechanism[84] and blood pressure regulation.

PCOS related changes in cerebral hemodynamics?

The region-based analysis showed that none of the four hemodynamic parameters (CBF, Δt_{tiss}, aBV, Δt_{art}) was significantly different between PCOS patients and healthy controls in GM or BS, as illustrated in Figure 5.2. Moreover, results here for both patients and healthy volunteers are in good agreement with what is expected from literature and anatomy within healthy volunteers, with average CBF_{GM} being approximately 60 ml/100 g/min for both patients and controls and finding that the BS had significantly lower perfusion and higher aBV than the GM[45,132]. The lower perfusion in the BS is explained by the presence of both grey and white matter, and the higher aBV can be explained by the fact that the basilar artery runs alongside the anterior part of the pons.

The fact that in the current baseline perfusion analysis no differences were found in regional hemodynamic parameters between PCOS patients and healthy controls might be as expected. There are currently no known links with either poly-cystic ovaries or ovulatory dysfunction and CBF and, although there are regions within the brain that show activity correlated with androgen levels[142], these do not include the brainstem or the whole brain grey matter. Furthermore, currently there is little evidence in the literature that there are baseline differences in regional perfusion due to PCOS per se, even in studies that have investigated brain function in this clinical cohort with BOLD functional MRI[143–145]. None of these studies report differences in baseline brain function related to PCOS, they solely report relative differences in BOLD responses to visual cues. Moreover, these neuroimaging studies focus on a single aspect of PCOS, namely insulin sensitivity within patients[143–145]. For instance, the research conducted by Van Vugt et al. aims at mapping the brain regions that are correlated with insulin sensitivity and use a cohort of PCOS patients because of the heterogeneity of insulin sensitivity amongst PCOS patients. On top of that, Van Vugt et al. do not include healthy controls in their experiments[144,145]. Comparing the results from our voxel-wise analysis (Table 5.3) with Van Vugt's results does suggest that the differences in CBF between PCOS and healthy controls are not related to differences in insulin sensitivities within these cohorts. The main brain regions showing insulin sensitivity related activation reported by Van Vugt et al. do not include the posterior cingulate cortex (PCC), or the left middle temporal cortex[144,145].

Marsh et al.[143] did include healthy controls in their study, that aims to explain why mood disorders are more prevalent among PCOS patients, which potentially enables comparison with the results from our voxel-wise analysis. Marsh et al. use BOLD imaging to investigate differences in emotional processing in the brain related to insulin sensitivity and for this purpose compare insulin resistant PCOS patients with non-insulin resistant healthy controls[143]. They found different levels of activation in the left prefrontal and bilateral anterior cingulate cortex (ACC), areas that are involved in integration of cognitive and emotional processing[143]. However, Marsh et al. do not report differences in the regions we have found to have different baseline CBF (Figure 5.3 and Table 5.3).

Can we then explain why our voxel-wise comparison of baseline CBF resulted in differences between PCOS patients and healthy volunteers within the left middle temporal cortex and the PCC? The latter has been previously linked with autonomic processes via its role in cognitive and emotional processes[58,134]. For instance, Critchley et al.[58] found that there is BOLD activity within the PCC correlated with heart rate variability during cognitive and motor tasks independent from the stimulus, suggesting that this activity was not related to the tasks. Patterson et al.[134] measured BOLD activity in the PCC correlated with skin conductance responses, another indirect measure of sympathetic outflow. Based on these results, elevated CBF_{PCC} may suggest that PCOS patients have elevated sympathetic outflow compared to healthy controls. However, no significant differences are found in CBF_{MD} nor in any other regions implicated with autonomic control by either Critchley et al.[58] or Patterson et al.[134] during cognitive/emotional processing. Whether or not there is a difference in SNA between PCOS patients and healthy controls can only be assessed by direct measurement of sympathetic outflow.

Another possibility is that voxel-wise differences in CBF are related to the androgen excess in the PCOS patients, as 18 out of 19 included patients were diagnosed with this criterion (see Table 5.1). PCOS patients with AE have elevated levels of free testosterone, which potentially leads to an increase of cerebral metabolism in regions that have androgen sensitive receptors, such as the amygdala, ACC or PCC[142]. In addition, in a study with women suffering from anorexia nervosa administration of testosterone lead to increased CBF within several brain areas, including the PCC[146]. However, blood tests included in this experiment did not result in a significant difference in free testosterone levels between the PCOS patients and healthy volunteers (Table 5.2).

Interestingly, a study investigating grey matter volume changes during puberty found that increased testosterone levels are correlated to higher grey matter volumes within the temporal lobes[147]. If higher levels of testosterone mean that there is a higher grey-to-white matter ratio within the temporal lobe, this could explain the higher perfusion in PCOS patients found here as grey matter has a 2-3 times higher perfusion rate than white matter. However, the current VBM analysis resulted in no significant differences between PCOS and healthy grey matter volume, which rules out a testosterone mediated increase in grey matter volume being responsible for the differences in CBF.

The small number of voxels found with significant differences in CBF between PCOS patients and healthy volunteers likely suggest that there are no gross underlying differences in physiology between the current groups that would cause differences in perfusion. The differences found may have occurred by chance. Another possibility is that the differences are caused by miss-registration of the low resolution CBF maps to standard space, resulting in significant differences at border regions (i.e. between high-perfused grey and low-perfused white matter). Irrespective of the cause of the significant differences in CBF between PCOS patients and healthy controls, for the remainder of the discussion these are not considered to be of significance and CBF data is pooled together over all 38 participants.

Blood pressure and medulla perfusion

One interesting aspect of this experiment is that, in combination with the measurement of MAP, MTI PASL optimized for lower brain regions measured in a large cohort of participants does enable investigation of medullar cerebrovascular physiology in relation to resting blood pressure. As illustrated by Figure 5.4, data from both PCOS patients and healthy controls are grouped together for the linear regression analysis between ROI based CBF_{MD} and MAP because there were no significant differences in the cerebrovascular parameters within the medulla. Although none of these correlations are significant, trends are observed that may shed some light on medullar cerebrovascular physiology in relation to resting blood pressure, as is outlined in the following paragraphs.

The correlation between CBF_{MD} and MAP (Figure 5.4), although not significant, suggests that Cushing's mechanism is correct and that women with lower perfusion of the medulla have higher MAP. Cushing's mechanism is also called the selfish brain hypothesis, because the decrease in CBF_{MD} is said to cause an increase in blood pressure to maintain adequate blood flow to the brainstem. Within this theoretical frame work the exact mechanisms linking detection of hypoperfusion and elevating MAP are not yet known. However, from previous experiments it is known that it is an increase in sympathetic outflow from the medulla that can cause the increase in BP because this brainstem region contains important nuclei involved in blood pressure control[83,148]. One example of BP regulation being mediated by the medulla is illustrated by the baroreflex (schematic in Figure 5.6)[148]: a decrease in MAP is detected by baroreceptors in the external carotid arteries signalling a decrease in neuronal firing of the nucleus of the solitary tract (NTS), which in turn leads to a decrease in activity of the caudal ventrolateral medulla (CVLM). The CVLM inhibits the RVLM and a decrease in CVLM activity therefore leads to an increase in RVLM outflow. In the selfish brain hypothesis it is suggested that there may be another, not yet discovered, BP sensor within the brain that triggers the baroreflex to elevate MAP[85]. Although the current dataset does support Cushing's mechanism, more research into the origin of the negative correlation between MAP and CBF_{MD} is necessary to investigate the underlying mechanisms.

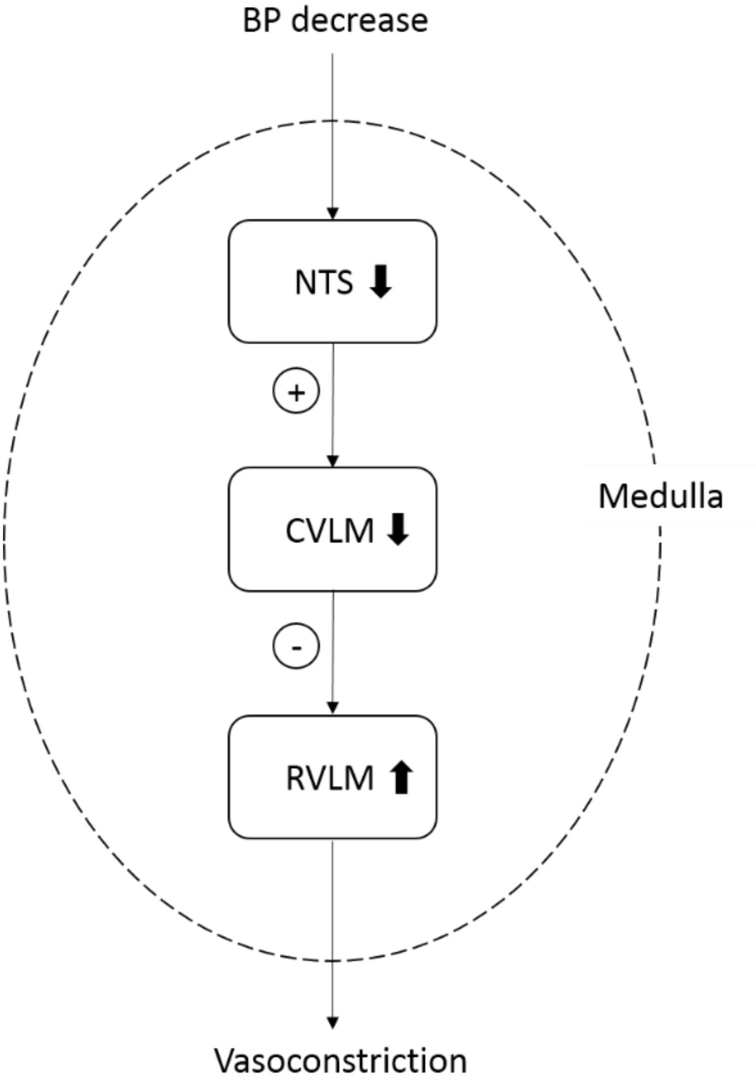

Figure 5.6. Schematic of medullar nuclei involved in the baroreceptor reflex, based on animal research [149] and in-vivo functional MRI within humans [83]. A decrease in blood pressure causes the NTS to decrease excitatory stimulation of the CVLM, which in turn leads to a decrease in inhibition of the RVLM. This means that sympathetic outflow by the RLVM is increased, which leads to peripheral vasoconstriction. *NTS = nucleus of the solitary tract, CVLM = caudal ventrolateral medulla, RVLM = rostral ventrolateral medulla, + excitatory stimulation, - inhibitory stimulation.*

Note that, if Cushing's mechanism is indeed present, this means that women with higher resting MAP should have higher sympathetic nerve activity, as the increase in MAP is a result from the sympathetically mediated vasoconstriction regulated by the RVLM[83,149,150]. However, it is known that in pre-menopausal women there is no correlation between MAP at rest and sympathetic outflow, as measured by muscle sympathetic nerve activity (MSNA)[150]. For instance, in women with high MSNA resting MAP is not necessarily high (and vice versa)[151]. Recent work has shown that pre-menopausal women show potentiated β-adrenergic receptor mediated vasodilation that is able to counteract increased sympathetic outflow to maintain MAP by offsetting α-adrenergic receptor mediated vasoconstriction[152]. This means that it is possible that women with low MAP and low CBF_{MD} still show elevated MSNA, in accordance with Cushing's mechanism, but that this increases sympathetic outflow does not lead to increased MAP. It is because of this lack of correlation between MAP and MSNA that future investigation into the role of the medulla within Cushing's mechanism should at minimum include a direct measurement of sympathetic outflow and should treat pre-menopausal women separate from post-menopausal women and men. When pre-menopausal women are included, such an experiment should control for β-adrenergic receptor mediated vasodilation, e.g. by including a β-adrenergic receptor antagonist[152].

A network for blood pressure regulation?

The voxel-wise whole brain correlation analysis revealed a network of brain regions showing negative and positive correlations between MAP and CBF. The negative correlation between CBF and MAP in the ACC and periACC replicates the results from Sander et al.[81], who found that the ACC and periACC show a decrease in BOLD activity during post exercise ischemia (PEI) in men and women. Despite showing elevated sympathetic outflow during PEI, Sander et al. hypothesized that the decreases in BOLD activity might have been caused by the pain participants felt during the uncomfortable PEI, because previous experiments highlighted the involvement of these areas in pain processing[81]. However, in our experiment participants were not experiencing any discomfort during the CBF scan, suggesting that the decrease in BOLD activity within the ACC and periACC during PEI might indeed be related to the increase in BP that occurred during PEI in Sander's experiment. Moreover, Critchley et al.[58] found that the dorsal ACC shows BOLD activity related to sympathetically driven low-frequency heart rate variability in healthy volunteers, strengthening the hypothesis that the changes in CBF with MAP are related to sympathetic outflow.

Nowadays the view that the cerebellum is only involved in motor control has long been outdated as there are regions within the cerebellum that are involved in cognitive, emotional and autonomic processes[55,135,153]. For instance, in anaesthetised rabbits and cats stimulating the superior semilunar lobule (uvula) resulted in a decrease in systemic blood pressure[135]. In addition, anatomical research has shown that there are projections connecting the cerebellum to several brain regions implicated to mediate sympathetically mediated processes, including the superior temporal gyrus and the ACC[60]. Interestingly, our results from the voxel-wise correlation of CBF and MAP include brain regions corresponding to the literature about the cerebellar function within the SNS (Table 5.4).

However, it must be noted that the design of the current experiment was aimed at investigating the differences in perfusion between PCOS patients and healthy controls and therefore sub-optimal for investigation of sympathetically mediated blood pressure regulation. This is for instance illustrated by not finding clusters within the brainstem in which CBF and MAP were significantly correlated (correlations in this region did not pass corrections for cluster size, data not shown). The current results do suggest that our recently optimised perfusion measurement can be used as a tool to investigate cerebral physiological aspects of blood pressure regulation, in an experiment optimised to investigate this physiological process. Such an experiment should as a minimum include a homogeneous cohort of volunteers and would benefit from a within-subject design, e.g. incorporate a BP modulating task, to maximise statistical power.

Methodological considerations

In the current experiment there are two points at which we have diverted from our brainstem optimized MTI PASL protocol as presented previously[132]. First, we used only 8 inversion times here instead of the 13 inversion times used to fully explore the kinetic curve of the label in the brainstem. The main reason for this is that we had to decrease the total acquisition time of the perfusion scans as the full scan protocol of the PCOS study lasted approximately 1.5 hours. Eight TIs were chosen to ensure temporal spacing of inversion times of less than 200 ms at the early TIs, which leads to increased sensitivity to pick up differences in arrival times compared to the 6 TIs used during the hypercapnia experiment as presented previously (although these were not found between PCOS patients and healthy volunteers)[132].

Secondly, here we used a gradient echo read-out with a single spiral interleave, instead of using two spiral interleaves as suggested by our previous experiment[132]. The main reason being that when using two interleaves to create a signal image the acquisition time for this image is 2*TR and that although temporal SNR and image quality in the area around the brainstem was improved[132], little improvement was seen for the rest of the brain. In this experiment, we then chose to use a single interleave as this would enable more images to be acquired within a shorter period of time, which in itself is beneficial for increasing the signal to noise ratio of the CBF measurement.

To summarise, the current study is the first that has investigated CBF in PCOS patients, which proved to be an optimal application of MTI PASL methods that we have previously presented[132]. Few differences in regional cerebrovascular parameters between PCOS patients and healthy women in the brainstem, nor in the medulla, were found. These results suggest that there are no differences in underlying physiology, including MSNA levels, between the current cohort of PCOS patients and healthy volunteers. Future work should include a direct measure of sympathetic outflow to investigate the hypothesis that PCOS goes hand in hand with elevated SNA. However, the inclusion of BP measurements in combination with little difference in CBF between the PCOS patients and healthy controls did enable exploratory voxel-wise analyses investigating potential correlations between cerebral perfusion and cardiovascular control. Our results suggest negative correlations between MAP and CBF_{MD} and between MAP and aBV_{MD}, which is as expected based on the theoretical frame work of Cushing's mechanism[84]. Moreover, brain regions including areas within the cerebellum and limbic cortex have been found to show perfusion that correlates with BP, coinciding with literature on brain regions other than the medulla that are implicated in sympathetically mediated cardiovascular control. The current experiment has shown that our recently optimised PASL method can be applied to investigate cerebrovascular physiology within a clinical cohort and has laid the basis to use perfusion measurements for investigating cerebral control of cardiovascular function.

Chapter 6

Non-invasive assessment of arterial compliance of human cerebral arteries

A non-invasive method of assessing cerebral arterial compliance (AC) is introduced in which arterial spin labelling (ASL) is used to measure changes in arterial blood volume occurring within the cardiac cycle. Short inversion time pulsed ASL was performed on healthy volunteers with inversion times ranging from 250ms to 850ms. A model of the arterial input function was used to obtain the arterial blood volume (aBV). Results indicate that aBV depends on the cardiac phase of the arteries in the imaging volume. Arterial compliance, calculated from aBV and brachial blood pressures measured in systole and diastole, was assessed in the flow territories of the basal cerebral arteries originating from the Circle of Willis: right and left middle cerebral arteries (RMCA and LMCA), right and left posterior cerebral arteries (RPCA and LPCA), and the anterior cerebral artery (ACA). Group average AC values calculated for the RMCA, LMCA, ACA, RPCA, and LPCA were 0.56 ± 0.2 %/mmHg, 0.50 ± 0.3 %/mmHg, 0.4 ± 0.2 %/mmHg, 1.1 ± 0.5 %/mmHg, 1.1 ± 0.3 %/mmHg, respectively. The current experiment has shown the feasibility of measuring AC of cerebral arteries with short inversion time PASL.

6.1. Introduction

The classical definition of arterial compliance (AC) by Spencer and Denison is a change in arterial blood volume (aBV) due to a given change in arterial blood pressure[154]. AC ensures that arteries are able to accommodate the pulsatile blood flow originating from the heart and average out these pulsations to have continuous blood flow in the capillary bed of human tissue[155]. When AC decreases, that is arteries become stiffer, they lose the ability to smooth the pulsatile blood flow and as a consequence downstream arterioles and capillaries are exposed to high blood pressures[94]. This increase in blood pressure in the distal arterial bed in turn causes deterioration of vessel walls, which in the brain manifests as cerebral small vessel disease (SVD)[94]. The prevalence of SVD increases with aging and has also been linked to cognitive decline in patients with dementia and Alzheimer's Disease[156]. Moreover, patients with diabetes mellitus[94] and hypertension[157] also have an increased risk at developing SVD. Although the mechanisms underlying development of cerebral SVD are still poorly understood, it is evident that arterial stiffening is highly linked to this pathology[96]. Measuring local AC in the brain may therefore give valuable insight in the development and treatment of cerebral SVD.

Compliance of cerebral arteries has long been ignored in cerebrovascular research because of the difficulty of obtaining in vivo measurements of mechanical wall properties and the fact that ex vivo deformation testing has shown that intracerebral arteries are relatively stiff compared to extracranial arteries[158,159]. However, from a physiological standpoint it is important that cerebral arteries are also compliant and act as a flow-buffer to enable steady flow through the cerebral capillary bed and to protect this distal microvasculature from blood pressure fluctuations[160]. This is likely the reason for the fact that recent advances in modelling cerebral pressure-flow relationships have shown that including an arterial compliance component results in more physiological flow profiles than using rigid arterial wall models[159–162]. In addition, biaxial deformation testing has shown that circumferential deformation in fresh human cerebral arteries occurs with much less resistance than axial deformation[163], highlighting that cerebral arteries are able to show compliant behaviour.

Currently, ultrasound echo-tracking of arterial walls to obtain maximum (systolic) and minimum (diastolic) diameters with simultaneous measurement of local pulse pressure (the difference between systolic and diastolic blood pressure) is one of the standard methods to assess local AC[164,165], whether it be in peripheral (e.g. radial[166]) or more central (e.g. carotid[167]) arteries. However, echo-tracking of cerebral arteries is difficult because the skull reflects most of the ultrasound waves[168]. One ultrasound method that is currently used to assess cerebral AC is transcranial Doppler ultrasound (TCD)[79,80,169], which detects blood flow velocities from accessible cerebral arteries (mainly the middle cerebral artery). One drawback of TCD is that it cannot measure arterial geometry, such as volume or diameter, directly and therefore either a mathematical model is used to transform blood flow into volume, which assumes that there is no change in arterial diameter[79,80], or arterial stiffness is assessed with the augmentation index, a parameter based on the wave form of the blood flow velocity[169]. Another drawback of TCD, in particular for the middle cerebral artery (MCA), is that thickness of the temporal bone renders it impossible to measure MCA flow velocities in approximately 20 % of the population[170].

We propose a method that enables measurement of cerebral aBV based on short inversion time (TI) pulsed arterial spin labelling (PASL)[26]. PASL is a method in which arterial blood is magnetically labelled before it reaches the volume of interest and is usually applied to measure tissue perfusion, which is the delivery of blood to the capillary bed of the brain. Images containing perfusion weighted signal are calculated by subtracting a tag image from a control image. The latter acquired without any labelling of arterial blood. Before acquisition of the label image blood is magnetically labelled when it flows through the major brain feeding arteries (i.e. internal carotid and vertebral arteries) and image acquisition takes place after leaving time (> 1 s) for the labelled blood to pass into the cerebral capillary bed. However, before arriving at the capillary bed the labelled blood first has to pass through the macrovasculature of the brain. Imaging at short inversion times (< 1 s) therefore results in ASL images in which the major arteries, such as the MCAs, posterior and anterior cerebral arteries (PCAs, ACA), are clearly visible.

The aim of the current study is to show the feasibility of non-invasive measurement of AC by exploiting the signal arising from the cerebral arteries at short inversion time PASL.

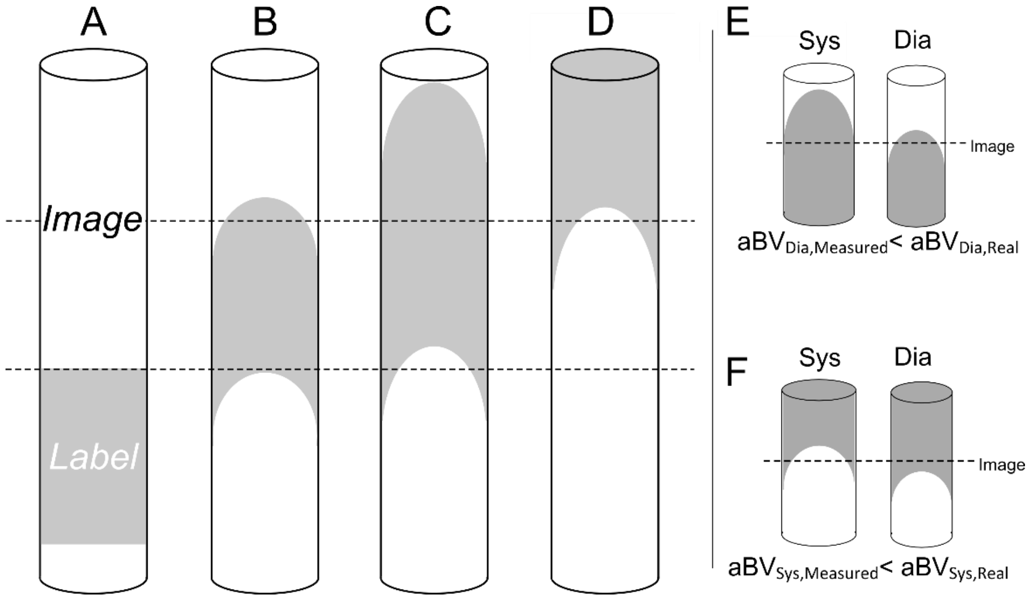

Figure 6.1. A-D Schematic of the labelled bolus in pulsed ASL evolving over time. In order to measure arterial blood volume with a single inversion time it is important that all the arterial blood in the image is labelled, as is the case in C. Due to dispersion of the label there will be times when not all the arterial blood in the image is labelled, as is the case in B and D. Assessing arterial blood volume (aBV) in systole (sys) and diastole (dia) with a single inversion time can be prone to error. When imaged too early, the diastolic blood volume is underestimated (E). When imaged too late the systolic blood volume is underestimated (F).

Modelling arterial blood volume

In measuring arterial blood volume with pulsed arterial spin labelling it is important to account for changes in the kinetics of the labelled bolus due to the cardiac cycle, such as differences in bolus arrival time[27,28]. In addition, as the label progresses through the vasculature dispersion takes place, which means that the leading and trailing edges of the bolus are not well-defined (see Figure 6.1A-D). If a single inversion time is used to assess blood volume, the cardiac phase related changes in label kinetics may cause underestimation of aBV, as illustrated by Figure 6.1EF, which in turn will confound calculation of arterial compliance. To account for changes in arrival time and dispersion we therefore model the arterial blood volume based on multi inversion time pulsed arterial spin labelling data.

Here we model the arterial signal by extending the macrovascular compartment described previously by Chappell et al.[26], which assumes plug flow in large arteries, with a Gaussian kernel to account for dispersion as has been introduced previously by Wu et al.[27]:

$$\Delta M(t) = \begin{cases} 0 & 0 < \Delta t_{art} \\ 2\alpha M_{0,a} e^{-\frac{1}{T_{1a}}} aBV[w(t) * \mu(\sigma, t)] & \Delta t_{art} \leq t \leq \Delta t_{art} + \tau \\ 0 & \Delta t_{art} + \tau < t \end{cases} \quad \text{Eq. 6.1}$$

with ΔM(t) the difference signal arising from subtracting tag and control PASL images, aBV is the arterial blood volume in fraction of the voxel volume ($\%_v$), Δt_{art} is the bolus arrival time in the microvasculature (in ms), τ is the bolus duration (in ms), α=1 (label efficiency) and $T_{1,a}$ = 1664 ms (T_1 arterial blood at 3T)[171]. $M_{0,a}$ can be determined based on the equilibrium magnetisation of CSF ($M_{0,CSF}$) according to methods previously described by Wong et al.[13]. Furthermore, *w(t)* is a square weighting function with the same width as the label duration (τ):

$$w(t) = \begin{cases} 1 & 0 \leq t \leq \tau \\ 0 & \tau < t \end{cases} \quad \text{Eq. 6.2}$$

which is convolved with a Gaussian kernel centered on Δt_{art} and with width σ to model dispersion:

$$\mu(\sigma, t) = \frac{1}{\sigma\sqrt{2\pi}} e^{\frac{-((t-\Delta t_{art})^2}{2\sigma^2}} \quad \text{Eq. 6.3}$$

It is important to note that, although PASL is most commonly performed to assess tissue perfusion, here the interest lies solely on measuring the PASL signal of the macrovasculature. For this purpose, only short inversion time PASL with inversion times shorter than 1 s are used and regions of interest (ROI) are drawn that only contain voxels with a relatively large arterial compartment (see Methods section for more details). The short inversion times ensure that the signal coming from the brain parenchyma is small in comparison to the signal coming from large arteries. Even though arrival times of the label into the microvasculature (Δt_{tiss}) have been reported to be as short as 700 ms for proximal brain regions (i.e. 40 mm from distal end of the labelling region[39]), the maximum tissue signal is still reported to occur at time points well over 1 s[39,90,109]. In addition, the ROI used here have a large macrovascular compartment which ensures that the maximum macrovascular signal is in fact 6 to 10 times larger than the maximum tissue signal[39].

In order to illustrate the minimal interference of signal coming the microvasculature at short inversion times, the signal from a voxel containing both macrovascular and microvascular compartments was simulated up to 2.5 seconds after PASL labelling by adding a tissue signal model described previously[26] to Eq. 6.1. The aBV was set to range between 0.1 $\%_v$ and 10 $\%_v$, the tissue perfusion was set at 60 ml/100 g/min and Δt_{tiss} was 350 ms later than the arterial arrival time, which is in line with previous ASL studies that have included flow crushing gradients to estimate the macrovascular and microvascular arrival times[39]. For each of the simulated signal curves, Eq. 6.1 was then fitted to the signal at 7 inversion times (all < 1 s) to give an estimate of aBV. Results from this simulation study showed that when the underlying aBV was larger than 1 $\%_v$ the aBV calculated based on early inversion times only, overestimates the true value by less than 5 % for Δt_{tiss} = 700 ms (see Figure 6.2).With either larger underlying aBV or larger Δt_{tiss} the overestimation of aBV becomes smaller. In the current experiment, the PASL data is therefore analysed without the microvascular compartment and an estimate of tissue perfusion is not given.

6.2. Materials and Methods

Imaging data were acquired on a 3 T whole body MRI system (GE Excite HDx, Milwaukee, WI) using an eight-channel receive-only head coil. Informed consent was obtained from all volunteers under ethical approval from the Cardiff University School of Psychology Ethics Committee and all experiments were performed in accordance with the guidelines stated in the Cardiff University Research Framework (version 4.0, 2010).

Image acquisition

Multi inversion time PICORE PASL acquisitions were performed on five healthy volunteers (age 25.4 ± 1.5 years). Seven inversion times (TIs) were acquired in random order (250 – 850ms, spacing 100 ms, separate scan series). Note that all TIs < 1s, as explained in the *Theory* section. The label was applied 10 mm below the most proximal slice and had a width of 200 mm. A QUIPSS II[13] cut off of the label was applied at 700 ms for inversion times > 700 ms. Images were acquired with a spiral gradient echo sequence (TE=2.7 ms, TR = 1400 ms, 80 tag-control pairs per TI, 14 slices, slice gap 1 mm, slice delay 29 ms, voxel size 3x3x7 mm^3). A fully relaxed (infinite TR) calibration image was obtained with the same acquisition

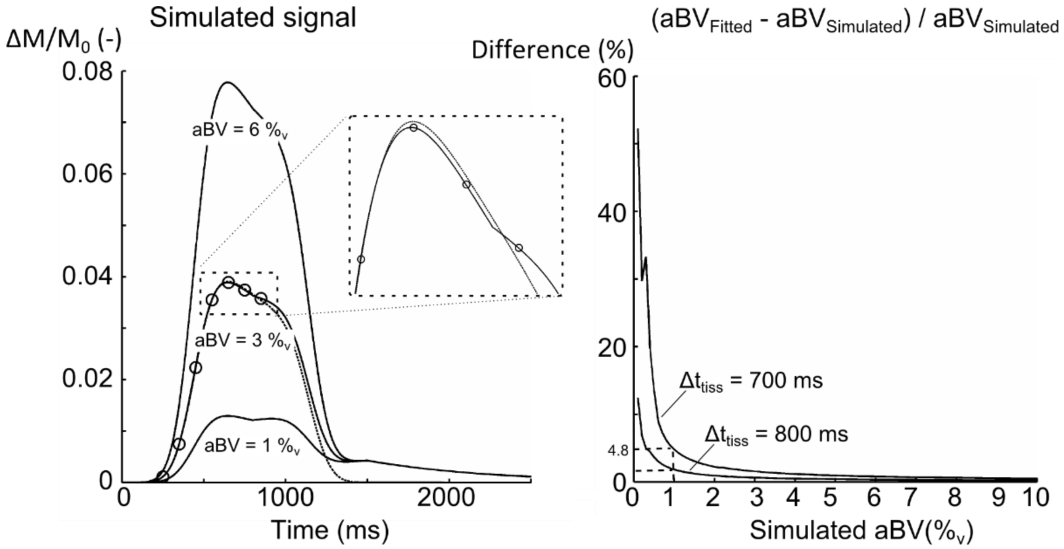

Figure 6.2. *Left*: simulated $\Delta M/M_0$ signal from a voxel containing a macrovascular and microvascular compartment. The microvascular compartment was simulated with previously described methods[26], the cerebral blood flow was set to be 60 ml/100 g/min and the tissue arrival time (Δt_{tiss}) at 800 ms. Arrival time of the labelled bolus at the microvasculature was set to be 450 ms, and aBV ranged from 0.1 % to 10 %. The resulting two compartment model is plotted (solid lines) for aBV = 1, 3, and 6 %. Seven time points < 1 s were then used (open circles) to fit Eq 1 to estimate aBV. An example of this fit is plotted (dotted line) for aBV = 3 $\%_v$. The inset shows how the fitting aBV with only the short inversion time slightly overestimates the true aBV. *Right*: The differences of the fitted aBV, based on the 7 short inversion times, and the simulated aBV is plotted versus the simulated aBV ($\%_v$). The difference is plotted as a percentage change: 100% * ($aBV_{fitted} - aBV_{simulated}$) / $aBV_{simulated}$. This plot shows that for Δt_{tiss} = 700 ms and $aBV_{simulated}$ > 1 %, using only the short inversion times leads to overestimation of aBV of less than 5 %. This overestimation becomes smaller with increasing aBV, and increasing Δt_{tiss}.

parameters but without labelling, to obtain the equilibrium magnetisation of cerebrospinal fluid ($M_{0,CSF}$).

Blood pressures

The cardiac cycle was monitored by finger plethysmography. Brachial artery blood pressure (BP) was measured non-invasively with an MRI compatible blood pressure cuff once for each ASL scan (OMRON, Tokyo, Japan). Per participant, the seven BP measurements were used to calculate average systolic and diastolic blood pressure (BP_{sys} and BP_{dia}).

Image analysis

PASL time series were motion corrected using *mcflirt* within the FMRIB Software Library v5.0 (FSL-http://fsl.fmrib.ox.ac.uk)[115]. Retrospective synchronisation was then performed using in-house programmes written in MATLAB R2012b (Mathworks, Natick, MA, USA). A time shift of 225 ms was applied to the finger plethysmograph trace to account for the delay between the cerebral and finger pulse. This time period was deduced from literature as the difference between the delay time between the R-peak in the electrocardiogram and the left finger and the time delay between the R-peak in the ECG and the onset of the carotid pulse wave[172]. Images were further analysed on slice-by-slice basis, taking into account the slice time delay of 29 ms. The normalized cardiac phase (φ_c) of each acquired slice was determined according the following:

$$\varphi_c = (t_{acq} - t_1)/(t_2 - t_1) \qquad \text{Eq. 6.4}$$

where t_{acq} is the time of the slice acquisition, t_1 the time of the previous systolic peak in the shifted plethysmography trace and t_2 the time of the following systolic peak in the plethysmography trace. Thus, the cardiac cycle is then advancing linearly from 0 to 1 during a single cardiac cycle and is then set to 0 for the next cardiac period. The cardiac cycle was divided into 8 bins, i.e. the first bin containing slices acquired with $0 \leq \varphi_c < 1/8$, the second bin containing slices acquired with $2/8 \leq \varphi_c < 3/8$ and so on. Slices acquired in "early diastole" corresponded to those with $1/8 \leq \varphi_c \leq 2/8$ and slices acquired in "early systole" were those with $6/8 \leq \varphi_c \leq 7/8$. Average tag and control images were calculated and subtracted to obtain maps of ΔM for each of the 8 cardiac phases at each of the 7 TIs.

The number of tag and control images in each cardiac phase was noted in order to analyse whether the synchronisation led to any bias for a particular cardiac phase or inversion time.

Calculation of parameter maps

Eq. 6.1 was used to estimate aBV, Δt_{art}, and σ on a voxelwise basis for each of the 8 cardiac phases separately (least-square fitting, *lsqcurvefit* in MATLAB). The additional slice acquisition delay of 29 ms for each subsequent slice was taken into account in the fitting procedure. The bolus duration (τ) was fixed at 700 ms by the QUIPSS II cut-off. Maps of aBV_{Dia} and aBV_{Sys} were used to calculate arterial compliance (AC) according to:

$$AC = 100\% \cdot \frac{aBV_{Sys} - aBV_{Dia}}{aBV_{Dia\cdot}\left(BP_{Sys} - BP_{Dia}\right)} \qquad \text{Eq. 6.5}$$

Note that here AC is normalized for the arterial blood volume in diastole and is therefore calculated as percentage change in aBV per mmHg (%/mmHg).

Regions of interest

For each participant, an average ΔM image was obtained for the full time series of TI = 750 ms (i.e. the average of 80 tag-control difference images). Regions of interest (ROI) were determined based on data from TI = 750 ms because on average this was the inversion time with the maximum intensity in the raw difference images (data not shown). A mask of the TI = 750 ms ΔM image was created such that each slice only contained the 5 % of voxels with the highest intensities (the 95th percentile intensity threshold was determined for each slice separately). Broad regions of interest were manually drawn around the vascular territories within each slice. For instance, in the slice just above the Circle of Willis these regions were drawn to encompass the flow territories of the right middle, left middle, right posterior, left posterior and anterior cerebral arteries (RMCA, LMCA, RPCA, LPCA, and ACA). The ROIs of the flow territories were then calculated by multiplying each of the broad masks with the thresholded ΔM image. Note that there is only one ROI for the ACA, because the voxel size used for image acquisition did not allow for separation of the left and right ACA.

Statistics

A three-way repeated measures analysis of variance (RM-ANOVA) was used to assess whether there were significant differences in number of tag and control images per cardiac phase after retrospective synchronization of image acquisition with the cardiac cycle. *TI*, *ROI* and *cardiac phase* (systole vs. diastole) were used as independent variables. To investigate differences in aBV, Δt_{art} and σ between flow territories and between cardiac phase a two-way RM-ANOVA was performed with *ROI* and *cardiac phase* (systole vs. diastole) as independent variables. Note that only the diastolic and systolic parameter maps are used for the above RM-ANOVAs. To assess differences in arterial compliance between different flow territories a one-way RM-ANOVA was performed, with *ROI* as independent variable.

6.3. Results

All relevant subject information is summarized in Table 6.1. The average pulse pressure ($BP_{Sys} - BP_{Dia}$) was 52.7 ± 9.5 mmHg with an average heart rate of 65.4 ± 10.0 beats per minute (bpm).

Retrospective resynchronisation of image acquisition with the cardiac cycle did not lead to any bias towards a particular inversion time (RM-ANOVA, $F(6,24) = 0.804$, $p=0.557$). On average, out of the 160 images acquired for a single inversion time there were 10 tag and 10 control images in diastole, and 10 tag and 11 control images in systole.

Fitting the model on a voxel by voxel basis lead to individual parameter maps for aBV, Δt_{art}, and σ calculated for 8 different cardiac phases. An example of fitting the model to data from a single voxel in early systole ($6/8 \leq \varphi_c < 7/8$) and early diastole ($1/8 \leq \varphi_c < 2/8$) can be seen in Figure 6.3. Regional aBV and Δt_{art} showed consistent variation along the cardiac cycle in all participants (an example can be seen in Figure 6.4). Median values were calculated for the aforementioned five flow territories just above the circle of Willis in systole and diastole (see Figure 6.5). Repeated measures ANOVA showed that aBV_{Sys} was significantly higher than aBV_{Dia} for each of the five ROIs (pairwise comparisons $p < 0.05$, after RM-ANOVA showed significant effect of cardiac phase on aBV $F(1,4) = 16.5$, $p <0.02$). Also, on average $\Delta t_{art,Sys}$ was 41 ms longer than $\Delta t_{art,Dia}$ (RM-ANOVA significant effect of systole vs. diastole, $F(1,4) = 22.9$, $p<0.01$). In addition, σ_{Dia} was on average 30 ms larger than σ_{Sys} for the LMCA and ACA, although this was not significant (RM-ANOVA, effect of cardiac phase on σ $F(1,4) = 7.37$, $p =0.0533$).

Table 6.1. Summary of participant data (3 males, 2 females). Mean and standard deviations are shown.

Subject	Age [years]	Sex [M/F]	BP (Sys/Dia - PP) [mmHg]	Heart rate [bpm]	Slice just above circle of Willis [Z number]
I	28	M	122/56 – 66	59.8	4
II	24	M	119/62 – 57	50.6	4
III	25	F	108/66 – 42	71.7	3
IV	25	F	110/64 – 46	69.5	3
V	25	M	119/66 – 53	75.2	4

M = Male, F = Female, BP = Blood pressure, Sys = systole, Dia = diastole, bpm = beats per minute (averaged over 7 acquisitions)

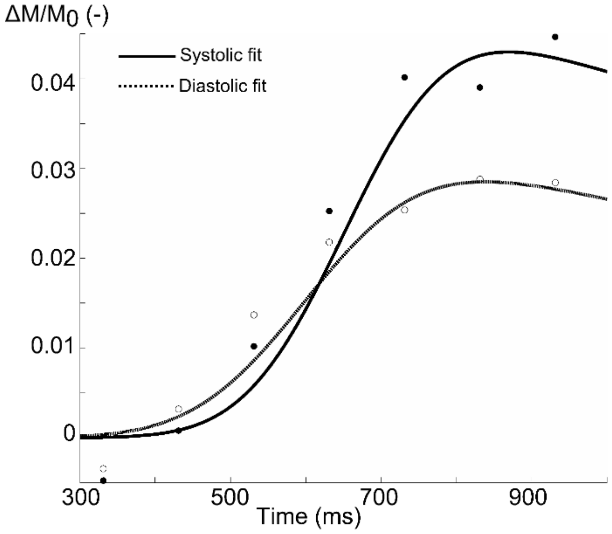

Figure 6.3. Example of model fit for a single voxel in the flow territory of the RMCA of one subject. Note that although signal intensities were calculated for 8 different cardiac phases, only systolic (•) and diastolic (◦) data points are shown here. Data were corrected for slice time acquisition.

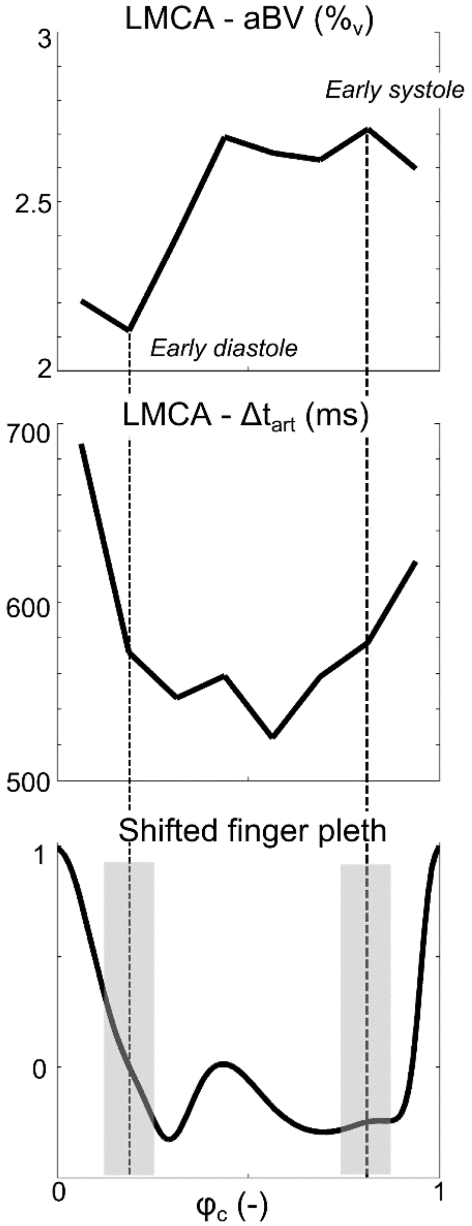

Figure 6.4. Example of fitted aBV (top) and Δt_{art} (middle) calculated for each of the 8 cardiac phases. The full trace of the cardiac cycle can be seen in the bottom image. This data is from the LMCA flow territory of subject V. Note how these images clearly show cardiac cycle related variation in aBV and Δt_{art}. Images acquired in early diastole had $0.125 \leq \varphi_c \leq 0.25$ and in early systole had $0.75 \leq \varphi_c \leq 0.875$ (grey bars in the bottom image).

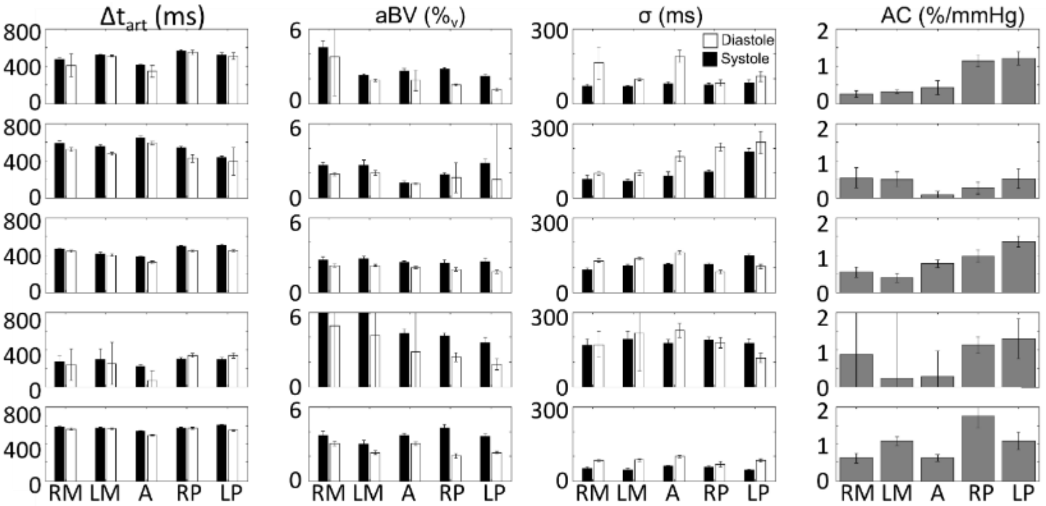

Figure 6.5. Regional median results for aBV, Δt_{art}, σ, and AC for each individual subject (I-V) calculated for the slice just above the circle of Willis. aBV, Δt_{art}, and σ are given for systole (black) and diastole (white). AC is calculated as percentage increase in aBV in systole compared to diastole. Errorbars indicate one standard error of the mean. RM-ANOVA showed that $aBV_{Sys} > aBV_{Dia}$ for each ROI (pairwise comparisons, $p<0.05$, after a significant effect of the interaction between ROI and systole vs. diastole was found, $F(4,16) = 4.2$, $p <0.03$). *RM = right middle cerebral artery, LM = left middle cerebral artery, A = anterior cerebral artery, RP = right posterior cerebral artery, LP = left posterior cerebral artery.*

Individual values for AC for the slice just above the circle of Willis can be seen in Figure 6.5. Averaged over five subjects AC values calculated for the RMCA, LMCA, ACA, RPCA, and LPCA were 0.57 ± 0.20 %/mmHg, 0.50 ± 0.30 %/mmHg, 0.43 ± 0.24 %/mmHg, 1.1 ± 0.48 %/mmHg, 1.1 ± 0.30 %/mmHg, respectively. Note that these values for AC indicate that we have measured aBV changes within the cardiac cycle from 25 % to 50 % (multiplying AC with the pulse pressure).

Examples of the aBV maps in diastole and systole and the resulting maps of AC containing the slice just above the circle of Willis can be seen in Figure 6.6.

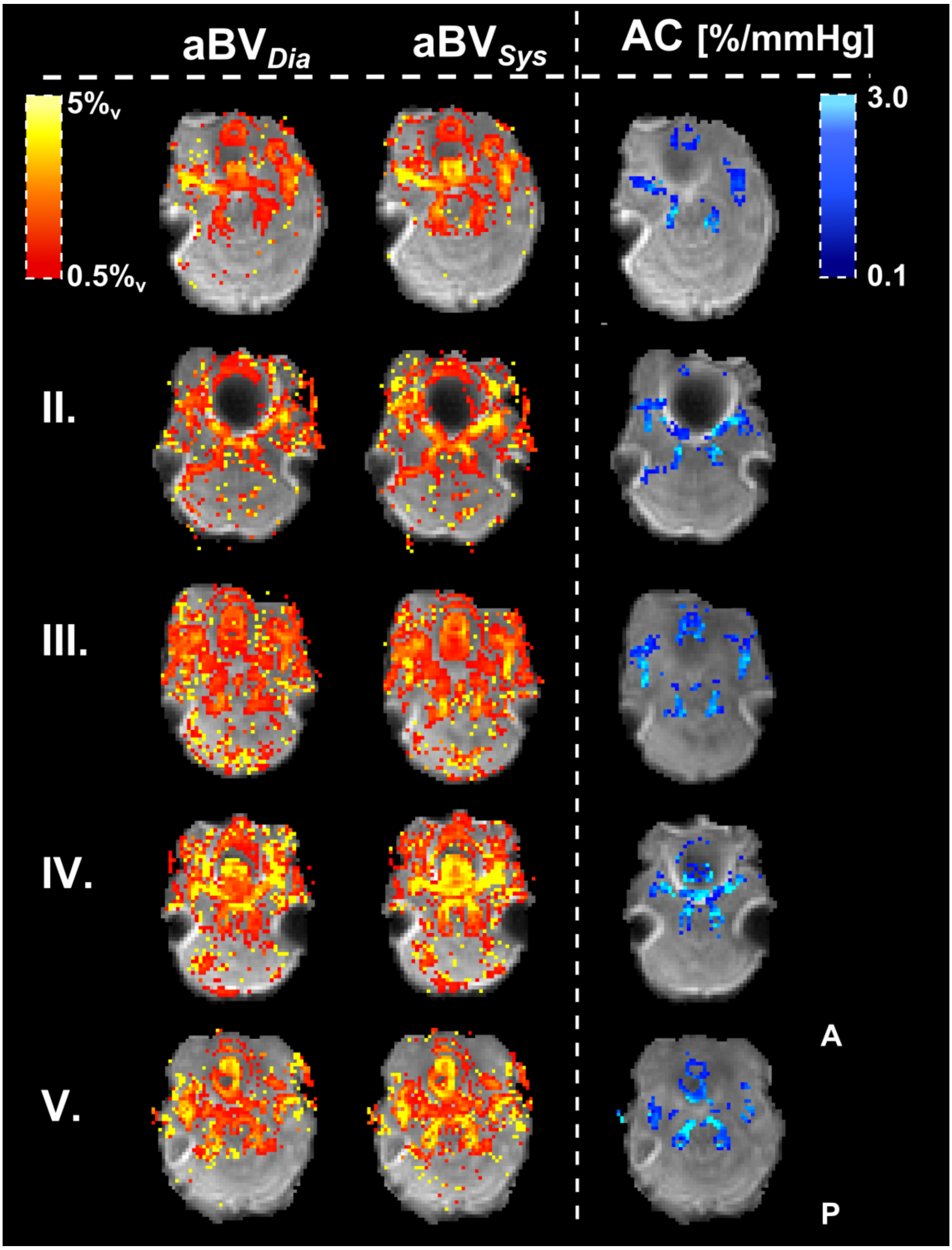

Figure 6.6. Maps of aBV (%$_v$) just above the circle of Willis. aBV$_{Dia}$ and aBV$_{Sys}$ are plotted for each individual (top row shows Subject I). The calculated AC maps are plotted in the right column. Note how AC here is normalized for aBV$_{Dia}$ and is therefore showing percentage increases in aBV between systole and diastole per mmHg increase in blood pressure. The AC maps are masked, showing only the voxels used to calculate flow territory averages. *A = Anterior, P = Posterior.*

6.4. Discussion

The current study has shown the feasibility of non-invasive assessment of arterial compliance of major cerebral arteries by retrospective synchronization of short inversion time arterial spin labelling images with the cardiac cycle. In addition to finding significant differences between systolic and diastolic arterial blood volume, we have also found differences in dispersion and arrival time which can be attributed to the pulsatility of the cardiac cycle.

Pulsatility of the cardiac cycle

Although it is well known that pulsatility of the cardiac cycle causes modulation of PASL signal[27,173], to our knowledge this is the first study actually exploiting this modulation of PASL signal to assess cerebrovascular arterial compliance. In particular, here we robustly show that aBV changes in line with the cardiac cycle (Figure 6.4), which is as expected based on elastic properties of the cerebral arteries[174] as well as on arterial compliance measured in arteries outside the brain[175].

One important aspect of assessing cardiac pulsatility of the PASL signal in the *imaging* volume is accounting for the effect that the cardiac phase of the *labelling* slab has on PASL signal. That is, it is important to ensure that the changes in aBV we find in the *imaging* volumes are truly caused by changes in arterial volumes and not by differences caused by labelling at different cardiac phases. For instance, previous work has shown that PASL with a QUIPSS II cut off at 700 ms can lead to differences in signal coming from the brain parenchyma of up to 16% between applying the labelling pulse in systole or diastole[27]. To investigate the effect of the cardiac phase on the label, the PASL time series acquired here were also retrospectively synchronized to the cardiac cycle based on the cardiac phase of the label. Effectively, an image volume for a single cardiac phase now exists of slices that result from labelling at a fixed time within the cardiac cycle, meaning that each *imaging* slice will be acquired in a later cardiac phase due to the present of the slice delay. Maps for aBV and Δt_{art} were calculated by fitting the model to these images the same way as described in the Methods section. The main finding from this analysis is that the cardiac phases with maximum and minimum aBV ($\varphi_{aBV,max}$ and $\varphi_{aBV,min}$) resulting from synchronization according to cardiac phase of the label showed a dependency on slice location, shifting along the cardiac cycle for more distal slices (Illustrated by Figure 6.7).

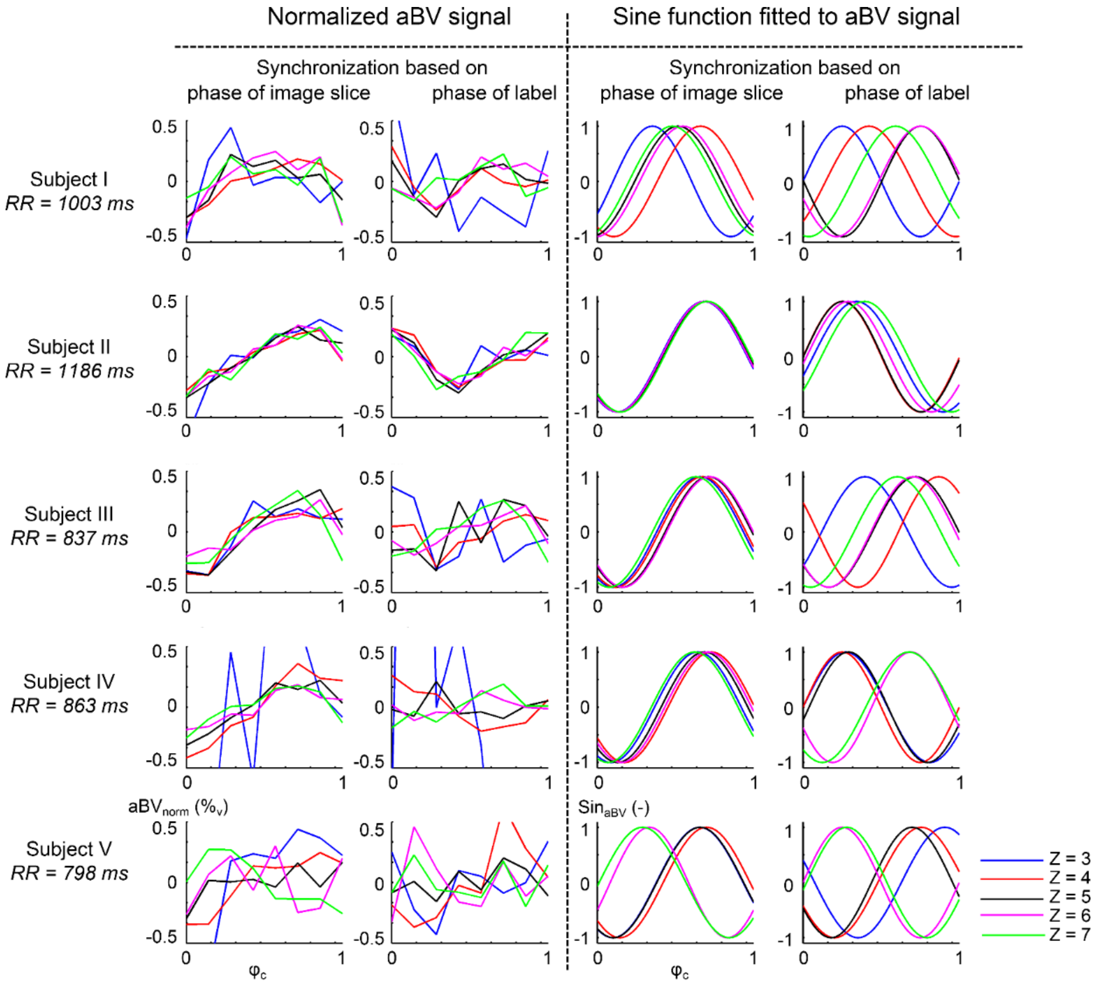

Figure 6.7. To illustrate the dependency of arterial blood volume (aBV in volume percentage of the voxel) on the cardiac phase (φc) of the imaging volume here results are shown for the aBV in the flow territory of the left middle cerebral artery (LMCA) for 5 consecutive slices (coloured lines, Z = 3 t/m 7). Each row contains data from one subject. The two columns on the left show aBV$_{norm}$ (aBV – the average aBV over the cardiac cycle). The two columns on the right show sine waves fitted to the data on the left to highlight the difference between synchronisation based on cardiac phase of the image and label (amplitudes of the sine waves are set to 1). When the imaging data is retrospectively synchronized according to the phase of the imaging slice, the cardiac phase for which aBV is maximum is similar for all 5 consecutive slices (column 1 and 3), because all slices are acquired in the same cardiac phase. When the data is retrospectively synchronized according to the phase of the label the cardiac phase for which aBV is maximum shows a dependency on slice location. If images are synchronized based on when the label has occurred, there will be differences in cardiac phase of consecutive slices because a 2D acquisition scheme is used with a slice delay of 29 ms. In particular in participants with a shorter beat-to-beat period (RR interval) the dependency of aBV on the cardiac phase of the imaging slice becomes more apparent (compare subject III with subject II), illustrated by the dispersion of cardiac phases in data synchronized with the cardiac phase of the label compared to the data synchronized based on the cardiac phase of the image.

The fact that $\varphi_{aBV,max}$ and $\varphi_{aBV,min}$ shift for more distal slices when the label is applied in the same phase for each of the slice acquisitions shows that the aBV within the slice follows the cardiac phase of the slice itself, rather than being determined by the cardiac phase of the label location at time of labelling. An important note here is that, when images are sorted according to the cardiac phase of the label and 14 slices are acquired with a slice delay of 29 ms, there is a cardiac phase difference ($\Delta\varphi_c$) of more than 0.4 (406/1000ms) between the most proximal and most distal slice acquired for the average heart rate of 60 beats per minute (R-R interval of 1000 ms). The fact that this phase shift is measurable with the aBV resulting from data that are synchronized based on when the label is acquired shows that the effect of the cardiac phase of the label on assessing aBV in the *imaging* volume is less important than the cardiac phase of the slice itself. Moreover, if there would be a significant effect of the cardiac phase of the label, a similar dependency of $\varphi_{aBV,max}$ and $\varphi_{aBV,min}$ on slice location should be present in the dataset that is sorted based on the cardiac phase of the *imaging* slice. The fact that systolic and diastolic phase are the same in almost all slices in the current study (i.e. early systole: $6/8 \leq \varphi_c < 7/8$ and early diastole $1/8 \leq \varphi_c < 2/8$), suggests that the effect of the cardiac phase of the label is indeed minimal (illustrated by Figure 6.7).

In short, the findings from the analysis in which the PASL time series were sorted according to the cardiac phase of the *label* show that even if there is an effect of the cardiac phase of the label on measured aBV, this effect is small relative to the change in arterial volume caused by the cardiac cycle in the *imaging* volume and is therefore considered negligible in the current study.

Previously reported AC of cerebral arteries

Due to the difficulty of in vivo measurement of local cerebral AC reference values for healthy cerebral arteries are difficult to find. Interestingly, Giller et al.[77] performed measurements of outer arterial diameters during craniotomies of 10 patients with varying pathologies and from their data it can be derived that they measured changes in volume related to changes in blood pressure in exposed MCAs (M2 segment) and ACAs of 0.6 %/mmHg and 0.9 %/mmHg, respectively. Our volume related changes for the MCA (0.54 %/mmHg, averaged over right and left) compare well with derived volume changes as reported by Giller et al.[77], while it appears that here we underestimate the compliance in the ACA (0.43 %/mmHg). It is important to note however, that the circumstances in which Giller et al. measured changes in arterial diameters may not be reflective of true in vivo AC as several factors during craniotomy may affect compliance and pulsatile behaviour of exposed arteries, such as a change in transmural pressure of the artery due to exposure, the anaesthesia used, and the pathology present[77]. However, it remains of interest that, despite the obvious differences in methods of measuring AC, Giller et al. do measure larger changes in diameter of smaller arteries which is also suggested by our finding of significantly larger AC in the PCA segments branching from the Circle of Willis.

A direct comparison between AC reported here and AC values derived from TCD ultrasound should be interpreted with caution. As mentioned in the introduction, TCD (of the MCA) is restricted to the measurement of blood flow velocity and in order to estimate compliance assumptions on vessel diameter have to be made. For instance, in the method described by Kim et al.[79] the assumption is made that there is no change in MCA diameter, neither over the cardiac cycle nor when intracranial pressure increases, and the MCA velocity profile is then used to model arterial inflow and venous outflow of the arterial bed distal to the location of insonation. The compliance measure that is calculated then does not reflect compliance of the MCA, but of the arterial bed distal to the MCA[79,80]. Moreover, only relative changes in compliance relating to changes in physiological state (i.e. change in intracranial pressure[79] or occlusion of the internal carotid artery[80]) are then reported, which confounds comparison with measurements of aBV changes over the cardiac cycle in distinct cerebral arteries as has been done here.

Another cerebral compliance measure derived from TCD data is the augmentation index (AI), which is calculated as the ratio of the difference between velocities at the return of the pulse wave reflected by the distal arterial bed and at diastole and the differences between systolic and diastolic velocities in the flow profile of the insonated vessels (MCA and PCA in the experiment done by Flück et al.)[169]. Although detection of the pulse wave reflected by the more distal vascular bed is in part determined by the stiffness of the arterial wall at the location of insonation, because pulse wave velocity is linked to arterial stiffness, it is also highly influenced by the vessel branching and vessel wall properties of the distal arterial bed[164,169,175]. In contrast to the results presented here, Flück et al. report a higher AI for the

PCA (80.5 %) than for the MCA (76.1 %) in young individuals, suggesting that the PCA is less compliant. However, the dependency of the cerebral AI on both the distal arterial bed and the stiffness of the arterial wall at the location of insonation inhibits the separate estimation of these parameters and again illustrates that our current method gives complementary information to the TCD estimates of arterial stiffness.

Current models of pressure-flow relationship in the cerebral vasculature are in general validated with TCD measurements of blood flow velocity profiles through accessible cerebral arteries[160,161,176] and therefore also stress that the compliance parameters included in these models reflect the capacitive behaviour of the distal arterial bed instead of local arterial wall properties[160]. Furthermore, values used for arterial compliance vary in order of magnitude between different models. For instance, Alastruey et al.[162] use one-dimensional pressure-flow models of compliant arteries to model the Circle of Willis and use values ranging from 8.3 µl/mmHg, for the arterial bed distal to the PCA, to 15.5 µl/mmHg for the arterial bed distal to the MCA. In contrast, Reymond et al.[161] also use one-dimensional models of pressure and flow to model the Circle of Willis and use compliance values ranging from 0.028 µl/mmHg to 0.058 µl/mmHg for the arterial beds supplied by the MCA and PCA, respectively. Although both studies use similar assumptions to calculate the compliances, including that the total systemic compliance is distributed over all compliances in the full model and that the local geometry of the arteries is taken into account, differences arise due to the literature-based values each study uses for the cerebral geometry and total systemic compliance[161,162]. As an example, when combining our results of normalized AC with the volumes for arterial segments derived from the data used by Reymond et al.[161], we would come to 0.15 µl/mmHg, 0.089 µl/mmHg, and 0.03 µl/mmHg for MCA M1, ACA A1, and PCA P1, respectively, values that fall within the range of compliances used in the modelling literature[161,162].

Interestingly, a recent study performed by Yan et al.[46] also uses ASL to assess AC and reports changes in aBV in large cerebral arteries of about 46% over the cardiac cycle while the AC values reported here correspond to a change in aBV over the cardiac cycle of approximately 23%, 28%, and 58% in the ACA, MCA, and PCA, respectively. Although Yan et al. used a different ASL method[46] to assess aBV, combining their results with the current AC values for local flow territories suggests that ASL based methods for detecting changes in aBV related to the cardiac cycle are consistent.

In short, ASL derived measurements of arterial stiffness are difficult to compare directly to compliance measurements of the cerebral vasculature derived from different methodologies, such as TCD. Our method of local AC measurement has the potential of giving complementary information to TCD-based estimates of compliance. Reports on in vivo local arterial compliance are scarce in literature, but comparison to values derived from previous experiments seems to suggest the reported AC values found here are plausible.

Methodological considerations

In the current experiment no model of tissue perfusion is included, even though PASL is conventionally used to assess this physiological parameter. The main reason for not including this compartment in the model is the fact that the inversion times used here are below 1 s, which means that the majority of the labelled blood has not reached the capillary bed of the brain yet and therefore no perfusion has taken place. However, at TI = 850 ms some perfusion might have still taken place, since transit delays from the blood to the capillary bed of more proximal brain regions have been reported to be less than 900 ms[37,90]. However, the simulation study described in the Theory section showed that a short arrival time of the label to the capillary bed (of 700 ms), would result in a maximum overestimation of aBV of 5 %, when the underlying aBV is higher than 1$\%_v$. As an example, the resulting aBV_{Dia} for the LPCA here (group average aBV_{Dia} = 1.68 $\%_v$ with $\Delta t_{art,Dia}$ = 445 ms) indicate that this is an overestimation of 1.2 %, meaning that the true aBV_{Dia} would actually be 1.65 $\%_v$. This level of overestimation is deemed acceptable in the current study.

It is important to note that, although overestimation of aBV is marginal, it is dependent on the true arterial blood volume and decreases with increasing aBV (as is illustrated by Figure 6.2). This means that the estimates for aBV_{Dia} are more biased than the estimates for aBV_{Sys} and, because compliance depends on $aBV_{Sys} - aBV_{Dia,}$ the AC might therefore be underestimated. However, as illustrated by the example of the LPCA as stated above, the fact that the ROIs used here only contain voxels with a sufficiently large aBV (> 1.5$\%_v$) ensures that not including later inversion times has limited effect on the arterial compliance measurement.

One obvious confound of the current study is using brachial blood pressures as a surrogate for intracranial blood pressures. Pulse pressure in the common carotid artery is lower than in the brachial artery, because the peripheral brachial artery is located closer to reflection sites of the pressure wave through the vascular tree[164]. Use of the brachial pulse pressure could, therefore, result in an underestimate of cerebral AC. Distal to the carotid arteries the pulse pressure decreases even further until it is (almost) 0 in the capillary bed to facilitate exchange of oxygen and nutrients in the cerebral tissue[177]. The cerebral arteries of interest here lie in between the common carotid and the capillary bed, which means that an invasive measurement would be necessary to obtain local pulse pressures.

In order to obtain perfusion weighted ΔM images within the ASL technique it is required to subtract tag from control images. The retrospective synchronisation of image acquisition to the cardiac cycle used here can result in an unbalanced number of tag and control images used to calculate the ΔM images. When the number of tag or control images used to calculate a ΔM of a particular cardiac phase becomes too small, there is a potential to lead to biased measurements of aBV_{Sys} or $aBV_{Dia.}$ In particular when motion is present within the time series. However, the current data set does not reveal any bias towards the number of images used to calculate systolic and diastolic aBV maps, which is likely due to the use of a repetition time different from the beat-to-beat period of the cardiac cycle of healthy participants.

Lastly, it should be noted that cerebral aBV can be measured with different MRI methods as presented here, some of which could be synchronized to the cardiac cycle and therefore have the potential to assess cerebral AC as well. For instance, Yan et al. have already combined ASL with a balanced steady-state free procession (bSSFP) read-out to assess AC within large arteries and smaller arterioles[46]. One drawback of Yan's method is that it is a single slice method, making it less time efficient as the multi-slice method we propose here for investigation of AC throughout the brain. Vascular space-occupancy (VASO) with dynamic subtraction is another method that can quantify aBV, by assessing differences between images in which blood signal is nulled and images without nulling of blood signal[43]. However, VASO is currently optimised to assess precapillary aBV on a single-slice basis and, because the time of imaging depends on the repetition time of the pulse sequence, would require adaption to assess aBV of larger arteries at different times within the cardiac cycle.

The current study has shown the feasibility of measuring local arterial compliance of cerebral arteries with short inversion time pulsed arterial spin labelling and has resulted in plausible estimates of local AC. Compared to TCD, measurement of AC with PASL has the benefit of measuring AC based on local arterial wall properties instead of assessing compliance of the arterial bed distal to the location of measurement and therefore has the potential to give complimentary information about the health of cerebral arteries.

Chapter 7

The effect of increased sympathetic nerve activity on cerebrovascular physiology

In vivo human data on the effects of elevated sympathetic outflow on the cerebrovasculature are missing from literature because of the difficulty of performing non-invasive measurement of cerebrovascular and medullar physiology. In this study we show that with the perfusion based imaging methods from chapters 4 and 6 it is possible to investigate the effect of sympathetic outflow on cerebrovascular physiology. In 8 healthy male volunteers we measured cerebral arterial compliance (AC) and medullar CBF (CBF_{MD}) during post exercise ischemia (PEI), which was preceded by isometric forearm contraction. This intervention led to an increase in sympathetic outflow in all participants. During PEI AC of the cerebral arteries proximal and at the level of the Circle of Willis significantly decreased while there was no change in AC of the distal cerebral vascular bed. There was no change in CBF_{MD}. This experiment shows the feasibility of applying our recently introduced methods of assessing cerebrovascular physiology to investigate the role of the sympathetic nervous system in regulating cerebral homeostasis. Furthermore, the differential response of the compliance of the cerebral arteries to increased sympathetic outflow shows for the first time in vivo that the large cerebral arteries increase their resistance to protect the distal vascular bed: cerebral autoregulation occurs.

7.1 Introduction

Sympathetic innervation of the cerebrovasculature

The sympathetic nervous system (SNS) controls important physiological processes in the human body and is often referred to as the ‘fight or flight’ part of the autonomic nervous system because in case of stress it is responsible for producing an ‘excited’ state, including increased blood pressure (BP) and heart rate, and dilated pupils[53]. One of the key signalling pathways of the SNS induces vasoconstriction via increased neural activity of the rostral ventrolateral medulla (RVLM)[83,131], which stimulates the release of norepinephrine, a neurotransmitter binding to α-receptors located on membranes of the vascular smooth muscle cells (SMC) in arterial walls[65,150]. Although this signalling pathway has been extensively investigated in human peripheral vasculature, such as in skeletal muscle[65,178,179], there is limited literature on in vivo sympathetic regulation of human cerebrovasculature due to the difficulty of non-invasively assessing physiological and functional parameters of the cerebral arteries and the medulla.

However, there is little doubt about the SNS being involved in regulation of the cerebrovasculature[49,68]. From early anatomic research it is known that the large cerebral arteries are extensively innervated with sympathetic perivascular nerves[48,68]. It is also known that sympathetic control is important for maintaining cerebrovascular resistance, as previous experiments have shown that when sympathetic stimulation is blocked cerebrovascular resistance decreases. For instance, after unilateral inhibition of sympathetic nerves innervating the cerebrovasculature Umeyama et al.[180] showed an increase in cerebral blood flow (CBF), measured with single photon emission computed tomography, and Ide et al.[78] showed an increase in middle cerebral artery (MCA) blood flow velocity, measured with transcranial Doppler (TCD) ultrasound. In addition, animal experiments have shown that increasing SNA by directly stimulating sympathetic nerves leads to vasoconstriction of the large cerebral arteries, including the internal carotid and middle cerebral arteries[181,182].

Cerebrovascular physiology: arterial compliance

When vasoconstriction occurs the tone of smooth muscle cells increases and compliance of the cerebral arteries decreases. Arterial compliance (AC) is also an important marker of cerebrovascular health. Compliant arteries smooth out the pulsatile blood flow originating from the heart to ensure continuous blood flow through the capillary bed of the bain[155]. Continuous blood flow within the brain parenchyma ensures optimal exchange of oxygen, nutrients and metabolites[155]. With decreasing AC, i.e. increasing arterial stiffness, blood flow within the cerebral microvasculature becomes increasingly pulsatile which can have detrimental effects. The increased pulsatile stress leads to damage of small vessel walls which can lead to severe cerebrovascular pathologies such as small vessel disease (SVD)[94,96], vascular cognitive impairment (dementia and Alzheimer’s Disease)[95] and cerebral aneurysms[183].

There are several treatments[164] aimed at increasing arterial compliance, such as exercise training[184] or anti-hypertensive drug treatment[94,185]. However, until now most of the studies assess effectiveness of treatment with measures of systemic AC, such as carotid-femoral pulse wave velocity[184] or aortic compliance[185], and improvements in cerebral AC with treatment have yet to be determined. In addition, large cohort studies have shown that early and controlled drug treatment in patients at risk of increased cerebral arterial stiffness reduces the prevalence of vascular dementia in later life, while aggressive treatment in later life can be detrimental[186]. In order to optimize treatment it is therefore of vital importance to detect decreased cerebral AC at an early stage. However, in vivo assessment of cerebral AC is difficult, due to the cerebrovasculature being imbedded within the brain impeding standard AC measurements with ultrasound techniques[170].

Cerebrovascular physiology: medullar perfusion

Sympathetic outflow is regulated in the brainstem, where the RVLM is directly responsible for up or down regulation of sympathetic nerve activity. The physiological conditions within the medulla are therefore of vital importance to maintain healthy homeostasis within the human body. Hypoperfusion of the medulla may have severe long-term consequences, in particular for blood pressure regulation as is described by *Cushing’s mechanism*[84]. In this hypothesis it is suggested that there is a 'selfish brain mechanism' in which hypoperfusion of the medulla induces increased sympathetic outflow to maintain adequate perfusion to the brainstem[84,85]. The term "Cushing's mechanism" has evolved from a wide range of experiments in animal and man coming from over a 100 years of research; Cushing himself showed in 1901 that compression of the brainstem in the ischemic brain of dogs drives up blood pressure leading to death (Cushing's *reflex*)[86], while recent human work has shown that in normotensive patients at risk of hypertension ("borderline" and "white coat" hypertensives) SNA is already elevated before they become clinically hypertensive[87]. Within the framework of Cushing's mechanism the latter is explained by the chronically increased cerebral arterial stiffness associated with hypertension, which increases cerebrovascular resistance and therefore cause hypoperfusion of the brainstem, which in turn is responsible for the increase in sympathetic outflow[84,85]. In particular, because of the presence of increased cerebrovascular resistance in patients suffering from hypertension it is suggested that Cushing's mechanism is failing, which means that despite the elevated sympathetic outflow these patients still have low perfusion of the medulla.

Currently, the link of hypoperfusion of the brainstem with elevated SNA has been established mostly through animal or in vitro experiments[88,89]. Waki et al.[88] showed that induced hypoxia of the rat medulla leads to a sympathetically mediated increase of BP. While an in vitro preparation of the brainstem and heart, including the surrounding vasculature, of neonatal pre-hypertensive spontaneously hypertensive rats showed that an increase in vascular resistance of the arteries supplying the brainstem caused an increase in sympathetic activation of the heart[89]. In vivo, human evidence for the link between medullar hypoperfusion and increased sympathetic outflow is limited due to the difficulty of measuring CBF within the human brainstem[90].

The current study

In the current study we show that with recently introduced imaging methods it is possible to investigate the effects of sympathetic outflow on the cerebrovasculature, as well as to examine physiology within the medulla. In the process of doing so, we firstly aim to demonstrate the use of our novel method of assessing cerebral arterial compliance (AC), which is a short inversion time pulsed arterial spin labelling (PASL) method that can be used to measure compliance of individual cerebral arteries (*Chapter 6*). Secondly, we aim to apply our multi inversion time PASL method optimised to assess brainstem perfusion (*Chapter 4*) to assess changes in CBF within the medulla when sympathetic nerve activity (SNA) is modulated. Here we use isometric forearm contraction (IFC) followed by post exercise ischemia (PEI) in healthy volunteers, because this intervention is well known for increasing and maintaining elevated SNA[70,81]. We hypothesize that during PEI we find a decrease in cerebral AC because of the vasoconstriction induced by elevated SNA. In addition, we hypothesize that in healthy volunteers no change in medullar perfusion occurs with the up regulated SNA during PEI because of the 'selfish brain mechanism'.

Collaboration

The *Methods* section explains the order of events in the current study in detail. However, it is mentioned here that in addition to an MRI scan session in which our novel method of AC measurement and our recently optimised brainstem perfusion method are included there was a second session outside the MRI scanner for all of our volunteers. In this session the increase in sympathetic outflow during IFC and PEI was determined by a technique called microneurography, in which muscle sympathetic nerve activity (MSNA) is directly measured from sympathetic fibres responsible for vasoconstriction. This technique requires a large amount of experience and there are currently only three researchers in the United Kingdom who are able to perform this measurement. Training in microneurography requires a minimum of 6 months and was beyond the scope of my PhD. Therefore, the microneurography data presented in this work are resulting from a collaboration between myself and Dr. Emma Hart from Bristol University, one of the experts in the technique. Dr. Hart helped me by acquiring the microneurography data and taught me how to analyse these. Data are presented here with her permission.

7.2 Methods

Eight healthy males (average age: 30.4 ± 6.4 years) were recruited for the PEI experiment. Imaging data were acquired on a 3 T whole body MRI system (GE Excite HDx, Milwaukee, WI) using an eight-channel receive-only head coil. Informed consent was obtained from all volunteers under ethical approval from the Cardiff University School of Psychology Ethics

Committee and all experiments were performed in accordance with the guidelines stated in the Cardiff University Research Framework (version 4.0, 2010).

Each participant underwent two sessions, one MSNA session and one MRI session to measure AC and CBF. There was one participant for which the MSNA session was unsuccessful and another participant for which there is no CBF measurement because he was not comfortable with proceeding. Therefore there are seven datasets for the MSNA measurements of PEI, and eight datasets for the MRI measurement of AC.

Post exercise ischemia (PEI)

The PEI protocol was similar to that previously described by Sander et al.[81]. A pneumatic in-house made and MRI compatible handgrip device was used. Participants were first asked to use their dominant hand (all were right handed) to perform their maximum effort handgrip twice, each time holding for 2 seconds. During the task each participant was instructed via visual cues to do an isometric forearm contraction (IFC) at 40% of his maximum grip for 3 minutes. After 2 minutes of IFC a brachial blood pressure cuff, placed ipsilateral to the gripping hand, was inflated to 100 mmHg above resting systolic BP. The blood pressure cuff was inflated for 10 minutes. Note that this meant that there was 1 min of overlap of IFC and cuff inflation. The total duration of this PEI protocol was 12 minutes. A timeline of this protocol can be seen in Figure 7.1.

Arterial compliance measurements

The MRI scan session contained four main scan series, two measurements of AC and two measurements of CBF. For both measurements (AC and CBF) there was one resting scan series, in which participants were instructed to look at a cross-hair for the duration of the scan, and one series preceded by the IFC task, and scanned in the following 10 minutes of PEI (see Figure 7.1).

The AC measurement was performed as described previously (Chapter 6). Short inversion time (TI) pulsed ASL was used with seven TIs: 250 – 850 ms, with spacing of 100 ms. PICORE

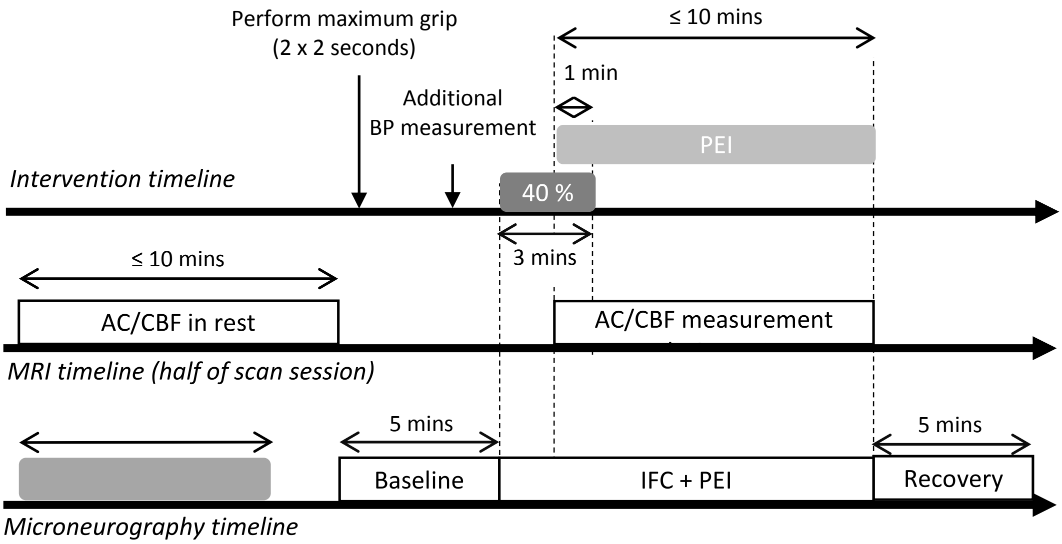

Figure 7.1. Timelines of experiment. The top row shows the timing of the intervention. Participants performed their maximum grip to determine 40% of their maximum grip for the 3 minute long IFC. The BP measurement was done with the same MRI compatible brachial blood pressure cuff which is later used to induce PEI. Participants were instructed to perform the handgrip task with their dominant hand. There was 1 minute of overlap between the IFC and inflation of the brachial BP cuff (at 100 mmHg above resting systolic BP). PEI lasted for maximum 9 more minutes. The middle timeline shows the events in the MRI scanner. The resting measurement of AC or CBF was performed before the handgrip task. Note that for each participant the AC measurements were first, but that the same protocol was repeated for the CBF measurement afterwards. The bottom line shows the microneurography measurement. Locating the peroneal nerve lasted for maximum 60 minutes. After the peroneal nerve was located, MSNA was measured for 22 minutes (containing baseline, IFC, PEI and recovery periods). *BP = blood pressure, IFC = isometric forearm contraction, PEI = post exercise ischaemia, AC = arterial compliance, CBF = cerebral blood flow.*

tagging was applied with label thickness of 200mm and a QUIPSS II[187] cut-off at 700 ms, so for the acquisitions with TI = 750 ms and TI = 850 ms, and 32 tag-control pairs were acquired for each TI. The gap between the distal end of the labelling slab and the most proximal slice was 1 mm. A gradient echo spiral read-out with a single interleaf was used. Other acquisition parameters were: variable repetition time (TR), minimum TR = 1 s, TE = 2.7 ms, voxel size = 3.5x3.5x7 mm^3, 12 slices, slice gap 1 mm, slice delay 29 ms.

A calibration image was acquired with the same acquisition parameters, except for the repetition time (TR = 4s) and without applying a labelling pulse, in order to obtain the equilibrium magnetisation of cerebrospinal fluid ($M_{0,\ CSF}$).

Physiological monitoring

Blood pressure (BP) was measured continuously with a photoplethysmograph finger cuff on the left thumb (BIOPAC Systems, Goleta, USA). Mean arterial pressure (MAP) was calculated as follows: MAP = $(1/3)*BP_{Sys} + (2/3)*BP_{Dia}$ and pulse pressure (PP) was calculated as the difference between systolic and diastolic blood pressure ($PP = BP_{Sys} - BP_{Dia}$). Average MAP and PP were calculated for the durations of the AC scans in rest and PEI. Finger photoplethysmography was used to measure cardiac traces, a pneumatic belt just below the rib cage was used to monitor respiratory rate and a nasal cannula to monitor end-tidal partial pressures of carbon dioxide ($P_{ET_{CO_2}}$) and oxygen ($P_{ET_{O_2}}$).

Image analysis

PASL time series were motion corrected using *mcflirt* within the FMRIB Software Library v5.0 (FSL-http://fsl.fmrib.ox.ac.uk)[115]. Retrospective synchronisation was then performed using in-house programmes written in MATLAB R2012b (Mathworks, Natick, MA, USA). A time shift of 225 ms was applied to the finger plethysmograph trace to account for the delay between the cerebral and finger pulse. This time period was deduced from the delay time between the R-peak in the electrocardiogram and the left finger[188] and the time delay between R-peak in the ECG and the onset of the carotid pulse wave[172]. Images were further analysed on slice-by-slice basis, taking into account the slice time delay. The normalized cardiac phase ($\varphi_{c,norm}$) of each acquired slice was determined according the following:

$$\varphi_{c,norm} = (t_{acq} - t_1)/(t_2 - t_1) \qquad \text{Eq. 7.1}$$

where t_{acq} is the time of the slice acquisition, t_1 the time of the previous systolic peak in the shifted plethysmography trace and t_2 the time of the following systolic peak in the plethysmography trace. The cardiac cycle was then divided into 6 bins, i.e. the first bin containing slices acquired with $0 \leq \varphi_{c,norm} < 1/6$, the second bin containing slices acquired with $2/6 \leq \varphi_{c,norm} < 3/6$ and so on. Slices acquired in “early diastole” corresponded to those with $1/6 \leq \varphi_{c,norm} \leq 2/6$ and slices acquired in “early systole” were those with $4/6 \leq \varphi_{c,norm} \leq$

5/6. Average tag and control images were calculated and subtracted to obtain maps of ΔM for each of the 6 cardiac phases at each of the 7 TIs.

Calculation of compliance related parameter maps

We used Eq. 7.2 to estimate aBV, Δt_{art}, and σ on a voxelwise basis for each of the 6 cardiac phases separately (least-square fitting, *lsqcurvefit* in MATLAB):

$$\Delta M(t) = \begin{cases} 0 & 0 < \Delta t_{art} \\ 2\alpha M_{0,a} e^{-\frac{1}{T_{1a}}} aBV[w(t) * \mu(\sigma, t)] & \Delta t_{art} \leq t \leq \Delta t_{art} + \tau \\ 0 & \Delta t_{art} + \tau < t \end{cases} \qquad \text{Eq. 7.2}$$

The bolus duration (τ) was fixed at 700 ms by the QUIPSS II cut-off, the *w(t)* was a square weighting function (1 for $t < \tau$, 0 elsewhere), and *μ(σ,t)* a Gaussian kernel with width σ and centered on Δt_{art}. A full description of this model can be found in Chapter 6. Maps of aBV_{Dia} (from images acquired in “early diastole”) and aBV_{Sys} (calculated from images acquired in “early systole”) were used to calculate arterial compliance (AC) according to:

$$AC = 100\% \cdot \frac{aBV_{Sys} - aBV_{Dia}}{aBV_{Dia} \cdot (BP_{Sys} - BP_{Dia})} \qquad \text{Eq. 7.3}$$

Note that here AC is normalized for the arterial blood volume in diastole and is therefore calculated as percentage change in aBV per mmHg (%/mmHg).

Regions of interest

For each participant regions of interest (ROI) were determined based on an *average* aBV map: a map of aBV resulting from fitting Eq. 7.2 to an average ΔM image containing the tag-control data for all TIs and all cardiac phases (no synchronization with cardiac phase!). For instance, in the slice just above the Circle of Willis these regions were drawn to encompass the flow territories of the right middle, left middle, right posterior, left posterior and anterior cerebral arteries (RMCA, LMCA, RPCA, LPCA, and ACA). These manually drawn ROIs were multiplied with the thresholded average aBV map ($aBV \geq 0.5\ \%_v$) to create individual ROIs of each artery. Note that ROIs were created for average aBV maps from both the *Rest* and *PEI* AC time series. For each flow territory, the union of the ROIs resulting from the *Rest* and *PEI* data was used for the region based analysis (see Figure 7.2).

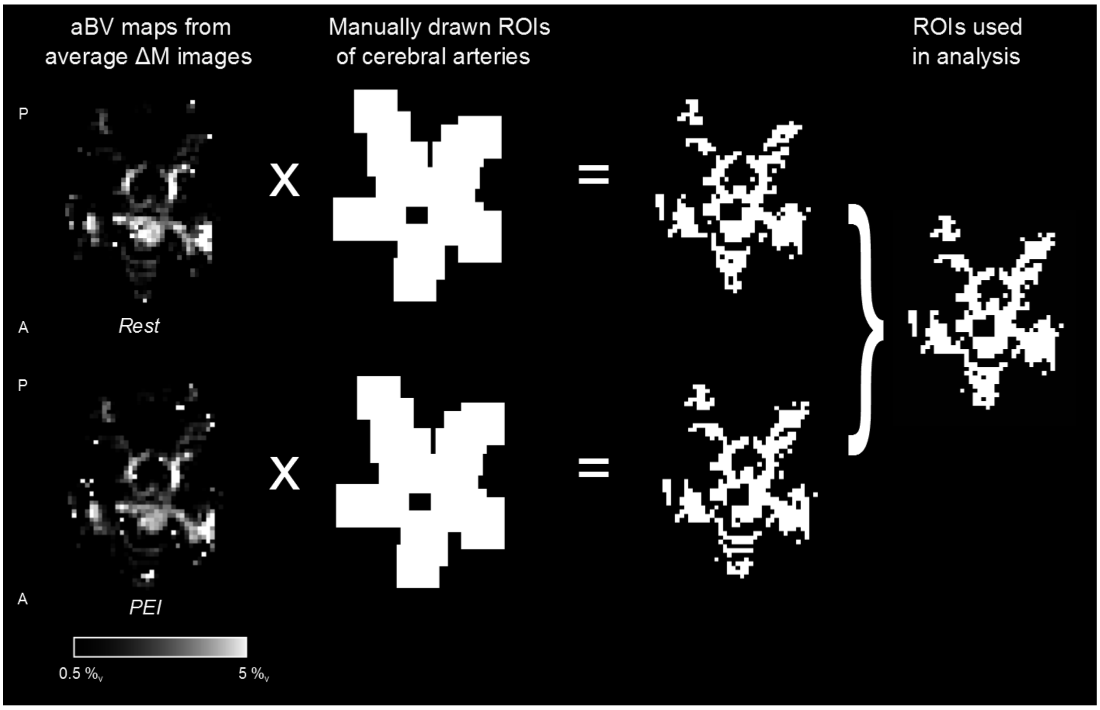

Figure 7.2. Example of ROIs used in the analysis of the PEI data. First, aBV maps were created by fitting the arterial input function to all the ΔM data (no synchronisation to the cardiac cycle is performed) for both the AC measurements (*Rest* and *PEI*). Broad ROIs were drawn manually to encompass all of the flow territories of the individual arteries (note that there are five individual territories; RMCA, LMCA, ACA, RPCA, and LPCA). These manually drawn ROIs were multiplied with the thresholded aBV maps (aBV ≥ 0.5 $\%_v$) to create individual ROIs of each artery, in *Rest* and during *PEI*. For each flow territory, the union of the ROIs resulting from the *Rest* and *PEI* data was used for the region based analysis. *A = anterior, P = posterior.*

Perfusion measurement and image analysis

CBF measurement was done with multi inversion time pulsed ASL, optimised for brainstem imaging[132]. PICORE labelling with label thickness of 200 mm and a QUIPSSII cut-off at 700 ms[187] was used and ten tag-control pairs were acquired for each of 8 TIs (250 ms, 400 ms, 550 ms, 700 ms, 1000 ms, 1300 ms, 1600 ms, 1900 ms). A gradient echo image acquisition was performed with two spiral interleaves, to minimise signal loss due to field inhomogeneities and physiological noise. Other acquisition parameters were: variable repetition time (TR), minimum TR = 1 s, TE = 2.7 ms, voxel size = 3.5x3.5x7 mm^3, 12 slices, slice gap 1 mm. Total acquisition time was approximately 10 minutes.

The CBF time series were motion corrected (mcflirt within the FSL toolbox v5.0, http://fsl.fmrib.ox.ac.uk). Edge-preserving smoothing was applied to the minimal contrast image (SUSAN[116], within FSL) and the result was used to correct the CBF time series for the coil sensitivity profile, i.e. the CBF time series was divided by the pre-processed minimal contrast image. Average difference images (ΔM) were obtained for each inversion time after tag-control subtraction of the CBF time series. Chappell's two-compartment model, containing both a macro- and microvascular compartment[26], was then used to fit the kinetic curve of the magnetic label on a voxel-by-voxel basis. Chappell's model is described as follows:

$$\Delta M(t) = \Delta M_{tiss}(t, CBF, \Delta t_{tiss}) + \Delta M_{art}(t, aBV, \Delta t_{art}) \qquad \text{Eq. 7.4}$$

Note that in addition to CBF in ml/100 g/min, this model also results in estimates of the arterial blood volume (aBV) in volume percentage of the voxel ($\%_v$), arrival time of the labelled bolus in the macrovasculature (Δt_{art}) in ms and arrival time of the labelled bolus in the microvasculature (Δt_{tiss}) in ms. The reader is referred to work of Chappell et al.[26] for a full description of the model.

Masks of whole brain grey matter (GM) were created from the T_1-weighted structural scan with *FAST* (available within FSL). In order to obtain masks of the brainstem linear registrations were performed with *FLIRT* (available within FSL) to register each subject's CSF image to the Montreal Neurological Institute (MNI) standard space, via the T_1-weighted structural scan. The transformation matrices resulting from these registration were concatenated and inverted to obtain the transformation matrix for the registration from MNI standard space to subject space. The latter transformation matrix was used to register the mask of the brainstem, available within the Harvard-Oxford Subcortical Atlas in FSL, to subject space. The brainstem mask was subdivided into the medulla (MNI standard space: $Z \leq 13$), pons (MNI standard space: $14 \leq Z \leq 24$), and midbrain (MNI standard space: $Z \geq 24$) to calculate CBF, aBV, Δt_{tiss}, and Δt_{art} for these regions individually.

Statistics

In order to determine differences in AC or CBF during PEI we performed two separate two-way repeated measures ANOVA (RM-ANOVA). Each analysis had two independent factors: *physiological state* (rest versus PEI) and *ROI*. In the RM-ANOVA regarding the AC data the independent factor *ROI* contained the five flow territories: RMCA, LMCA, ACA, RPCA, and

LPCA. In the RM-ANOVA regarding the CBF data the independent factor *ROI* contained five brain regions: the medulla, pons, midbrain, brainstem and grey matter. Unless stated otherwise data is presented here as *average ± standard error of the mean* (SEM).

Quantification of head motion

Head motion was quantified to analyse the effect that PEI had on the quality of the PASL data. The amount of head motion induced by the PEI was quantified based on previously described methods[189]. The reference image used by *mcflirt* was the middle image of the time series. For each image *i* the norm of the translation (T_{Norm}) with respect to the reference image was calculated as follows:

$$T_{Norm} = \sqrt{dS_i^2 + dL_i^2 + dP_i^2} \qquad \text{Eq. 7.5}$$

The translation parameters are corresponding to movement in the superior (dS), left (dL) and posterior direction (all in mm). The median of T_{Norm} for each time series was used to investigate differences between rest and PEI in gross head motion for both AC and CBF measurements. Note that there were two separate t-tests performed for the AC and CBF because of the different number of participants for each scan (one participant did not complete the CBF measurement).

Microneurography

Seven out of eight participants also underwent a successful microneurography session to measure muscle sympathetic nerve activity (MSNA). In this technique microelectrodes are inserted directly into sympathetic nerves of muscles such that multiunit discharges within these fibres can be measured[190]. MSNA was measured from the peroneal nerve of the right leg during 5 minutes of baseline, the IFC and PEI (12 minutes), and a 5 minute recovery period (see Figure 7.1). The microneurography measurement was performed by Dr. Emma Hart from Bristol University, who is one of three experts in this technique in the United Kingdom. Physiological monitoring was the same as during the MRI scan session, except no respiratory belt to measure respiratory rate or nasal cannula to measure end-tidal gas concentrations was used.

MSNA was measured according to methods described previously[191,192]: participants were in supine position with a foam pad under their right thigh and MSNA was recorded from the right peroneal nerve at the fibular head using insulated tungsten microelectrodes connected to an amplifier (NeuroAmp Ex, ADInstruments, Bella Vista, Australia). A muscle sympathetic fascicle was identified when taps on the muscle belly or passive muscle stretch evoked mechanoreceptive impulses, and no afferent neural response was evoked by skin stimuli. The recorded signal was amplified 80000-fold, band-pass filtered (700 to 5000 Hz), rectified, and integrated (resistance-capacitance integrator circuit time constant 0.1 s) by a nerve traffic analyser (PowerLab 8/35, ADInstruments, Bella Vista, Australia). MSNA data was recorded with LabChart 7 (ADInstruments, Bella Vista, Australia) and analysed with in-house written scripts (Spike 2, Cambridge Electronic Design, Cambridge, United Kingdom) to yield burst frequency (bursts/100 heartbeats).

7.3 Results

Figure 7.3 contains results of the main physiological parameters measured during the microneurography session (N = 7). It can be seen that the IFC lead to a steep increase in heart rate, which reduced as soon as the IFC was stopped, but did not return to baseline until the end of the PEI. It can be seen that blood pressure increased during the IFC and remained elevated throughout the PEI period, as illustrated by the elevated MAP and PP. MSNA, as measured by bursts/100 beats showed a steady increase during both the IFC and PEI, peaking at the end of PEI period.

Group average physiological parameters during the MRI scan session are stated in Table 7.1, where it can be seen that although on average blood pressure increased during PEI, significant increases in systolic and diastolic BP, and MAP were only found during the AC measurement (paired t-test, $p < 0.05$).

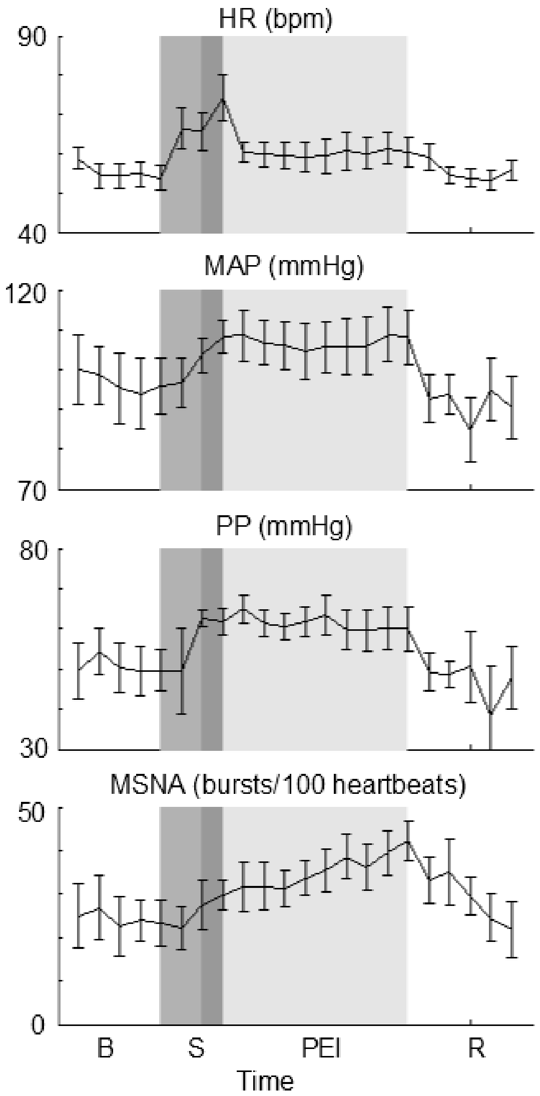

Figure 7.3. Group average data (N=7) resulting from the MSNA sessions. In each of the sessions there was a baseline recording (of at least 3 mins), followed by a 3 minute period of IFC at 40 % (middle grey), and a 10 minute period of PEI (lightest grey). Note that there was 1 minute of overlap (dark grey) between the IFC and occlusion of the brachial blood pressure cuff that caused the PEI. It can be seen that heart rate (HR), mean arterial pressure (MAP), and pulse pressure (PP) increased during the IFC. While PEI maintained elevated blood pressure, the heart rate decreased immediately after termination of the IFC task. In the bottom graph it can be seen that MSNA shows a steady increase from baseline to a maximum at the end of PEI.

Table 7.1. Relevant physiological parameters *(average ± standard deviation)* for the rest and PEI periods during acquisition of the AC, CBF, and microneurography measurements. Note that there was one participant that withdrew after the AC measurement and one participant for which no microneurography was performed. All measurements were done continuously throughout the scan session, note that all average values stated here are calculated for a time period of approximately 10 minutes (for the duration of each scan).

	Arterial compliance (N=8)		*Cerebral blood flow (N=7)*		*Microneurography (N=7)*	
	Rest	PEI	Rest	PEI	Rest	PEI
BP_{Sys} (mmHg)	126.4 ± 9.5	134.9 ± 11.0*	132.1 ± 10.1	135.1 ± 16.1	130.8 ± 22.6	147.8 ± 19.8
BP_{Dia} (mmHg)	68.3 ± 9.3	77.9 ± 12.1*	71.7 ± 8.1	76.9 ± 15.0	79.6 ± 13.9	86.2 ± 15.5
PP (mmHg)	58.1 ± 6.7	57.0 ± 6.8	60.4 ± 7.1	58.2 ± 9.0	51.4 ± 11.7	61.3 ± 10.4
MAP (mmHg)	87.7 ± 8.9	96.9 ± 11.3*	91.8 ± 8.3	96.3 ± 14.8	96.8 ± 16.6	106.8 ± 16.2
Heart rate (beats/min)	58.7 ± 11.5	62.6 ± 12.6	56.3 ± 9.2	62.6 ± 11.3*	53.3 ± 8.7	61.5 ± 11.2*
Breathing rate (breaths/min)	16.4 ± 4.3	16.1 ± 5.6	16.6 ± 3.0	15.0 ± 5.6	-	-
P_{ETCO_2} (mmHg)	38.1 ± 5.3	35.6 ± 5.6	35.5 ± 5.1	31.9 ± 4.8*	-	-

** Significantly different (paired t-test, $p < 0.05$), - No monitoring of respiratory parameters during microneurography session*

During PEI there was an overall decrease in aBV, as illustrated by Figure 7.4. In addition, AC for the middle cerebral arteries decreased on average by approximately 50 %, for the ACA this was 30 %, while compliance of the posterior arteries seemed to decrease by more than 80 % during PEI (illustrated by Figure 7.5). The overall decrease in AC during PEI was significant (RM-ANOVA, F(1,7) = 20.7, $p < 0.01$). However, there was no significant difference between ROIs (RM-ANOVA, F(4,28) = 1.6, p = 0.23). Example AC maps are plotted in Figure 7.6.

When averaging AC together for the flow territories below the circle of Willis (CoW), encompassing the internal carotid and basilar arteries, and the RMCA and LMCA it can be seen that on average the larger, proximal arteries show a decrease in AC during PEI while more distal flow territories do not show a decrease in AC during PEI (see Figure 7.7). Slice by slice comparison of AC during rest and PEI showed that only for the slice with the CoW and slice CoW – 3 the decrease in AC was significant (paired t-test, $p < 0.03$).

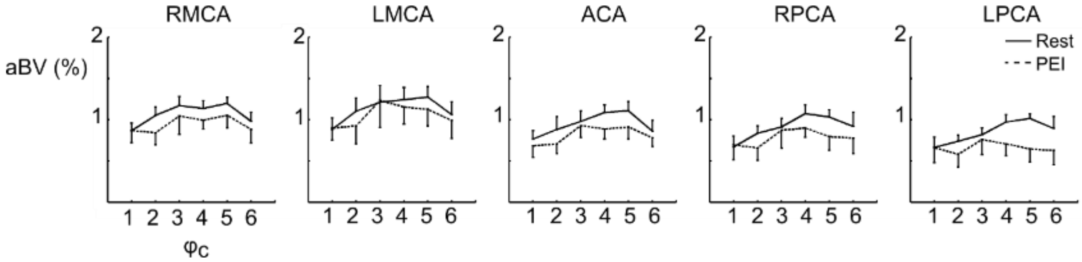

Figure 7.4. Fitted aBV (%$_v$) per cardiac phase (φ_c) resulting from the AC measurement. Group average values (N =8) are shown for the flow territories in a single slice just above the Circle of Willis, containing the M1 segment of the MCAs. During PEI aBV was particularly lower during systole ($\varphi_c = 5$), while there was no decrease in aBV during diastole ($\varphi_c = 1$), indicating that PEI is related to a decrease in AC by affecting the aBV at higher BP (note that $BP_{Sys} > BP_{Dia}$). *Error bars indicate SEM. aBV = arterial blood volume, RMCA = right middle cerebral artery, LMCA = left middle cerebral artery, ACA = anterior cerebral artery, RPCA = right posterior cerebral artery, LPCA = left posterior cerebral artery, PEI = post exercise ischemia.*

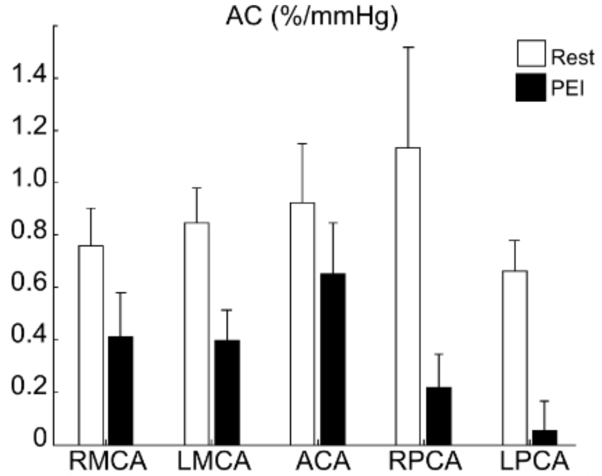

Figure 7.5. Group average (N=8) AC for the middle, posterior and anterior arteries branching from the Circle of Willis in rest and during PEI. It can be seen that during PEI AC decreases in all five flow territories (RM-ANOVA, $F(1,7) = 20.7$, $p < 0.01$). However, there was no significant difference between flow territories. *Error bars indicate SEM. AC = arterial compliance, RMCA & LMCA = right and left middle cerebral arteries, ACA = anterior cerebral artery, RPCA & LPCA = right and left posterior cerebral artery.*

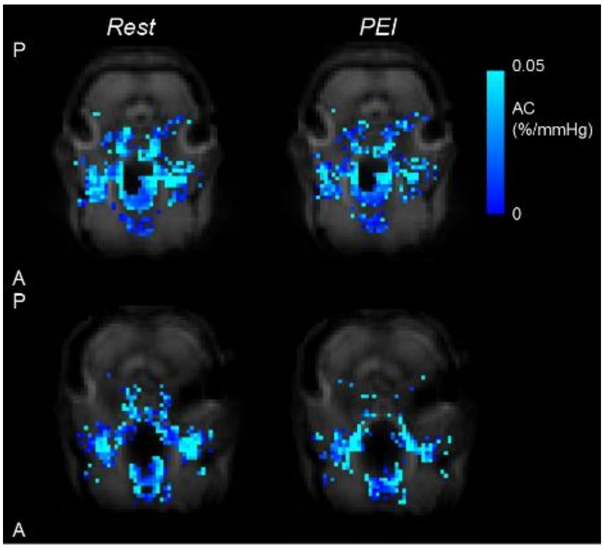

Figure 7.6. Example of AC maps in *Rest* and during *PEI*, each row represent a subject. Note that the AC maps are masked with the ROIs as defined by the average aBV images (see Methods section for details of ROI formation). In addition, the maps are thresholded to show voxels with positive AC. It can be seen that in both subjects AC decreases during PEI, but also that the amount of voxels with positive AC decreases during PEI. Increased head motion is the likely cause for the latter, particularly illustrated by the second subject (bottom row), where the compliance of the posterior arteries appears to decrease below zero during PEI. *A = anterior, P = posterior.*

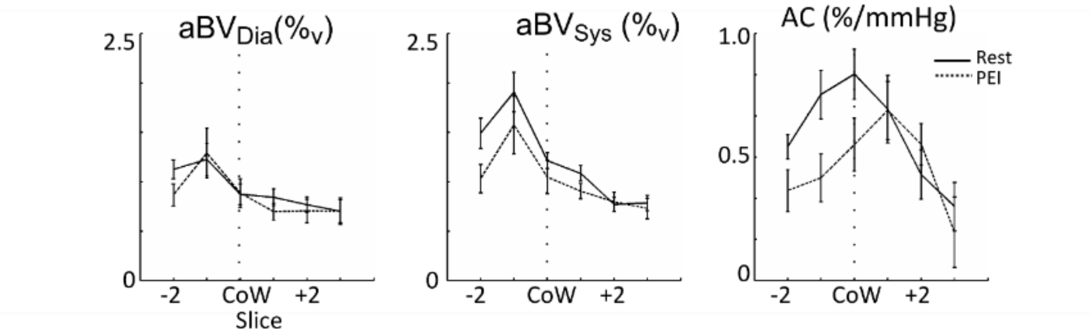

Figure 7.7. Group average aBV_{Dia}, aBV_{Sys}, and AC plotted against slice location, from 2 slices below to 3 slices above the CoW (slice with the M1 segment of the MCA). Note that the data is averaged over the flow territories of the major brain feeding arteries below the Circle of Willis (internal carotid and basilar/vertebral arteries) and both RMCA and LMCA above the CoW. Although none of the flow territories show a change in aBV_{Dia}, the larger and more proximal arteries show a decrease in aBV_{Sys} during PEI. Note that this leads to the figure on the right, where it can be seen that the arteries below and at the level of the CoW show a decrease in AC during PEI, while the MCA flow territories more distal from the CoW show no decrease in AC during PEI. *Error bars indicate SEM. AC = Arterial compliance, PEI = Post exercise ischemia, CoW = Circle of Willis.*

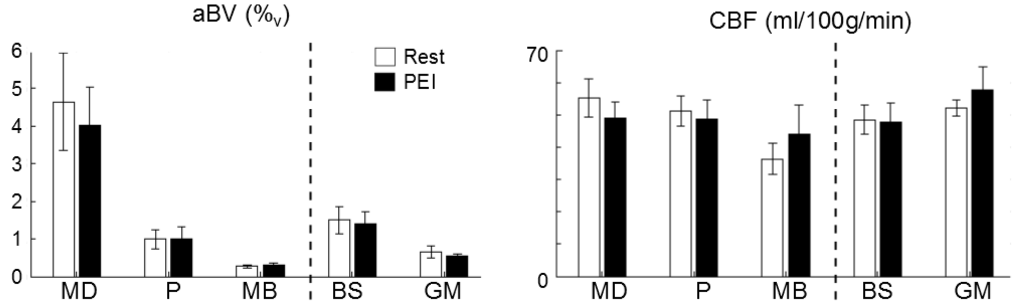

Figure 7.8. Group average aBV and CBF per ROI (N=7). RM-ANOVA's showed no significant effect of Rest vs PEI for CBF (F(1,6)=0.03, p=0.89) and aBV (F(1,6)=0.454, p = 0.53). However, as expected the MD had the highest aBV from all ROIs, while during both Rest and PEI periods the medulla and the midbrain had significantly different CBF. (And the midbrain had significantly lower CBF than the GM). *Error bars indicate standard error of the mean. PEI = post exercise ischemia, MD = Medulla, P = Pons, MB = Midbrain, BS = Brainstem, GM = Grey matter.*

Group average values of aBV and CBF for the different ROIs can be seen in Figure 7.8. Neither aBV or CBF resulting from the perfusion measurement was significantly influenced by PEI, as shown by RM-ANOVA (aBV: F(1,6) = 0.45, p = 0.53, CBF: F(1,6) = 0.02, p = 0.89), nor were there significant interactions between *physiogloical state* and *ROI* (aBV: F(4,24) = 1.07, p= 0.40, CBF: F(4,24) = 2.16, p = 0.11). However, there were significant differences in hemodynamic parameters between ROIs (aBV: F(4,24) = 11.6, p < 0.001, and CBF: F(4,24) = 5.11, p < 0.01). Post-hoc paired t-tests showed that the MD had the largest aBV of all ROIs and that the CBF_{MD} was significantly higher than CBF_{MB} (paired t-test, p <0.05).

Although on average there was an increase in head motion, over all participants (N = 8 for the AC measurement, N = 7 for the CBF measurement) this increase was not significant (paired t-tests, AC: p = 0.55, CBF: p = 0.35). As can be seen in Figure 7.9, in 6 out of 15 sessions participants had a decrease in head motion during PEI.

7.4 Discussion

In this study it has been shown that the novel method of non-invasive measurement of AC (*Chapter 6*) is able to measure decreases in compliance of individual cerebral arteries caused by an intervention that elevates sympathetic outflow. In addition to demonstrating the use of our novel method of AC, this study included the application of a brainstem optimised

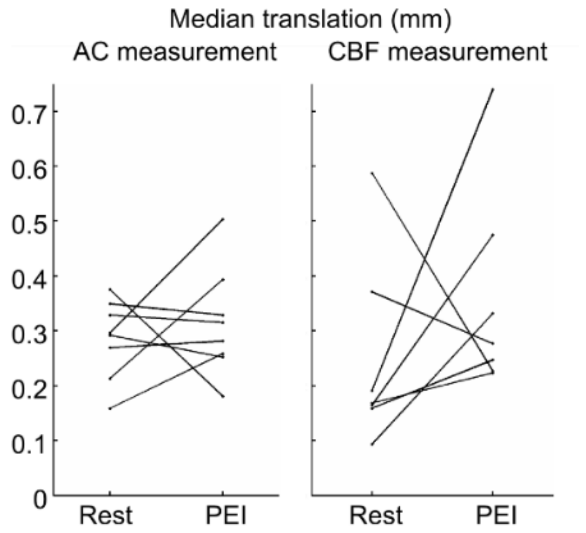

Figure 7.9. Head motion in rest and during PEI, for both the AC and CBF measurements. Each line represents the median of T_{norm} for a single participant. Note that N=8 for AC, and N=7 for CBF. Paired t-tests show no significant differences in head motion between rest and PEI (AC: p = 0.55, CBF: p = 0.35). Note however, that the amount of head motion is very variable across participants. Head motion is detrimental for the AC measurement, as illustrated by the participant with the largest head motion during PEI (for whom the AC maps are shown in the bottom row in Figure 7.6). *AC = arterial compliance, CBF = cerebral blood flow, PEI = post exercise ischemia.*

protocol of PASL perfusion measurement (*Chapter 4*) to investigate medullar physiology. No significant differences were found in perfusion or arterial blood volume due to increased sympathetic nerve activity during post exercise ischemia.

Arterial compliance

AC of the cerebral arteries at the level of the CoW shows a significant decrease during PEI, as is illustrated by Figure 7.5. The decrease in compliance is likely caused by an increase in smooth muscle cell (SMC) tone within the vessel walls, which causes vasoconstriction. However, as can be seen in Figure 7.4, it is mainly aBV_{Sys} that is affected by the increase in SMC tone and no change of aBV_{Dia} occurs. This result may be explained by the fact that mechanic properties of arterial walls are dependent on three tissues: collagen, elastin and smooth muscle cells[61,178]. When it comes to distending the arterial wall, collagen and elastin are the passive components and the SMC are the active or contractile components. Bank et al.[178,179] measured the contribution of each of the individual components to the stiffness of the human brachial artery at different levels of intra-arterial pressure and smooth muscle tone. Their results showed that at lower transmural pressure (i.e. 70 mmHg) an increase in SMC tone does not change the mechanical properties of the arterial wall, but changes the relative contributions of the three components to the wall stiffness. The contribution of SMC to the stiffness of the arterial wall becomes larger and the contribution of collagen decreases. However, at higher transmural pressure (i.e. 100 mmHg) an increase in SMC tone also increases arterial wall stiffness[179], which would explain why here we find no changes in aBV_{Dia} and a decrease in aBV_{Sys} during PEI (Figure 7.4 and Figure 7.7).

It is likely that the decrease in AC is caused by the significant increase in sympathetic outflow during PEI, as illustrated by the increase in MSNA in this study (Figure 7.3, bottom image)[48,49,179]. Vasoconstriction within the cerebral arteries then is caused by the release of norepinephrine, a potent vasoconstrictor[150]. However, it must be noted here that during the AC measurement in PEI there also was a significant increase in blood pressure, as shown by the significant increases in BP_{Sys} and BP_{Dia} (see Table 7.1). From ex-vivo experiments it is known that in the absence of sympathetic stimulation, SMC also show a myogenic response: the contraction mechanism of the muscle cells is activated by stretch induced by elevated BP[62,65]. The following paragraphs discuss whether here it is the increase in sympathetic outflow or the increase in BP that caused the decrease in AC of the arteries below and at the level of CoW during PEI.

The fact that more distal smaller cerebral arteries are unaffected during PEI while there is a decrease in AC in the larger cerebral arteries may be explained by the decrease in sympathetic perivascular stimulation along the cerebral vascular tree. From ex vivo and animal experiments it is known that perivascular sympathetic nerves are surrounding the basal cerebral arteries but their density decreases along the cerebrovascular tree, such that parenchymal arterioles are not innervated by the sympathetic nervous system at all[48,49,51,182,193,194]. Furthermore, in rats Cipolla et al.[182] demonstrated that the difference in sensitivity to sympathetic stimulation lies in the presence of norepinephrine α1-receptors on the surface of SMC; while these receptors are abundant in SMC of the proximal MCA, SMC in the walls of pial arteries branching from the MCA contain progressively less of these vasoconstriction related receptors. In addition, Baumbach et al.[195] showed that in rabbits and cats only basal cerebral arteries show a marked vasoconstriction with an increase in sympathetic stimulation. In their experiment Baumbach et al. controlled for potential myogenic responses from the SMC by directly stimulating sympathetic nerves such that there was no change in systemic blood pressure. Although human equivalents of these animal experiments are non-existent for obvious reasons, the results of these studies combined with presence of sympathetic perivascular nerves make it plausible that the elevated sympathetic outflow in the current PEI experiment, at least in part, is causing the decrease in AC in the larger cerebral arteries.

Myogenic vasoconstriction due to an increase in blood pressure may be ruled out because there are no changes in aBV_{Sys}, and therefore no changes in AC, in the distal slices (Figure 7.7). Although these slices do contain smaller arteries and arterioles, their vessel walls still contain SMC because these cells only completely disappear from the vessel walls in the capillaries within the brain parenchyma[47]. In addition, the MAP increase during PEI in the current experiment is only 10 mmHg. Osol et al.[196] showed in vitro that when transmural pressure ranged from 60 to 140 mmHg in the absence of sympathetic stimulation there were only minor changes in rat PCA diameter (although wall tension did show a related increase). Osol's results suggest that the increase in BP in the current experiment may not be sufficient to cause marked vasoconstriction in the cerebral arteries. However, translating in vitro experiments on animal cerebral arteries to in vivo human data is difficult, not only because of the differences in sympathetic signalling pathways between species[49] but also because the variety of signalling pathways that can influence SMC tone[62,194].

The fact that the large cerebral arteries constrict indicates that cerebral autoregulation has taken place: as a response to elevated BP proximal cerebral arteries increase their resistance to protect the distal cerebrovasculature from the increase in systemic BP[68]. It is possible that because of cerebral autoregulation there is no change in mean arterial pressure in the arteries and arterioles distal to the circle of Willis, despite the increase in systemic MAP. As a result, myogenic increase of SMC tone cannot be ruled out because the SMC of the distal vasculature are not stretched due to increased pressure. The current experiment therefore renders it impossible to exclude myogenic vasoconstriction as a cause for the elevated SMC tone.

Even in the absence of a conclusive explanation for the elevated SMC tone, this experiment still contains the first *in vivo* measurement of the differential response of human cerebrovasculature to PEI. In order to investigate the role of the SNS in the cerebral circulation a control experiment is necessary in which sympathetic outflow is altered without an increase in BP. This could be an experiment in which low doses of vasoactive drugs (i.e. norepinephrine or nitro-glycerine[178,197]) are used, such that no changes in systemic blood pressure are present. Another option would be inducing orthostatic stress by using a lower body negative pressure chamber, as this stimulus is known to elevate peripheral muscle sympathetic nerve activity without changing systemic mean arterial pressure[198]. However, the current experiment has shown that the novel AC measurement is able to assess changes in cerebral AC and it is therefore recommended to be included in any experiment investigating sympathetic regulation of the cerebrovasculature.

Medullar perfusion and Cushing's mechanism

In healthy volunteers *Cushing's mechanism*[84] should result in no change in CBF_{MD} during PEI, despite the elevation in sympathetic outflow and blood pressure that accompanies exercise. Finding no significant differences in perfusion between PEI and rest here is therefore as expected. To the best of our knowledge this is the first experiment directly measuring human CBF_{MD} during rest and PEI and it shows the potential of using our method to investigate the relationship between sympathetic nerve activity and perfusion within the medulla.

Cushing's mechanism has been introduced in the context of research into the mechanisms of essential hypertension (hypertension without a clear cause)[84]. It is postulated that in essential hypertensive patients decreased perfusion of the medulla leads to an increase in BP, via elevated sympathetic outflow regulated by nuclei within the medulla. A common comorbidity in hypertension is increased arterial stiffness, which also affects the vertebral and basilar arteries. In the framework of Cushing's mechanism it is the decrease in compliance in the vertebro-basilar circuit that causes hypoperfusion of the medulla. It is then hypothesized that, in contrast to healthy people, hypertensives will have lower perfusion of the medulla and elevated sympathetic nerve activity in rest because the 'selfish brain mechanism' is unable to maintain CBF_{MD} because of the increased cerebrovascular resistance to the brainstem. The fact that hypertension is associated with increased arterial stiffness of cerebral arteries as well is an aspect known mainly from animal models (i.e. untreated spontaneous hypertensive rats) in which hypertension leads to hypertrophy of cerebral arterial walls and decreases in lumen diameters[194]. The combination of our novel methods that measure cerebral AC and are able to assess CBF_{MD} might therefore offer insight in the cerebrovasculature, and the regulation thereof, in patients with essential hypertension in future investigations.

Another interesting aspect of using our novel methods to image the cerebrovascular physiology is to investigate the mechanisms behind Cushing's mechanism. Although it is hypothesized that it is hypoperfusion of the medulla that drives the increase in SNA, it is important to note that the exact mechanisms behind this regulatory process are still unknown[85]. Some hypothesize that it is the decrease in oxygen delivery to the brainstem that triggers the increase in sympathetic outflow and causes the increase BP to be maintained[88]. Other studies have suggested activation of the medulla via pressure induced changes within the brain, either via a currently unknown intra-cranial baroreceptor[199] or due to a signalling pathway activated by changes in stretch of the vertebral or basilar arterial walls[200]. Our results do suggest that with an increase in BP there is vasoconstriction of the basilar artery (reduced aBV_{MD}, Figure 7.8), but more research is necessary to investigate whether it is this vasoconstriction that drives the increased SNA or whether it is only a consequence of the increased sympathetic outflow.

Other applications of the novel AC measurement

In the classical view of cerebral autoregulation it is postulated that it is mainly at the level of the smaller cerebral arteries where cerebrovascular resistance is altered to maintain constant CBF to the brain parenchyma over a range of MAP, because the larger cerebral arteries were assumed to be rigid[68]. However, ever since animal experiments revealed that the larger brain arteries show capacitive behaviour that can be influenced by changes in blood pressure or sympathetic stimulation[181,193,195] there is a growing body of evidence suggesting that the larger cerebral arteries are actually the site of cerebrovascular resistance regulation in humans as well[68,77,160]. Interestingly, in humans this evidence mainly consists of indirect measurements of cerebral arterial compliance based on transcranial Doppler assessments of the MCA or PCA[160,169] or on the analysis of blood flow patterns within the internal and vertebral arteries[201]. Our results in Figure 7.7 are the first to show the differential response within the cerebrovascular tree during a physiological challenge and confirm that it is within the larger brain arteries that cerebrovascular resistance changes during PEI while vascular properties of the arteries distal to the CoW are maintained. These results suggest that our novel method could be a valuable tool for the ongoing research into cerebral autoregulation.

In addition, the novel method of AC measurement is able to address the major assumption of constant MCA diameter in studies using Transcranial Doppler (TCD) ultrasound. Ainslie et al.[70], for instance, used a similar hand grip task to investigate changes in blood flow through the MCA with Transcranial Doppler ultrasound and found that this task does not change the peak flow velocity within the MCA but does increase cerebrovascular resistance (as assessed by dividing MAP by peak flow velocity). It is important to note that Ainslie et al. assume that no (significant) vasoconstriction of the MCA has taken place, even though they were not able to measure this directly with TCD. Our results of decreased aBV_{Sys}, and therefore decreased compliance, at the level of the M1 segment of the MCA (Figure 7.4) suggests that there is a change in MCA diameter during systole. However, as Ainslie et al.[70], we also find an increase in cerebrovascular resistance (decrease in compliance). An important aspect from our experiment is that because of the inclusion of a volumetric measure (aBV), our data illustrates that it is an increase in cerebrovascular tone which is responsible for the increase in resistance during PEI. Because our novel AC measurement gives information about the change in diameter of the MCA it is able to give complimentary information in experiments including TCD.

Methodological considerations

Although PEI has shown to be an ideal stimulus to decrease arterial compliance of the larger cerebral arteries and to investigate cerebral autoregulation and *Cushing's mechanism*[84], it also has two major limitations. Firstly, as discussed above, PEI elevates both sympathetic outflow and systemic blood pressure making it impossible to find a conclusive cause for the decrease in arterial compliance. Secondly, PEI in itself is uncomfortable to undergo, which makes volunteer recruitment difficult and means that drop-out rates are relatively high (as illustrated here by the one out of 8 participants that did not perform both AC and CBF measurements). All participants acknowledged their discomfort after the experiment, although tolerance levels did vary between the current volunteers. The latter is illustrated by the amount of head motion calculated during both the AC and CBF measurement (Figure 7.9). Although over the group of participants there was no significant difference in head motion during rest compared to during PEI, some volunteers did show large increases in head motion (up to 66 %). In data analysis of small ROIs, such as the flow territories of the posterior circulation in the AC measurement, such an increase in head motion is detrimental for the quality of the AC measurement. The latter particularly illustrated by the participant with the largest amount of head motion during PEI (bottom row Figure 7.6).

The increase in head motion during PEI is also the reason for dividing the cardiac cycle in only 6 phases, instead of 8 as is previously suggested (*Chapter 6*). Decreasing the number of phases means that each individual phase loses specificity, for instance if each phase is 1/6th of the cardiac cycle instead of 1/8th it means that a larger portion of the cardiac cycle will be called 'systole'. However, reducing the number of cardiac phases means that in each of the cardiac phases there are more images and therefore gives maps of AC with a higher signal to noise ratio in the participants with increased head motion during PEI (*data not shown*).

In particular during the CBF measurement of PEI there was no significant change in CBF during PEI in the ROI studied even though there was a significant decrease in $P_{ET_{CO_2}}$ (Table 7.1). Carbon dioxide is a potent vasoactive factor, which is known for causing vasodilation of cerebral arteries. Therefore, changes in $P_{ET_{CO_2}}$ modulate cerebral perfusion: with percentage increases in CBF ranging from 4-6 % per mmHg increase in $P_{ET_{CO_2}}$[111,112] and decreases in CBF when $P_{ET_{CO_2}}$ decreases are found between 1-3%/mmHg[68]. A possible reason for not finding significant decreases in CBF during PEI is because of cerebral autoregulation taking place to maintain overall cerebral perfusion[68]. Moreover, note that blood pressure also is an important factor in cerebral autoregulation and that during the CBF measurement the increases in blood pressure during PEI were not significant (Table 7.1).

For all 7 participants the CBF measurement was performed after the AC measurement and there may have been a habituation effect to the IFC task and PEI. In short, in future experiments investigating the effect of sympathetic outflow on CBF it is worthwhile to use a different stimulus than PEI, not only to have a better control of changes in blood pressure and carbon dioxide, but also to use a stimulus that participants find more tolerable.

In both our AC and CBF measurements functional parameter maps are calculated based on images acquired over a period of approximately 10 minutes. However, during PEI group average MSNA shows a steady increase until the blood pressure cuff is deflated (bottom image, Figure 7.3) and therefore the results in AC and CBF found here reflect responses of these parameters to an average increase in MSNA during PEI. The current methods do not allow detection of graded responses of the cerebrovasculature to increases in sympathetic outflow, should they exist.

Lastly, using brachial blood pressure as a surrogate for cerebral blood pressure is not optimal, in particular since it is known that in young people pulse pressure in the common carotid is often lower than brachial pulse pressure[164]. Moreover, distal to the common carotid artery pulse pressure decreases even further to ensure that there is constant pressure (and flow) in the capillary bed of the brain[155]. Note that due to the inverse relationship between AC and pulse pressure overestimating the latter by using brachial measurements leads to underestimation of local AC of the cerebral arteries. In particular, this may suggest that with the decrease in pulse pressure along the cerebrovascular tree compliance of the arteries above the Circle of Willis may not be lower than AC of the proximal larger arteries, as we have found here (Figure 7.7). However, the differential response of compliance of the different size arteries to PEI is still valid, because there was no significant difference in pulse pressure between rest and PEI during the AC measurement and assuming a linear relationship between pulse pressures along the vascular tree with increases in mean arterial pressure.

To summarise, the work presented here has demonstrated the use of our novel method of measuring cerebral arterial compliance to assess the response of the human cerebrovasculature to increased sympathetic nerve activity induced by post exercise ischemia. The major cerebral arteries show a significant decrease in arterial compliance, while there was no change in the smaller arteries distal to the Circle of Willis. The decrease in compliance is caused by an increase in tone of smooth muscle cells within the vessel walls, but further investigation is required to investigate whether this was due to the increase in sympathetic outflow or blood pressure during PEI. In addition, the current work contains an application of a recent optimisation of PASL to assess perfusion within the medulla to investigate *Cushing's mechanism* in humans. Results suggest that in healthy volunteers there is no change in CBF_{MD} with increased sympathetic outflow, although confirmation of this finding requires an expansion of the number of participants. Overall, this study validates our novel measurement of AC and highlights areas of research in which our novel method can be applied, possibly in combination with our multi inversion time PASL method for medullar perfusion assessment. These areas include research focused on sympathetic regulation of the cerebrovasculature, cerebral autoregulation and essential hypertension.

Chapter 8

General discussion

The aim of this thesis was to investigate non-invasive MRI measures to be used to further the understanding of cerebrovascular physiology, with investigating the role of the sympathetic nervous system in cerebrovascular physiology as an example area for application of our imaging tools. Because the brainstem has an important role in the sympathetic nervous system, it was important to have appropriate measures of the cerebral physiology within this brain region. Chapters 4 and 5 therefore show the process of optimisation and application of multi inversion time pulsed arterial spin labelling methods for brainstem cerebrovascular physiology measurements. In addition, when investigating cerebrovascular physiology it is imperative to have a measure of vascular health of the cerebral arteries. Chapter 6 therefore introduces the novel measure of compliance of individual cerebral arteries, which assess arterial stiffness within the cerebrovasculature. In Chapter 7 both innovations in perfusion imaging are brought together to assess the effects of modulating the sympathetic nervous system on the cerebrovasculature. In this chapter the main findings of this thesis are brought together and an eye is cast on the future; where may these recent innovations of non-invasive assessment of cerebrovascular physiology lead us?

8.1. Optimisation of brainstem perfusion measurement and main perfusion findings

Perfusion imaging of the brainstem with arterial spin labelling (ASL) suffers from a low signal-to-noise ratio (SNR) because of field inhomogeneities caused by the nearby sphenoid sinus, the presence of respiratory and cardiac induced motion, and the relatively large amount of macrovascular signal. The optimisation process described in Chapter 4 addressed these problems, which resulted in an image acquisition with two main adaptations. Firstly, an interleaved spiral read-out trajectory is used for image acquisition. Using a spiral-out trajectory means that no gradients have to be loaded before k-space read-out starts and therefore enables short echo times (TE = 3 ms), which in turn means that there is little time for signal decay due to field inhomogeneities and is therefore increasing SNR. In addition, interleaving the spiral acquisition counteracts the detrimental effect of physiological noise because this acquisition scheme oversamples low frequencies in k-space. Secondly, a two-compartment model is used that fits both a macro- and microvascular component to the ASL signal curve. In contrast with single compartment models there is no overestimation of perfusion in areas that have a large macrovascular contribution to the ASL signal, such as in the brainstem.

Results from Chapters 4, 5, and 7 then consistently show that the brainstem has lower perfusion and higher arterial blood volume (aBV) than the whole brain grey matter, which is as expected based on the local anatomy. The presence of white matter, which has lower perfusion, decreases brainstem CBF and the vasculature surrounding the brainstem leads to the large macrovascular contribution to the ASL signal.

8.2. Development of arterial compliance measurement and main compliance findings

Exploring the macrovascular compartment, which was fitted but initially ignored in the optimised brainstem perfusion analysis, resulted in the development of a novel method to measure arterial compliance of individual cerebral arteries. Retrospective synchronization of image acquisition with the cardiac cycle resulted in aBV measurements in systole and diastole. The percentage increase in aBV from diastole to systole divided by the pulse pressure gives a value of arterial compliance, which was calculated for the individual arteries branching of the Circle of Willis: the anterior and bilateral middle and posterior cerebral arteries.

Both the feasibility experiment in Chapter 6 and the resting values from the PEI experiment in Chapter 7 show that the middle cerebral arteries are the least compliant, while the posterior cerebral arteries are the most compliant of the arteries branching of the Circle of Willis. Based on a comparison with the existing literature on cerebral compliance the values presented in this thesis are plausible. However, because this is the first method that is able to assess cerebral compliance of individual human arteries *in vivo* it must be noted that a direct comparison with existing literature on cerebral compliance is difficult.

Chapter 7 illustrates that during PEI compliance of the arteries at the level of and below the Circle of Willis decreases, which illustrates that during PEI smooth muscle cell tone of the cerebrovasculature is up-regulated and the arterial walls stiffen. However, the use of isometric forearm contraction followed by PEI meant that there was not only an increase in sympathetic outflow but also an increase in systemic blood pressure and both these processes can be responsible for the increase in smooth muscle tone. Therefore PEI alone is not an optimal stimulus to separate the contribution of the sympathetic outflow from blood pressure fluctuations on cerebrovascular regulation.

Cerebral autoregulation

However, PEI is an optimal stimulus to measure cerebral autoregulation: the process in which cerebral blood flow is kept constant over a range of mean arterial pressures. Interestingly, there is an ongoing debate in the current research on cerebral autoregulation whether it is the large cerebral arteries or the arterioles that are responsible for maintaining constant cerebral perfusion[68]. The results in Chapter 7 are the first *in vivo* data that show that cerebral autoregulation, at least during PEI, occurs via increasing vascular resistance of the large cerebral arteries below and at the level of the Circle of Willis and that the distal cerebrovasculature appears to be unaffected. Our novel method of arterial compliance measurement is therefore an optimal method to be included in future research into the mechanisms behind cerebral autoregulation.

8.3. The present and future of investigating Cushing's mechanism

In the framework of Cushing's mechanism it is suggested that increases in sympathetic outflow (and concomitant increases in blood pressure) are caused by hypoperfusion of the medulla[84]. Note that Cushing's mechanism was introduced to direct the ongoing research into the mechanisms behind essential hypertension, i.e. hypertension without a clear cause. In this light it is suggested that in patients with essential hypertension decreased medullar perfusion is a consequence of increased cerebral arterial resistance, which is directly related to arterial compliance[84,85,202].

The experiments including the optimised brainstem perfusion analysis (Chapters 5 and 7) strengthen the hypothesis of Cushing's mechanism: the poly-cystic ovary syndrome (PCOS) study showed that over 38 women CBF in the medulla tended to go down with increasing mean arterial blood pressure, while the within-subject design of the post exercise ischemia (PEI) study showed that when sympathetic nervous activity (and blood pressure) increases in healthy volunteers average CBF in the medulla does not change, complying with the 'selfish brain mechanism'. In addition, both studies show a decrease in aBV in the medulla with increasing blood pressure/elevated SNA, suggesting that vasoconstriction occurs and therefore cerebrovascular resistance increases. Moreover, the clear decrease in compliance in the arteries below and at the level of the Circle of Willis during PEI (Chapter 7) clearly shows that there is a decrease in cerebrovascular resistance in the basilar and internal carotid arteries. Combining the information from all three chapters (4, 5, and 7) does suggest that the hypothesis in Cushing's mechanism is correct.

However, the main focus of this thesis was to develop methods that would allow non-invasive investigation of cerebrovascular physiology and regulation thereof and not investigating Cushing's mechanism per se. The feasibility of investigating Cushing's mechanism with these methods has been shown in this work. An important next step to investigate the clinical importance of this mechanism in humans is to apply the imaging methods from this thesis in a cohort of essential hypertensives.

One interesting avenue to investigate the directionality of the relationships between hypoperfusion of the medulla, increased sympathetic outflow and increased systemic blood pressure would be to translate the optimised brainstem perfusion protocol and the compliance measurement to animal imaging. A well-established animal model that can be used to assess Cushing's mechanism is the spontaneously hypertensive rat[203]. Investigating the relationship between medullar perfusion and elevated sympathetic outflow can for instance be done by decreasing blood flow to the medulla in the prehypertensive phase of the SHR and healthy controls and follow the development of elevated sympathetic nervous activity over time[85], while including the MRI techniques presented in this thesis to assess cerebrovascular health and physiology.

Another future step to address the relationship between hypoperfusion within the medulla and elevated sympathetic outflow in humans is to combine the optimised brainstem perfusion measurement with a brainstem optimised blood oxygenation-level dependent (BOLD) imaging protocol. A decrease in perfusion on its own does not say anything about neural activity. For instance, a decrease in CBF could suggest that there is a decrease in metabolic demand and therefore a decrease in neural activity. However, if metabolic demand remains the same and the decrease in medullar perfusion is a consequence of upstream increases in cerebral arterial resistance, neural activity within the medulla may change from a standard aerobic to an anaerobic process, which in turn may activate increased sympathetic outflow by a (unknown) chemoresponse[85]. Only a combination of qualitative BOLD imaging and quantitative perfusion imaging would be able to investigate this process non-invasively.

8.4. Future developments to improve the current methods

A future development to make the measurement of cerebrovascular physiology and regulation more time efficient would be combining the optimised brainstem perfusion method with the arterial compliance measurement. Both techniques are based on multi inversion time pulsed arterial spin labelling (MTI PASL) imaging, which enables combination of the measurements into one imaging sequence. However, in order to do so it is important to optimise the number and spacing of inversion times and the number of tag-control pairs per inversion time that give the best trade-off between SNR and acquisition time. One option could be to use a scheme similar as the optimal sampling schedule (OSS) for pulsed arterial spin labelling perfusion imaging reported by Xie et al.[204], in which the inversion times and number of repetitions to use are based on minimizing the variance on the arrival time and perfusion (with given a priori distributions). To optimally combine the brainstem perfusion and compliance measurements such a sampling scheme could for instance aim to optimise AC measurement of the basilar, and CBF and aBV in the medulla. Note that making brainstem perfusion and arterial compliance measurements more time efficient would also be beneficial for future clinical application of the novel cerebrovascular physiology measures.

A confound in the novel arterial compliance measurement technique is that brachial blood pressures are used for calculation of cerebrovascular wall properties, while it is known that neither cerebral pulse pressure[164] nor cerebral mean arterial pressure[193] are the same as their systemic/brachial equivalents. One option for future research would be to combine the current measurement of arterial compliance with a model for intracranial blood pressure, as direct measurement of intracranial pressure would require invasive techniques. An example of such a model is given by Zou et al.[205], who introduced a transfer function based on measured arterial blood pressure waves in canine carotid arteries and the pressure waves in the brain parenchyma.

The innovations in the use of established perfusion imaging methods presented in this thesis have resulted in non-invasive measures of cerebrovascular physiology. The feasibility of the novel arterial compliance and the optimised brainstem perfusion measurements has been shown and first steps were made in applying these methods to investigate clinically relevant processes, such as Cushing's mechanism and cerebral autoregulation. Moreover, development of these methods is ongoing and will further strengthen the application of non-invasive assessment of cerebrovascular health in physiological magnetic resonance imaging research.

Appendix A

Publications resulting from this thesis

Peer reviewed papers

- **Warnert EAH**, Murphy K, Hall JE, Wise RG, "*Non-invasive assessment of arterial compliance of human cerebral arteries with short inversion time arterial spin labelling*", Accepted by the Journal of Cerebral Blood Flow & Metabolism in October 2014
- **Warnert EAH**, Harris AD, Murphy K, Saxena N, Tailor N, Jenkins NS, Hall JE, Wise RG, "*In vivo assessment of human brainstem cerebrovascular function: A multi inversion-time pulsed arterial spin labelling study*", Journal of Cerebral Blood Flow & Metabolism, 5 Mar 2014, Epub ahead of publication

Abstracts

- **Warnert EAH**, Harris AD, Murphy K, Chappell M, Hall JE, Wise RG, "*Measuring Tissue Perfusion in the Human Brainstem Using Multi Inversion Time Pulsed Arterial Spin Labelling*", Proc. Intl. Soc. Magn. Res. Med. 21 (2013), p. 2182
- **Warnert EAH**, Murphy K, Hall JE, Wise RG , "*Arterial compliance of human cerebral arteries measured with pulsed arterial spin labelling*", Proc. Intl. Soc. Magn. Res. Med. 22 (2014), p. 4574.
- **Warnert EAH**, Lansdown AJ, Murphy K, Hall JE, Rees DA, Wise RG, "*Brainstem cerebral blood flow of women with poly-cystic ovary syndrome (PCOS)*" , Proc. Intl. Soc. Magn. Res. Med. 22 (2014), p. 4576.
- Jenkins NS, **Warnert EAH**, K Murphy, Hall JE, Wise RG, "*Non-invasive measurement of cerebrovascular response to hypercapnia in the brainstem using arterial spin labelling*", British Journal of Anaesthesia 2014; 112 (1), 192 - 193P
- Tailor N, **Warnert EAH**, Stone AJL, Harris AD, Murphy K, Hall JE, Wise RG, "*Non-invasive measurement of brainstem blood flow in normocapnia and hypercapnia using arterial spin labeling MRI*", Anaesthesia, Vol 67, Supplement S2, p 18, 2012

- Hart E, Coope T, **Warnert E**, Harris A, Stewart L, Nightingale A, Wise R, Paton J, "*Sex differences in the relationship between cerebal vascular resistance and sympathetic nerve activity: a magnetic resonance imaging study*", FASEB J, April 2014, 28, 680.9.
- Hart E, Harris AD, Wise RG, **Warnert EA**, Stewart L, Connor K and Paton J, "*Cerebral artery resistance is directly related to sympathetic nerve activity in men*". The FASEB Journal, 27, 2013.

References

1. Jezzard P, Clare S. Principles of nuclear magnetic resonance and MRI. Functional MRI, an introduction to methods. Oxford University Press; 2001. p. 67–92.

2. Hornak JP. The Basics of MRI. Biomed Eng (NY). 2008;24:2–6.

3. King KF, Bernstein MA, Zhou XJ. Imaging gradients. Handbook of MRI Pulse Sequences. Burlington, USA: Elsevier Academic Press; 2004. p. 243–66.

4. King KF, Bernstein MA, Zhou XJ. Signal acquisition and k-space sampling. Handbook of MRI Pulse Sequences. Burlington, USA: Elsevier Academic Press; 2004. p. 365–424.

5. King KF, Bernstein MA, Zhou XJ. Spiral. Handbook of MRI Pulse Sequences. Burlington, USA: Elsevier Academic Press; 2004. p. 928–54.

6. Glover GH, Lee AT. Motion artifacts in fMRI: comparison of 2DFT with PR and spiral scan methods. Magn Reson Med. 1995;33:624–35.

7. Glover GH, Lai S. Self-navigated spiral fMRI: interleaved versus single-shot. Magn Reson Med. 1998;39(3):361–8.

8. Mansfield P. Imaging by nuclear magnetic resonance. J Phys E. 1988;21:18.

9. King KF, Bernstein MA, Zhou XJ. Basic pulse sequences. Handbook of MRI Pulse Sequences. Burlington, USA: Elsevier Academic Press; 2004. p. 579–630.

10. Iannetti GD, Wise RG. BOLD functional MRI in disease and pharmacological studies: room for improvement? Magn Reson Imaging. 2007;25(6):978–88.

11. Alsop DC, Detre JA. Multisection cerebral blood flow MR imaging with continuous arterial spin labeling. Radiology. 1998;208(2):410–6.

12. Buxton RB, Frank LR, Wong EC, Siewert B, Warach S, Edelman RR. A general kinetic model for quantitative perfusion imaging with arterial spin labeling. Magn Reson Med. 1998;40(3):383–96.

13. Wong EC, Buxton RB, Frank LR. Quantitative imaging of perfusion using a single subtraction (QUIPSS and QUIPSS II). Magn Reson Med. 1998;39(5):702–8.

14. Detre JA, Leigh JS, Williams DS, Koretsky AP. Perfusion imaging. Magn Reson Med. 1992;23:37–45.

15. Edelman RR, Siewert B, Darby DG, Thangaraj V, Nobre AC, Mesulam MM, et al. Qualitative mapping of cerebral blood flow and functional localization with echo-planar MR imaging and signal targeting with alternating radio frequency. Radiology. 1994;192(2):513–20.

16. Kim SG. Quantification of relative cerebral blood flow change by flow-sensitive alternating inversion recovery (FAIR) technique: application to functional mapping. Magn Reson Med. 1995;34(3):293–301.

17. Williams DS, Detre JA, Leigh JS, Koretsky AP. Magnetic resonance imaging of perfusion using spin inversion of arterial water. Proc Natl Acad Sci U S A. 1992;89(1):212–6.

18. Dai W, Garcia D, de Bazelaire C, Alsop DC. Continuous flow-driven inversion for arterial spin labeling using pulsed radio frequency and gradient fields. Magn Reson Med. 2008;60(6):1488–97.

19. Garcia DM, De Bazelaire C, Alsop DC. Pseudo-continuous flow driven adiabatic inversion for arterial spin labeling. 13th Annual Meeting of ISMRM. Miami Beach, FL, USA; 2005.

20. Wong EC, Buxton RB, Frank LR. A theoretical and experimental comparison of continuous and pulsed arterial spin labeling techniques for quantitative perfusion imaging. Magn Reson Med. 1998;40(3):348–55.

21. Wolff SD, Balaban RS. Magnetization transfer contrast (MTC) and tissue water proton relaxation in vivo. Magn Reson Med. 1989;10(1):135–44.

22. Aslan S, Xu F, Wang PL, Uh J, Yezhuvath US, van Osch M, et al. Estimation of labeling efficiency in pseudocontinuous arterial spin labeling. Magn Reson Med. 2010;63(3):765–71.

23. Kwong KK, Belliveau JW, Chesler DA, Goldberg IE, Weisskoff RM, Poncelet BP, et al. Dynamic magnetic resonance imaging of human brain activity during primary sensory stimulation. Proc Natl Acad Sci U S A. 1992;89(12):5675–9.

24. Wong EC, Buxton RB, Frank LR. Implementation of quantitative perfusion imaging techniques for functional brain mapping using pulsed arterial spin labeling. NMR Biomed. 1997;10(4-5):237–49.

25. Buxton RB. Arterial spin labeling techniques. Introduction to functional magnetic resonance imaging. Cambridge: Cambridge University Press; 2009. p. 307–38.

26. Chappell MA, MacIntosh BJ, Donahue MJ, Gunther M, Jezzard P, Woolrich MW. Separation of macrovascular signal in multi-inversion time arterial spin labelling MRI. Magn Reson Med. 2010;63(5):1357–65.

27. Wu WC, Mazaheri Y, Wong EC. The effects of flow dispersion and cardiac pulsation in arterial spin labeling. IEEE Trans Med Imaging. 2007;26(1):84–92.

28. Gallichan D, Jezzard P. Modeling the effects of dispersion and pulsatility of blood flow in pulsed arterial spin labeling. Magn Reson Med. 2008;60(1):53–63.

29. Brookes MJ, Morris PG, Gowland PA, Francis ST. Noninvasive measurement of arterial cerebral blood volume using Look-Locker EPI and arterial spin labeling. Magn Reson Med. 2007;58:41–54.

30. Okell TW, Chappell MA, Schulz UG, Jezzard P. A kinetic model for vessel-encoded dynamic angiography with arterial spin labeling. Magn Reson Med. 2012;68(3):969–79.

31. Look DC, Locker DR. Time saving in measurement of NMR and EPR relaxation times. Rev Sci Instrum. 1970;41:250–1.

32. Okell TW, Chappell MA, Woolrich MW, Gunther M, Feinberg DA, Jezzard P. Vessel-encoded dynamic magnetic resonance angiography using arterial spin labeling. Magn Reson Med. 2010;64:430–8.

33. Gunther M, Warmuth C, Zimmer C. Sub-millimeter Dynamic Spin Labeling Cerebral 2D-Angiography with 40ms Temporal Resolution. Proc Intl Soc Mag Reson Med. 2002;10:1100.

34. Gunther M, Bock M, Schad LR. Arterial spin labeling in combination with a look-locker sampling strategy: Inflow turbo-sampling EPI-FAIR (ITS-FAIR). Magn Reson Med. 2001;46:974–84.

35. Wong EC. Vessel-encoded arterial spin-labeling using pseudocontinuous tagging. Magn Reson Med. 2007;58:1086–91.

36. Petersen ET, Lim T, Golay X. Model-free arterial spin labeling quantification approach for perfusion MRI. Magn Reson Med. 2006;55:219–32.

37. Ho YCL, Petersen ET, Golay X. Measuring arterial and tissue responses to functional challenges using arterial spin labeling. Neuroimage. 2010;49:478–87.

38. Zhou XJ, Bernstein MA. Motion-sensitizing gradients. Handbook of MRI Pulse Sequences. Burlington, USA: Elsevier Academic Press; 2004. p. 274–91.

39. Ho YC, Petersen ET, Zimine I, Golay X. Similarities and differences in arterial responses to hypercapnia and visual stimulation. J Cereb Blood Flow Metab. 2011;31(2):560–71.

40. Yan L, Li C, Kilroy E, Wehrli FW, Wang DJJ. Quantification of arterial cerebral blood volume using multiphase-balanced SSFP-based ASL. Magn Reson Med. 2012;68:130–9.

41. Lee T, Stainsby JA, Hong J, Han E, Brittain J, Wright GA. Blood relaxation properties at 3T effects of blood oxygen saturation. Proc Intl Soc Mag Reson Med. 2011;20:131.

42. Yan L, Wang S, Zhuo Y, Wolf RL, Stiefel MF, An J, et al. Unenhanced dynamic MR angiography: high spatial and temporal resolution by using true FISP-based spin tagging with alternating radiofrequency. Radiology. 2010;256:270–9.

43. Donahue MJ, Sideso E, MacIntosh BJ, Kennedy J, Handa A, Jezzard P. Absolute arterial cerebral blood volume quantification using inflow vascular-space-occupancy with dynamic subtraction magnetic resonance imaging. J Cereb Blood Flow Metab. 2010;30:1329–42.

44. Lu H, Hua J, van Zijl PCM. Noninvasive functional imaging of cerebral blood volume with vascular-space-occupancy (VASO) MRI. NMR Biomed. 2013;26:932–48.

45. Liu TT, Brown GG. Measurement of cerebral perfusion with arterial spin labeling: Part 1. Methods. J Int Neuropsychol Soc. 2007;13(3):517–25.

46. Yan L, Smith R, Liu C, Kilroy E, Chen Y, Wang DJJ. Assessing intracranial vascular compliance using dynamic arterial spin labeling. Proc Intl Soc Mag Reson Med. 2013;21:106.

47. Cipolla MJ. Anatomy and ultrastructure. The Cerebral Circulation. San Rafael (CA): Morgan & Claypool Lifesciences; 2009.

48. Hamel E. Perivascular nerves and the regulation of cerebrovascular tone. J Appl Physiol. 2006;100:1059–64.

49. Sándor P. Nervous control of the cerebrovascular system: Doubts and facts. Neurochemistry International. 1999. p. 237–59.

50. Susan Standring, PhD Ds. Gray's Anatomy 40th edition. Churchill Livingstone. 2009.

51. Cipolla MJ. Perivascular innervation. The Cerebral Circulation. San Rafael (CA): Morgan & Claypool Lifesciences; 2009.

52. Brodal P. The autonomic nervous system. The central nervous system. Oxford University Press; 2010. p. 411–58.

53. Marieb EN, Hoehn K. The autonomic nervous system. Human anatomy and physiology. Pearson Education Inc; 2007. p. 532–54.

54. Malpas SC. Sympathetic nervous system overactivity and its role in the development of cardiovascular disease. Physiol Rev. 2010;90:513–57.

55. Naidich TP, Duvernoy HM, Delman BN, Sorensen AG, Kollias SS, Haacke EM. Duvernoy's Atlas of the Human Brain Stem and Cerebellum. Vienna: Springer-Verlag/Wien; 2009.

56. Angeles Fernández-Gil M, Palacios-Bote R, Leo-Barahona M, Mora-Encinas JP. Anatomy of the brainstem: A gaze into the stem of life. Semin Ultrasound, CT MRI. 2010;31:196–219.

57. Kiernan J, Rajakumar N. Barr's The Human Nervous System: An Anatomical Viewpoint. Journal of anatomy. Baltimore, USA: Lipipincott, Williams & Wilkins; 2014.

58. Critchley HD, Mathias CJ, Josephs O, O'Doherty J, Zanini S, Dewar BK, et al. Human cingulate cortex and autonomic control: Converging neuroimaging and clinical evidence. Brain. 2003;126:2139–52.

59. Onat F, Cavdar S. Cerebellar connections: hypothalamus. Cerebellum. 2003;2:263–9.

60. Schmahmann JD. Dysmetria of thought: Clinical consequences of cerebellar dysfunction on cognition and affect. Trends in Cognitive Sciences. 1998. p. 362–71.

61. Hall JE. Guyton and Hall Textbook of Medical Physiology. Physiology. 2010.

62. Walsh MP, Cole WC. The role of actin filament dynamics in the myogenic response of cerebral resistance arteries. Journal of Cerebral Blood Flow & Metabolism. 2012.

63. Zonta M, Angulo MC, Gobbo S, Rosengarten B, Hossmann K-A, Pozzan T, et al. Neuron-to-astrocyte signaling is central to the dynamic control of brain microcirculation. Nat Neurosci. 2003;6:43–50.

64. Peppiatt CM, Howarth C, Mobbs P, Attwell D. Bidirectional control of CNS capillary diameter by pericytes. Nature. 2006;443:700–4.

65. Webb RC. Smooth muscle contraction and relaxation. Adv Physiol Educ. 2003;27:201–6.

66. Koeppen BM, Stanton BA. Berne & Levy Physiology. Mosby; 2009.

67. Grodon Betts J, Desaix P, Johnson E, Johnson JE, Korol O, Kruse D, et al. Human anatomy and Physiology. OpenStax College. 2013.

68. Willie CK, Tzeng Y-C, Fisher J a, Ainslie PN. Integrative regulation of human brain blood flow. J Physiol. 2014;592:841–59.

69. Zhang P, Huang G, Shi X. Cerebral vasoreactivity during hypercapnia is reset by augmented sympathetic influence. J Appl Physiol. 2011;110:352–8.

70. Ainslie PN, Ashmead JC, Ide K, Morgan BJ, Poulin MJ. Differential responses to CO2 and sympathetic stimulation in the cerebral and femoral circulations in humans. The Journal of physiology. 2005 p. 613–24.

71. Ainslie PN, Brassard P. Why is the neural control of cerebral autoregulation so controversial? F1000Prime Rep. 2014;6:14.

72. Toda N. Alpha adrenergic receptor subtypes in human, monkey and dog cerebral arteries. J Pharmacol Exp Ther. 1983;226:861–8.

73. Busch H-J, Buschmann IR, Mies G, Bode C, Hossmann K-A. Arteriogenesis in hypoperfused rat brain. J Cereb Blood Flow Metab. 2003;23:621–8.

74. Ashwini CA, Shubha R, Jayanthi KS. Comparitive anatomy of the circle of Willis in man, cow, sheep, goat, and pig. Neuroanatomy. 2008;7:54–65.

75. Fonck E, Prod'hom G, Roy S, Augsburger L, Rüfenacht DA, Stergiopulos N. Effect of elastin degradation on carotid wall mechanics as assessed by a constituent-based biomechanical model. Am J Physiol Heart Circ Physiol. 2007;292:H2754–63.

76. Zanchi A, Stergiopulos N, Brunner HR, Hayoz D. Differences in the mechanical properties of the rat carotid artery in vivo, in situ, and in vitro. Hypertension. 1998;32:180–5.

77. Giller CA, Bowman G, Dyer H, Mootz L, Krippner W. Cerebral arterial diameters during changes in blood pressure and carbon dioxide during craniotomy. Neurosurgery. 1993;32:737–41; discussion 741–2.

78. Ide K, Boushel R, Sørensen HM, Fernandes A, Cai Y, Pott F, et al. Middle cerebral artery blood velocity during exercise with beta-1 adrenergic and unilateral stellate ganglion blockade in humans. Acta Physiol Scand. 2000;170:33–8.

79. Kim D-J, Kasprowicz M, Carrera E, Castellani G, Zweifel C, Lavinio A, et al. The monitoring of relative changes in compartmental compliances of brain. Physiol Meas. 2009;30:647–59.

80. Carrera E, Kim D-J, Castellani G, Zweifel C, Smielewski P, Pickard JD, et al. Cerebral arterial compliance in patients with internal carotid artery disease. Eur J Neurol. 2011;18:711–8.

81. Sander M, Macefield VG, Henderson LA. Cortical and brain stem changes in neural activity during static handgrip and postexercise ischemia in humans. J Appl Physiol. 2010;108(6):1691–700.

82. Macefield VG, Gandevia SC, Henderson LA. Neural sites involved in the sustained increase in muscle sympathetic nerve activity induced by inspiratory capacity apnea: a fMRI study. J Appl Physiol. 2006;100(1):266–73.

83. Macefield VG, Henderson LA. Real-time imaging of the medullary circuitry involved in the generation of spontaneous muscle sympathetic nerve activity in awake subjects. Hum Brain Mapp. 2010;31(4):539–49.

84. Paton JFR, Dickinson CJ, Mitchell G. Harvey Cushing and the regulation of blood pressure in giraffe, rat and man: introducing "Cushing"s mechanism'. Exp Physiol. 2009;94:11–7.

85. Cates MJ, Dickinson CJ, Hart ECJ, Paton JFR. Neurogenic hypertension and elevated vertebrobasilar arterial resistance: Is there a causative link? Curr Hypertens Rep. 2012;14:261–9.

86. Cushing H. Concerning a definite regulatory mechanism of the vasomotor centre which controls blood pressure during cerebral compression. Bull Johns Hopkins Hosp. 1901;126:289–92.

87. Smith PA, Graham LN, Mackintosh AF, Stoker JB, Mary DASG. Relationship between central sympathetic activity and stages of human hypertension. Am J Hypertens. 2004;17:217–22.

88. Waki H, Bhuiyan MER, Gouraud SS, Takagishi M, Hatada A, Kohsaka A, et al. Acute reductions in blood flow restricted to the dorsomedial medulla induce a pressor response in rats. J Hypertens. 2011;29:1536–45.

89. Cates MJ, Steed PW, Abdala APL, Langton PD, Paton JFR. Elevated vertebrobasilar artery resistance in neonatal spontaneously hypertensive rats. J Appl Physiol. 2011;111:149–56.

90. Warnert EA, Harris AD, Murphy K, Saxena N, Tailor N, Jenkins NS, et al. In vivo assessment of human brainstem cerebrovascular function: a multi-inversion time pulsed arterial spin labelling study. J Cereb Blood Flow Metab. 2014;36:956–63.

91. Somers VK, Dyken ME, Clary MP, Abboud FM. Sympathetic neural mechanisms in obstructive sleep apnea. J Clin Invest. 1995;96:1897–904.

92. Anderson EA, Balon TW, Hoffman RP, Sinkey CA, Mark AL. Insulin increases sympathetic activity but not blood pressure in borderline hypertensive humans. Hypertension. 1992;19:621–7.

93. Lansdown A, Rees DA. The sympathetic nervous system in polycystic ovary syndrome: a novel therapeutic target? Clin Endocrinol. 2012;77(6):791–801.

94. O'Rourke MF, Safar ME. Relationship between aortic stiffening and microvascular disease in brain and kidney: Cause and logic of therapy. Hypertension. 2005;46:200–4.

95. Nation DA, Wierenga CE, Clark LR, Dev SI, Stricker NH, Jak AJ, et al. Cortical and subcortical cerebrovascular resistance index in mild cognitive impairment and Alzheimer's disease. J Alzheimers Dis. 2013;36:689–98.

96. Pantoni L, Garcia JH. Pathogenesis of leukoaraiosis: a review. Stroke. 1997;28:652–9.

97. Pattinson KT, Mitsis GD, Harvey AK, Jbabdi S, Dirckx S, Mayhew SD, et al. Determination of the human brainstem respiratory control network and its cortical connections in vivo using functional and structural imaging. Neuroimage. 2009;44(2):295–305.

98. Zambreanu L, Wise RG, Brooks JC, Iannetti GD, Tracey I. A role for the brainstem in central sensitisation in humans. Evidence from functional magnetic resonance imaging. Pain. 2005;114(3):397–407.

99. Gili T, Saxena N, Diukova A, Murphy K, Hall JE, Wise RG. The thalamus and brainstem act as key hubs in alterations of human brain network connectivity induced by mild propofol sedation. J Neurosci. 2013;33(9):4024–31.

100. Leon-Carrion J, van Eeckhout P, Dominguez-Morales Mdel R, Perez-Santamaria FJ. The locked-in syndrome: a syndrome looking for a therapy. Brain Inj. 2002;16(7):571–82.

101. Afridi SK, Matharu MS, Lee L, Kaube H, Friston KJ, Frackowiak RSJ, et al. A PET study exploring the laterality of brainstem activation in migraine using glyceryl trinitrate. Brain. 2005;128:932–9.

102. Levy DE, Sidtis JJ, Rottenberg DA, Jarden JO, Strother SC, Dhawan V, et al. Differences in cerebral blood flow and glucose utilization in vegetative versus locked-in patients. Ann Neurol. 1987;22(6):673–82.

103. Khalili-Mahani N, van Osch MJ, Baerends E, Soeter RP, de Kam M, Zoethout RW, et al. Pseudocontinuous arterial spin labeling reveals dissociable effects of morphine and alcohol on regional cerebral blood flow. J Cereb Blood Flow Metab. 2011;31(5):1321–33.

104. Viviani R, Abler B, Seeringer A, Stingl JC. Effect of paroxetine and bupropion on human resting brain perfusion: an arterial spin labeling study. Neuroimage. 2012;61(4):773–9.

105. Chen Y, Wang DJ, Detre JA. Comparison of arterial transit times estimated using arterial spin labeling. MAGMA. 2012;25(2):135–44.

106. Figueiredo PM, Clare S, Jezzard P. Quantitative perfusion measurements using pulsed arterial spin labeling: effects of large region-of-interest analysis. J Magn Reson Imaging. 2005;21(6):676–82.

107. Ho YC, Petersen ET, Golay X. Measuring arterial and tissue responses to functional challenges using arterial spin labeling. Neuroimage. 2010;49(1):478–87.

108. Francis ST, Bowtell R, Gowland PA. Modeling and optimization of Look-Locker spin labeling for measuring perfusion and transit time changes in activation studies taking into account arterial blood volume. Magn Reson Med. 2008;59(2):316–25.

109. Gallichan D, Jezzard P. Variation in the shape of pulsed arterial spin labeling kinetic curves across the healthy human brain and its implications for CBF quantification. Magn Reson Med. 2009;61(3):686–95.

110. MacIntosh BJ, Filippini N, Chappell MA, Woolrich MW, Mackay CE, Jezzard P. Assessment of arterial arrival times derived from multiple inversion time pulsed arterial spin labeling MRI. Magn Reson Med. 2010;63(3):641–7.

111. Kastrup A, Kruger G, Neumann-Haefelin T, Moseley ME. Assessment of cerebrovascular reactivity with functional magnetic resonance imaging: comparison of CO(2) and breath holding. Magn Reson Imaging. 2001;19(1):13–20.

112. Noth U, Meadows GE, Kotajima F, Deichmann R, Corfield DR, Turner R. Cerebral vascular response to hypercapnia: determination with perfusion MRI at 1.5 and 3.0 Tesla using a pulsed arterial spin labeling technique. J Magn Reson Imaging. 2006;24(6):1229–35.

113. Weiskopf N, Hutton C, Josephs O, Deichmann R. Optimal EPI parameters for reduction of susceptibility-induced BOLD sensitivity losses: a whole-brain analysis at 3 T and 1.5 T. Neuroimage. 2006;33(2):493–504.

114. Cox RW. AFNI: software for analysis and visualization of functional magnetic resonance neuroimages. Comput Biomed Res. 1996;29(3):162–73.

115. Smith SM, Jenkinson M, Woolrich MW, Beckmann CF, Behrens TE, Johansen-Berg H, et al. Advances in functional and structural MR image analysis and implementation as FSL. Neuroimage. 2004;23 Suppl 1:S208–19.

116. Smith SM, Brady JM. SUSAN - A new approach to low level image processing. Int J Comput Vis. 1997;23(1):45–78.

117. Van Gelderen P, de Zwart JA, Duyn JH. Pittfalls of MRI measurement of white matter perfusion based on arterial spin labeling. Magn Reson Med. 2008;59(4):788–95.

118. Ito H, Yokoyama I, Iida H, Kinoshita T, Hatazawa J, Shimosegawa E, et al. Regional differences in cerebral vascular response to PaCO2 changes in humans measured by positron emission tomography. J Cereb Blood Flow Metab. 2000;20(8):1264–70.

119. Gauthier CJ, Hoge RD. A generalized procedure for calibrated MRI incorporating hyperoxia and hypercapnia. Hum Brain Mapp. 2013;34(5):1053–69.

120. Heistad DD, Marcus ML. Total and regional cerebral blood flow during stimulation of carotid baroreceptors. Stroke. 1976;7(3):239–43.

121. Yang Y, Engelien W, Xu S, Gu H, Silbersweig DA, Stern E. Transit time, trailing time, and cerebral blood flow during brain activation: measurement using multislice, pulsed spin-labeling perfusion imaging. Magn Reson Med. 2000;44(5):680–5.

122. Harvey AK, Pattinson KT, Brooks JC, Mayhew SD, Jenkinson M, Wise RG. Brainstem functional magnetic resonance imaging: disentangling signal from physiological noise. J Magn Reson Imaging. 2008;28(6):1337–44.

123. Glover GH, Li TQ, Ress D. Image-based method for retrospective correction of physiological motion effects in fMRI: RETROICOR. Magn Reson Med. 2000;44(1):162–7.

124. Vidorreta M, Wang Z, Rodriguez I, Pastor MA, Detre JA, Fernandez-Seara MA. Comparison of 2D and 3D single-shot ASL perfusion fMRI sequences. Neuroimage. 2012;66C:662–71.

125. Sato K, Fisher JP, Seifert T, Overgaard M, Secher NH, Ogoh S. Blood flow in internal carotid and vertebral arteries during orthostatic stress. Exp Physiol. 2012;97(12):1272–80.

126. Fauser BCJM, Tarlatzis BC, Rebar RW, Legro RS, Balen AH, Lobo R, et al. Consensus on women's health aspects of polycystic ovary syndrome (PCOS): The Amsterdam ESHRE/ASRM-Sponsored 3rd PCOS Consensus Workshop Group. Fertility and Sterility. 2012.

127. Sverrisdottir YB, Mogren T, Kataoka J, Janson PO, Stener-Victorin E. Is polycystic ovary syndrome associated with high sympathetic nerve activity and size at birth? Am J Physiol Endocrinol Metab. 2008;294(3):E576–81.

128. Esler M, Rumantir M, Wiesner G, Kaye D, Hastings J, Lambert G. Sympathetic nervous system and insulin resistance: from obesity to diabetes. Am J Hypertens. 2001;14:304S – 309S.

129. Grassi G, Facchini A, Trevano FQ, Dell'Oro R, Arenare F, Tana F, et al. Obstructive sleep apnea-dependent and -independent adrenergic activation in obesity. Hypertension. 2005;46:321–5.

130. Macefield VG. A role for the sympathetic nervous system in sympathetically maintained pain? Clin Neurophysiol. 2010;121(7):996–7.

131. Kumagai H, Oshima N, Matsuura T, Iigaya K, Imai M, Onimaru H, et al. Importance of rostral ventrolateral medulla neurons in determining efferent sympathetic nerve activity and blood pressure. Hypertens Res. 2012;35:132–41.

132. Warnert EAH, Harris AD, Murphy K, Chappell MA, Hall JE, Wise RG. Measuring Tissue Perfusion in the Human Brainstem Using Multi-Inversion Time Pulsed Arterial Spin Labelling. Proc Intl Soc Mag Reson Med. 2013;21:2182.

133. Critchley HD, Nagai Y, Gray MA, Mathias CJ. Dissecting axes of autonomic control in humans: Insights from neuroimaging. Auton Neurosci Basic Clin. 2011;161:34–42.

134. Patterson JC, Ungerleider LG, Bandettini PA. Task-independent functional brain activity correlation with skin conductance changes: an fMRI study. Neuroimage. 2002;17:1797–806.

135. Nisimaru N. Cardiovascular modules in the cerebellum. Jpn J Physiol. 2004;54:431–48.

136. Warnert EAH, Hall JE, Wise RG. Arterial compliance of the middle cerebral artery measured with short inversion time pulsed arterial spin labelling. Proc Intl Soc Mag Reson Med. 2014. p. 4574.

137. Martin AJ, Friston KJ, Colebatch JG, Frackowiak RS. Decreases in regional cerebral blood flow with normal aging. J Cereb Blood Flow Metab. 1991;11:684–9.

138. Willeumier KC, Taylor D V, Amen DG. Elevated BMI is associated with decreased blood flow in the prefrontal cortex using SPECT imaging in healthy adults. Obesity (Silver Spring). 2011;19:1095–7.

139. Douaud G, Smith S, Jenkinson M, Behrens T, Johansen-Berg H, Vickers J, et al. Anatomically related grey and white matter abnormalities in adolescent-onset schizophrenia. Brain. 2007;130:2375–86.

140. Good CD, Johnsrude IS, Ashburner J, Henson RN, Friston KJ, Frackowiak RS. A voxel-based morphometric study of ageing in 465 normal adult human brains. Neuroimage. 2001;14:21–36.

141. Andersson JLR, Jenkinson M, Smith S. Non-linear registration aka Spatial normalisation FMRIB Technial Report TR07JA2. In Practice. 2007 p. 22.

142. Höfer P, Lanzenberger R, Kasper S. Testosterone in the brain: Neuroimaging findings and the potential role for neuropsychopharmacology. European Neuropsychopharmacology. 2013. p. 79–88.

143. Marsh CA, Berent-Spillson A, Love T, Persad CC, Pop-Busui R, Zubieta JK, et al. Functional neuroimaging of emotional processing in women with polycystic ovary syndrome: A case-control pilot study. Fertil Steril. 2013;100.

144. Van Vugt DA, Krzemien A, Alsaadi H, Frank TC, Reid RL. Glucose-induced inhibition of the appetitive brain response to visual food cues in polycystic ovary syndrome patients. Brain Res. 2014;1558:44–56.

145. Van Vugt DA, Krzemien A, Alsaadi H, Palerme S, Reid RL. Effect of insulin sensitivity on corticolimbic responses to food picture in women with polycystic ovary syndrome. Obes (Silver Spring). 2013;21(6):1215–22.

146. Miller KK, Deckersbach T, Rauch SL, Fischman AJ, Grieco KA, Herzog DB, et al. Testosterone administration attenuates regional brain hypometabolism in women with anorexia nervosa. Psychiatry Res - Neuroimaging. 2004;132:197–207.

147. Bramen JE, Hranilovich JA, Dahl RE, Forbes EE, Chen J, Toga AW, et al. Puberty influences medial temporal lobe and cortical gray matter maturation differently in boys than girls matched for sexual maturity. Cereb Cortex. 2011;21:636–46.

148. Dampney RAL, Horiuchi J, Tagawa T, Fontes MAP, Potts PD, Polson JW. Medullary and supramedullary mechanisms regulating sympathetic vasomotor tone. Acta Physiologica Scandinavica. 2003. p. 209–18.

149. Dampney RA, Horiuchi J, Tagawa T, Fontes MA, Potts PD, Polson JW. Medullary and supramedullary mechanisms regulating sympathetic vasomotor tone. Acta Physiol Scand. 2003;177(3):209–18.

150. Hart EC, Joyner MJ, Wallin BG, Charkoudian N. Sex, ageing and resting blood pressure: gaining insights from the integrated balance of neural and haemodynamic factors. J Physiol. 2012;590:2069–79.

151. Narkiewicz K, Phillips BG, Kato M, Hering D, Bieniaszewski L, Somers VK. Gender-selective interaction between aging, blood pressure, and sympathetic nerve activity. Hypertension. 2005;45:522–5.

152. Hart EC, Charkoudian N, Wallin BG, Curry TB, Eisenach J, Joyner MJ. Sex and ageing differences in resting arterial pressure regulation: the role of the β-adrenergic receptors. J Physiol. 2011;589:5285–97.

153. Schmahmann JD. Disorders of the cerebellum: ataxia, dysmetria of thought, and the cerebellar cognitive affective syndrome. J Neuropsychiatry Clin Neurosci. 2004;16:367–78.

154. Spencer MP, Denison ABJ. Pulsatile blood flow in the vascular system. Handbook of Physiology Circulation. Washington, DC: Am. Physiol. Society; 1963. p. 842.

155. Hall JE, Guyton AC. Vascular distensibility and functions of the arterial and venous systems. Textbook of medical physiology. Philadelphia: Elsevier Inc; 2006. p. 171–80.

156. Prins ND, Van Dijk EJ, Den Heijer T, Vermeer SE, Jolles J, Koudstaal PJ, et al. Cerebral small-vessel disease and decline in information processing speed, executive function and memory. Brain. 2005;128:2034–41.

157. Poels MMF, Zaccai K, Verwoert GC, Vernooij MW, Hofman A, Van Der Lugt A, et al. Arterial stiffness and cerebral small vessel disease: The rotterdam scan study. Stroke. 2012;43:2637–42.

158. Hayashi K, Handa H, Nagasawa S, Okumura A, Moritake K. Stiffness and elastic behavior of human intracranial and extracranial arteries. J Biomech. 1980;13:175–84.

159. Tzeng Y-C, Ainslie PN. Blood pressure regulation IX: cerebral autoregulation under blood pressure challenges. Eur J Appl Physiol. 2013;1–15.

160. Chan GSH, Ainslie PN, Willie CK, Taylor CE, Atkinson G, Jones H, et al. Contribution of arterial Windkessel in low-frequency cerebral hemodynamics during transient changes in blood pressure. J Appl Physiol. 2011;110:917–25.

161. Reymond P, Merenda F, Perren F, Rüfenacht D, Stergiopulos N. Validation of a one-dimensional model of the systemic arterial tree. Am J Physiol Heart Circ Physiol. 2009;297:H208–22.

162. Alastruey J, Parker KH, Peir?? J, Byrd SM, Sherwin SJ. Modelling the circle of Willis to assess the effects of anatomical variations and occlusions on cerebral flows. J Biomech. 2007;40:1794–805.

163. Monson KL, Barbaro NM, Manley GT. Biaxial response of passive human cerebral arteries. Ann Biomed Eng. 2008;36:2028–41.

164. Laurent S, Cockcroft J, Van Bortel L, Boutouyrie P, Giannattasio C, Hayoz D, et al. Expert consensus document on arterial stiffness: methodological issues and clinical applications. Eur Heart J. 2006;27:2588–605.

165. Pannier BM, Avolio AP, Hoeks A, Mancia G, Takazawa K. Methods and devices for measuring arterial compliance in humans. American Journal of Hypertension. 2002. p. 743–53.

166. Cheung N, Islam FMA, Jacobs DR, Sharrett AR, Klein R, Polak JF, et al. Arterial compliance and retinal vascular caliber in cerebrovascular disease. Ann Neurol. 2007;62:618–24.

167. Tanaka H, Dinenno FA, Monahan KD, Clevenger CM, DeSouza CA, Seals DR. Aging, habitual exercise, and dynamic arterial compliance. Circulation. 2000;102:1270–5.

168. Pattinson KT, Wynne-Jones G, Imray CHE. Monitoring intracranial pressure, perfusion and metabolism. Contin Educ Anaesth Crit Care Pain. 2005;5(4):130–3.

169. Flück D, Beaudin AE, Steinback CD, Kumarpillai G, Shobha N, McCreary CR, et al. Effects of aging on the association between cerebrovascular responses to visual stimulation, hypercapnia and arterial stiffness. Front Physiol. 2014;5:49.

170. Itoh T, Matsumoto M, Handa N, Maeda H, Hougaku H, Hashimoto H, et al. Rate of successful recording of blood flow signals in the middle cerebral artery using transcranial Doppler sonography. Stroke. 1993;24:1192–5.

171. Lu H, Clingman C, Golay X, Van Zijl PCM. Determining the longitudinal relaxation time (T1) of blood at 3.0 tesla. Magn Reson Med. 2004;52:679–82.

172. Holdsworth DW, Norley CJ, Frayne R, Steinman DA, Rutt BK. Characterization of common carotid artery blood-flow waveforms in normal human subjects. Physiol Meas. 1999;20:219–40.

173. Chappell M a, Woolrich MW, Kazan S, Jezzard P, Payne SJ, MacIntosh BJ. Modeling dispersion in arterial spin labeling: validation using dynamic angiographic measurements. Magn Reson Med. 2013;69:563–70.

174. Fonck E, Feigl GG, Fasel J, Sage D, Unser M, Rüfenacht DA, et al. Effect of aging on elastin functionality in human cerebral arteries. Stroke. 2009;40:2552–6.

175. O'Rourke MF, Staessen JA, Vlachopoulos C, Duprez D, Plante GE. Clinical applications of arterial stiffness; definitions and reference values. Am J Hypertens. 2002;15(5):426–44.

176. Grinberg L, Cheever E, Anor T, Madsen JR, Karniadakis GE. Modeling blood flow circulation in intracranial arterial networks: A comparative 3D/1D simulation study. Ann Biomed Eng. 2011;39:297–309.

177. Safar ME. Peripheral pulse pressure, large arteries, and microvessels. Hypertension. 2004;44:121–2.

178. Bank AJ, Wang H, Holte JE, Mullen K, Shammas R, Kubo SH. Contribution of Collagen, Elastin, and Smooth Muscle to In Vivo Human Brachial Artery Wall Stress and Elastic Modulus. Circulation. 1996;94:3263–70.

179. Bank AJ, Wilson RF, Kubo SH, Holte JE, Dresing TJ, Wang H. Direct effects of smooth muscle relaxation and contraction on in vivo human brachial artery elastic properties. Circ Res. 1995;77:1008–16.

180. Umeyama T, Kugimiya T, Ogawa T, Kandori Y, Ishizuka A, Hanaoka K. Changes in cerebral blood flow estimated after stellate ganglion block by single photon emission computed tomography. J Aut Nerv Syst. 1995;50:339–46.

181. Mchedlishvili GI, Mitagvaria NP, Ormotsadze LG. Vascular mechanisms controlling a constant blood supply to the brain ("Autoregulation"). Stroke. 1973;4:742–50.

182. Cipolla MJ, Li R, Vitullo L. Perivascular innervation of penetrating brain parenchymal arterioles. J Cardiovasc Pharmacol. 2004;44:1–8.

183. Dusak A, Kamasak K, Goya C, Adin ME, Elbey M a, Bilici A. Arterial distensibility in patients with ruptured and unruptured intracranial aneurysms: is it a predisposing factor for rupture risk? Med Sci Monit. 2013;19:703–9.

184. Kingwell BA, Berry KL, Cameron JD, Jennings GL, Dart AM. Arterial compliance increases after moderate-intensity cycling. Am J Physiol. 1997;273:H2186–91.

185. Ting CT, Chen CH, Chang MS, Yin FC. Short- and long-term effects of antihypertensive drugs on arterial reflections, compliance, and impedance. Hypertension. 1995 p. 524–30.

186. Birkenhäger WH, Forette F, Staessen JA. Dementia and antihypertensive treatment. Curr Opin Nephrol Hypertens. 2004;13:225–30.

187. Luh WM, Wong EC, Bandettini PA, Hyde JS. QUIPSS II with thin-slice TI1 periodic saturation: a method for improving accuracy of quantitative perfusion imaging using pulsed arterial spin labeling. Magn Reson Med. 1999;41(6):1246–54.

188. Myllylä T, Korhonen V, Vihriälä E, Sorvoja H, Hiltunen T, Tervonen O, et al. Human heart pulse wave responses measured simultaneously at several sensor placements by two MR-compatible fibre optic methods. J Sensors. 2012;2012:1–8.

189. Yuan W, Altaye M, Ret J, Schmithorst V, Byars AW, Plante E, et al. Quantification of head motion in children during various fMRI language tasks. Hum Brain Mapp. 2009;30:1481–9.

190. Vallbo AB, Hagbarth K-E, Wallin BG. Microneurography: how the technique developed and its role in the investigation of the sympathetic nervous system. J Appl Physiol. 2004;96:1262–9.

191. Sundlöf G, Wallin BG. The variability of muscle nerve sympathetic activity in resting recumbent man. J Physiol. 1977;272:383–97.

192. Hart EC, Wallin BG, Barnes JN, Joyner MJ, Charkoudian N. Sympathetic nerve activity and peripheral vasodilatator capacity in young and older men. Am J Physiol Heart Circ Physiol. 2014;

193. Faraci FM, Heistad DD. Regulation of large cerebral arteries and cerebral microvascular pressure. Circ Res. 1990;66:8–17.

194. Pires PW, Dams Ramos CM, Matin N, Dorrance AM. The effects of hypertension on the cerebral circulation. Am J Physiol Hear Circ Physiol. 2013;304:1598–614.

195. Baumbach GL, Heistad DD. Effects of sympathetic stimulation and changes in arterial pressure on segmental resistance of cerebral vessels in rabbits and cats. Circ Res. 1983;52:527–33.

196. Osol G, Brekke JF, McElroy-Yaggy K, Gokina NI. Myogenic tone, reactivity, and forced dilatation: a three-phase model of in vitro arterial myogenic behavior. Am J Physiol Heart Circ Physiol. 2002;283:H2260–7.

197. Westling H, Jansson L, Jonson B, Nilsén R. Vasoactive drugs and elastic properties of human arteries in vivo, with special reference to the action of nitroglycerine. Eur Heart J. 1984;5:609–16.

198. Rea RF, Wallin BG. Sympathetic nerve activity in arm and leg muscles during lower body negative pressure in humans. J Appl Physiol. 1989;66:2778–81.

199. Osborn JW. Hypothesis: Set-points and long-term control of arterial pressure. A theoretical argument for a long-term arterial pressure control system in the brain rather than the kidney. Clinical and Experimental Pharmacology and Physiology. 2005. p. 384–93.

200. Adapala RK, Talasila PK, Bratz IN, Zhang DX, Suzuki M, Meszaros JG, et al. PKC{alpha} mediates acetylcholine-induced activation of TRPV4-dependent calcium influx in endothelial cells. Am J Physiol Heart Circ Physiol. 2011;301:H757–65.

201. Schubert T, Santini F, Stalder AF, Bock J, Meckel S, Bonati L, et al. Dampening of blood-flow pulsatility along the carotid siphon: does from follow function? Am J Neuroradiol. 2011;32:1107–12.

202. Laurent S, Katsahian S, Fassot C, Tropeano AI, Gautier I, Laloux B, et al. Aortic stiffness is an independent predictor of fatal stroke in essential hypertension. Stroke. 2003;34:1203–6.

203. Simms AE, Paton JFR, Pickering AE, Allen AM. Amplified respiratory-sympathetic coupling in the spontaneously hypertensive rat: does it contribute to hypertension? J Physiol. 2009;587:597–610.

204. Xie J, Gallichan D, Gunn RN, Jezzard P. Optimal design of pulsed arterial spin labeling MRI experiments. Magn Reson Med. 2008;59(4):826–34.

205. Zou R, Park E-H, Kelly EM, Egnor M, Wagshul ME, Madsen JR. Intracranial pressure waves: characterization of a pulsation absorber with notch filter properties using systems analysis: laboratory investigation. J Neurosurg Pediatr. 2008;2:83–94.